Characterization of Carbon Nanotube Based Thin Film Field Emitter

by

Niraj Sinha

A thesis
presented to the University of Waterloo
in the fulfillment of the
thesis requirement for the degree of
Doctor of Philosophy
in
Systems Design Engineering

Waterloo, Ontario, Canada, 2008

I hereby declare that I am the sole author of this thesis. This is a true copy of the thesis, including any required final revisions, as accepted by my examiners.

I understand that my thesis may be made electronically available to the public.

Abstract

In recent years, carbon nanotubes (CNTs) have emerged as one of the best field emitters for a variety of technological applications. The field emitting cathodes have several advantages over the conventional thermionic cathodes: (i) current density from field emission would be orders of magnitude greater than in the thermionic case, (ii) a cold cathode would minimize the need for cooling, and (iii) a field emitting cathode can be miniaturized. In spite of good performance of such cathodes, the procedure to estimate the device current is not straight forward and the required insight towards design optimization is not well understood. In addition, the current in CNT-based thin film devices shows fluctuation. Such fluctuation in field emission current is not desirable for many biomedical applications such as x-ray devices.

The CNTs in a thin film undergo complex dynamics during field emission, which includes processes such as (i) evolution, (ii) electromechanical interaction, (iii) thermoelectric heating, (iv) ballistic transport, and (v) electron gas flow. These processes are coupled and nonlinear. Therefore, they must be analyzed accurately from the stability and long-term performance point of view. In this research, we develop detailed physics-based models of CNTs considering the aspects mentioned above. The models are integrated in a systematic manner to calculate the device current by using the Fowler-Nordheim equation. Using the models, we were able to capture the fluctuations in the field emission current, which have been observed in actual experiments. A detailed analysis of the results reveals the deflected shapes of the CNTs in an ensemble and the extent to which the initial state of geometry and orientation angles affect the device current.

In addtion, investigations on the influence of defects and impurities in CNTs on their field emission properties have been carried out. By inclusion of defects and impurities, the field emission properties of CNTs can be tailored for specific device applications in future. For stable performance of CNT-based field emission devices, such as x-ray generators, design optimization studies have been presented. It has been found that the proposed design minimizes transience in field emission current. In this thesis, it has been demonstrated that phonon-assisted control of field emission current in CNT based thin film is possible. Finally, experimental studies pertaining to crosstalk phenomenon in a multi-pixel CNT array are presented.

Acknowledgments

Upon the completion of this thesis, I would like to express my sincere appreciation to my supervisor Professor John T.W. Yeow for his invaluable guidance, constructive discussion, and encouragement, without which this work would not have been possible.

My appreciation is extended to the members of the Advisory Committee: Professor J. Zelek, Professor E. Abdel-Rahman and Professor M. Anis, for their scholarly suggestions, advices and examination in the whole process. I am honored to have Professor X. Sun as the external examiner. I am indebted to Dr. D.A. Jaffray, Professor R.V.N. Melnik and Professor D. Roy Mahapatra for their continuous encouragement and support throughout my PhD work. I am specially thankful to Mr. Fred Sun, Mr. Enam Rabbani and Ms. Xiaodan Xu, who helped me in experiments. I would also like to extend my sincere thanks to our graduate coordinator Ms. Vicky Lawrence. In addition, my appreciation goes to my friends Aashish, Sarvagya and Akhilesh for critically examining and proofreading this thesis. I will always cherish the time spent with them during long discussions at Tim Hortons.

I am greatly indebted to my parents Dr. A. K. Sinha and Mrs. C. Sinha, my siblings Mr. Shashi, Mrs. Pratima, Mrs. Purnima, and Mr. Ashutosh for their continued moral support and love. Their sacrifice in making this work a reality is gratefully acknowledged.

Last but not the least, I thank all my labmates and friends in Waterloo for their useful advice and support throughout this research.

This research was made possible by the financial support from the Natural Sciences and Engineering Research Council (NSERC) of Canada, Ontario Graduate

Scholarship in Science and Technology (OGSST), University of Waterloo President's Graduate Scholarship, University of Waterloo Graduate Scholarship, and Princess Margaret Hospital, Toronto.

Niraj Sinha
Waterloo, Ontario, Canada

Dedication

Dedicated to my parents

Dr. A.K. Sinha and Mrs. C. Sinha

Contents

1 Introduction **1**

1.1 Background 1

1.2 Problem Statement 6

1.3 Research Objectives 10

1.4 Organization 12

2 CNT Background **13**

2.1 Introduction 13

2.2 Carbon Nanotube Synthesis Techniques 14

2.2.1 Carbon Arc-Discharge Technique 14

2.2.2 Laser-Ablation Technique 15

2.2.3 Chemical Vapor Deposition Technique 17

2.2.4 Purification 18

2.3 Properties of Carbon Nanotubes 19

2.4 CNT Characterization using Field Emission 24

2.5 Role of Various Physical Processes in the Degradation of CNT Field Emitters 25
2.6 Conclusion 29

3 Modeling the Evolution, Electromechanical Forces and Electron-Phonon Interaction 31

3.1 Introduction 31
3.2 Coupling of Models and Computational Scheme 32
3.3 Idealization of the Thin Film 33
3.4 Nucleation Coupled Model for Degradation of CNTs 36
3.5 CNT Geometry and Orientation 40
3.6 Electric Field 43
3.7 Electromechanical Forces 44
  3.7.1 Lorentz Force 45
  3.7.2 Ponderomotive Force 45
  3.7.3 Electrostatic Force 46
  3.7.4 The van der Waals Force 48
3.8 Dynamics of CNTs 50
3.9 Thermodynamics of Electron-Phonon Interaction 51
3.10 Conclusion 54

4 Modeling the Deformation due to Electron Gas Flow 55

4.1 Introduction 55

4.2 Quantum-Hydrodynamic Formalism 56
4.3 Maxwellian Electromagnetics 59
4.4 Displacement due to Fluctuation of the CNT Sheet 60
4.5 Field Approximation 65
4.6 Conclusion 68

5 Results and Discussions 69

5.1 Introduction 69
5.2 Experimental Setup 70
5.3 Degradation of the CNT Thin Films 74
5.4 Current-Voltage Characteristics 80
5.5 Field Emission Current History 84
5.6 Stress and Temperature 95
5.7 Sensitivity Analysis of Parameters Affecting Device Current 99
5.8 Influence of Defects and Impurities 100
5.9 Design Optimization Results 102
5.10 Field Emission Current History for Applied AC Voltage 106
5.11 Experimental Investigation of the Crosstalk Phenomenon 111
5.12 Conclusion 115

6 Conclusions and Future Work 116

6.1 Contributions of the Thesis 116
6.2 Future Work 117

Bibliography **121**

Appendices **141**

A Discretization of the nucleation coupled model for degradation **141**

B Calculation of the parameters c_{11} to c_{33} **145**

C Derivation of out-of-plane stress ($\sigma_{\mathbf{rr}}$) **151**

D Converting the electromagnetics equation into Bessel form **153**

E Details of the design of vacuum chamber **155**

F List of publications during PhD **158**

Chapter 1

Introduction

1.1 Background

Electron sources play an important role in electronic devices. The conventional mechanism used for electron emission is thermionic in nature. In this case, some of the electrons that are bound to the cathode material gain sufficient thermal energy to overcome the binding forces within the cathode and appear as free electrons outside the cathode. As the temperature is further increased, the number of electrons that are emitted also increases, therefore, showing strong dependence on the temperature of the cathode material (in addition to its work function). The energy-band diagram for thermionic emission is shown in Fig. 1.1 . A necessary condition for emission to take place is that the electrons must possess energy $X = E_F + \Phi$, where E_F is the Fermi level energy and Φ is the work function of the cathode material. The thermally emitted current density (J_{th}) is given by the Richardson-Dushmann equation,

$$J_{th} = A_{th} T^2 \exp\left(- \frac{\Phi}{kT} \right), \tag{1.1}$$

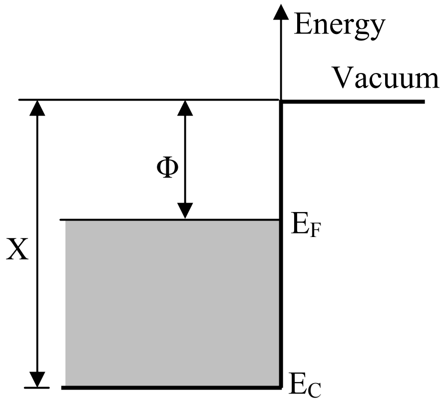

Figure 1.1: Energy-band diagram for thermionic emission.

where T is the temperature, k is the Boltzmann's constant and A_{th} is a constant, which depends on surface forces, material processes and surface roughness. The advantage of these hot cathodes is that they work even in environments containing a large number of gaseous molecules. However, thermionic cathodes in general have slow response time and they consume high power. Besides, the cathodes have limited lifetime due to mechanical wear. In addition, the thermionic electrons have random spatial distribution. As a result, fine focussing of electron beam is very difficult. This adversely affects the performance of some devices such as x-ray tubes where a small focal point is necessary to obtain high-resolution image(s).

An alternative mechanism to extract electrons is field emission, in which electrons near the Fermi level can tunnel through the energy barrier and escape to the vacuum under the influence of a sufficiently high external electric field. The electron tunneling due to high electric field is shown in Fig. 1.2 [1]. In the figure, the slope of the potential energy corresponding to the externally applied electric field is very steep. The electrons inside the cathode see on the boundary an equivalent potential barrier that has a very small width. Therefore, an electron possessing an

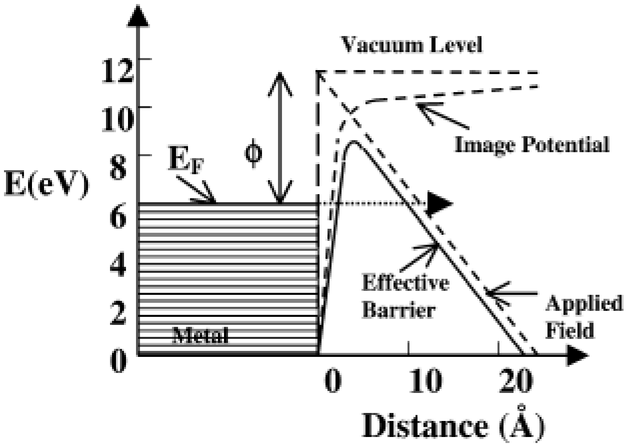

Figure 1.2: Potential energy diagram illustrating the effect of an external electric field on the energy barrier for electrons [1].

energy in the vicinity of the Fermi level now has a finite probability of tunneling through the surface potential barrier and escaping from the cathode.

The physics of field emission from metallic surfaces is well understood. The current density (J) due to field emission from a metal surface is usually obtained by using the Fowler-Nordheim (FN) equation [2], which is expressed as

$$J = \frac{BE^2}{\Phi} \exp\left(-\frac{C\Phi^{3/2}}{E}\right), \tag{1.2}$$

where E is the electric field, and B and C are constants. It is important to note that field emission current is independent of the temperature of the cathode. There are several advantages associated with field emission cathodes (also called cold cathodes).

(i) They have faster response time than the heated filaments (thermionic). As no heating is required, field emission cathodes start emitting the instant an extraction field is applied. They are particularly suitable for applications, which require instant 'on';

(ii) They consume less power because they do not require a power supply to heat the cathode(s). Here it is important to mention that there are issues related to the efficieny of extraction field. Nevertheless, these cathodes seem more appropriate for portable applications, which operate on battery power and where saving every unit of power is important;

(iii) These cathodes have longer life because there is no heating of the source since the emission current is almost solely controlled by the external field.

However, field emission cathodes require ultra-high vacuum (UHV) ambience for operation as they are highly affected by the gaseous molecules present during the field emission.

The key to the high performance of a field emission device is the behavior of its cathode. In the past, the performance of cathode materials such as Spindt-type emitters and nanostructured diamonds for field emssion has been studied by Spindt *et al.* [3], Gotoh *et al.* [4], and Zhu [5]. However, the Spindt type emitters suffer from high manufacturing cost and limited lifetime. Their failure is often caused by ion bombardment from the residual gas species that blunt the emitter cones [4]. On the other hand, nanostructured diamonds are unstable at high current densities [5]. Carbon nanotube (CNT), which is an allotrope of carbon, has potential to be used as cathode material in field emission devices. CNTs can essentially be thought of as a layer of graphite rolled-up into a cylinder. There are two types of CNTs: single-walled nanotubes (SWNTs) and multi-walled nanotubes (MWNTs). SWNTs and MWNTs differ in the arrangement of their graphene cylinders. These two types of CNTs are shown in Fig. 1.3 [6]. Furthermore, the CNTs in a thin

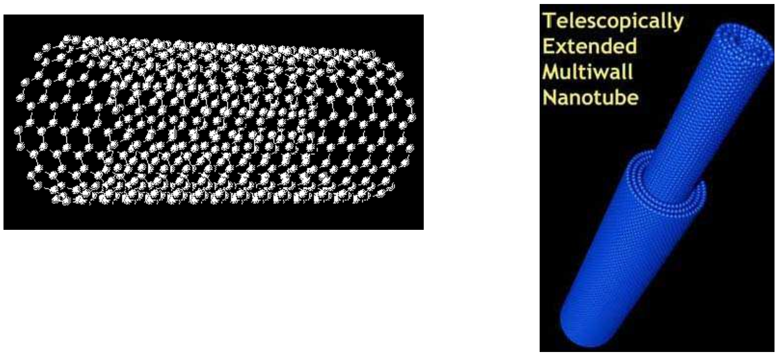

(a) (b)

Figure 1.3: (a) Structure of SWNTs. (b) Structure of MWNTs [6].

film/array can be either aligned or random (see Fig. 1.4) [7]. Since their discovery by Iijima in 1991 [8], extensive research on CNTs has been conducted. Field emission from CNTs was first reported in 1995 by Rinzler *et al.* [9], de Heer *et al.* [10], and Chernozatonskii *et al.* [11]. Field emission from CNTs has been studied extensively since then. With significant improvement in processing techniques, CNTs are currently among the best field emitters, and their application in field emission devices, such as field emission displays, gas discharge tubes, nanolithography systems, electron microscopes, lamps and x-ray tube sources has been successfully demonstrated [12]-[14]. The remarkable field emission properties of CNTs are attributed to their geometry, high thermal conductivity, and chemical stability, which will be discussed later in this thesis. In addition, the fact that carbon has very low sputter coefficients, is advantageous because an electron source is usually bombarded by positive ions. Studies have also reported that CNT sources have a high reduced brightness and their energy spread values are comparable to conventional field emitters and thermionic emitters [15].

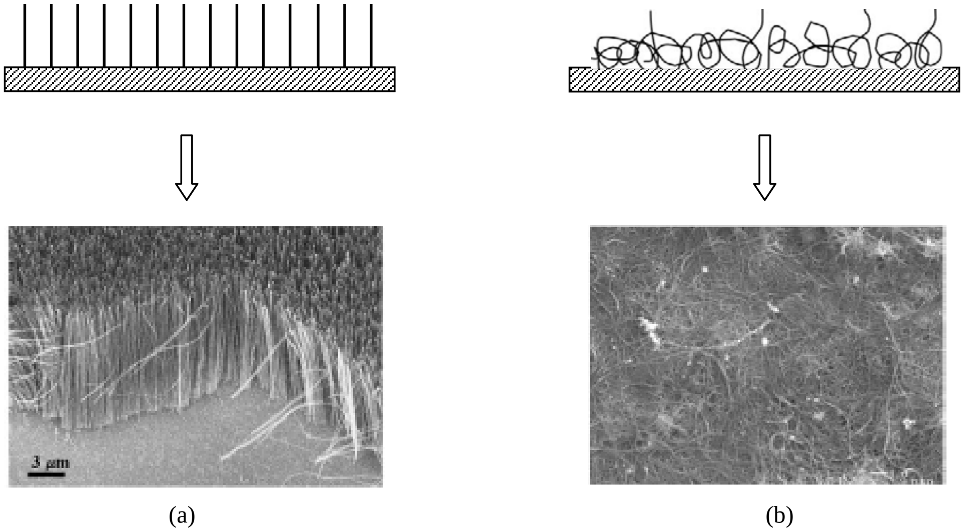

(a)

(b)

Figure 1.4: (a) Aligned CNTs. (b) Random CNTs [7].

1.2 Problem Statement

Field emission performance of a single isolated CNT is found to be remarkable, and as discussed earlier, this is due to structural integrity, high thermal conductivity, chemical stability and geometry of the CNTs. CNTs can be used as electron sources either in single or in multiple electron beam devices. In a single electron beam device, one can use a single CNT to produce an electron beam, whereas a continuous or a patterned film of CNTs is required to produce several independent electron beams. However, the situation becomes highly complex for cathodes comprising of an ensemble of CNTs, where the individual CNTs are not always aligned normal to the surface of the substrate. Figure 1.5 shows a scanning electron microscope (SEM) image in which the CNT tips are oriented in random manner. This is the most common situation, which can evolve from an initially ordered state of uniformly distributed and vertically oriented CNTs. Such evolution process must

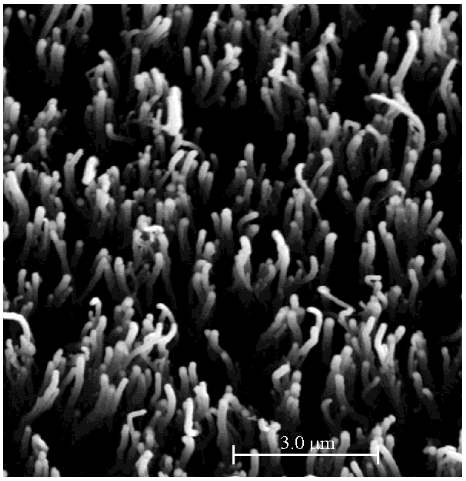

Figure 1.5: SEM image showing randomly oriented tip of CNTs in a thin film.

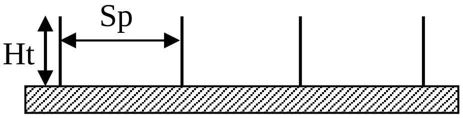

Figure 1.6: In an ideal situation, Sp/Ht > 1 for no screening.

be analyzed accurately from the view point of long-term performance of the device. Interests towards such an analysis and design studies stem from the problem of precision biomedical x-ray generation.

Till date, some studies have reported experimental observations on CNT thin films [16]. However, from mathematical, computational and design viewpoints, the models and characterization methods are available only for vertically aligned CNTs grown on patterned surface [17], [18]. In a CNT film, the array of CNTs may ideally be aligned vertically. However, in this case it is desired that the individual CNTs be evenly separated in such a way that their spacing is greater than their height to minimize the screening effect (see Fig. 1.6) [1]. If that is not followed, then the electric field on each CNT is shielded by neighboring CNTs, resulting in restrained

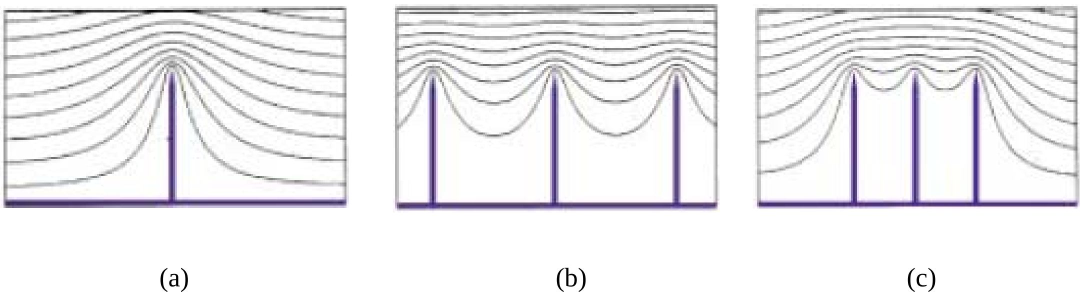

Figure 1.7: Simulation of equipotential lines of the electrostatic field for varying distances between neighboring CNTs [19].

field penetration as shown in Fig. 1.7 [19]. On the other hand, if the screening effect is minimized, then the emission properties as well as the lifetime of cathodes are adversely affected due to significant reduction in density of CNTs. For the cathodes with randomly oriented CNTs, the field emission current is produced by two types of sources: (i) small fraction of CNTs that point towards the current collector (anode) and (ii) oriented CNTs subjected to electromechanical forces causing reorientation due to the curved and flexible nature of CNTs. As often inferred [1], the advantage of the cathodes with randomly oriented CNTs is that always a large number of CNTs take part in the field emission over a longer period of time. This is unlikely in the case of cathodes with uniformly aligned CNTs. Due to this reason, thin film of randomly oriented CNTs will also be considered in the present study.

As mentioned earlier, detailed model and subsequent characterization method are currently not available for CNT thin films, where the array of CNTs may undergo complex dynamics during the process of charge transport, which includes (i) evolution, (ii) electromechanical interaction, (iii) thermoelectric heating, and (iv) ballistic transport. These processes are coupled, nonlinear, and multiphysics in their nature. In the majority of analytical and design studies, it is usual practice to employ the classical FN equation for field emission from metallic surface, with correction factors, to deal with the CNT tip geometry. The effect of degradation and fragmentation of CNTs during field emission should be considered and an evolution model should be developed. Also, in order to account for the oriented CNTs and interaction between themselves, it is necessary to consider the space charge and the electromechanical forces responsible for realignment. In addition, the coupled electron-phonon transport may produce temperature spikes. The temperature can significantly influence the electrical conductivity. Therefore, thermodynamics of electron-phonon interaction should also be included while developing a mathematical model. Some of the related factors are also important from device design considerations.

In addition to the problems discussed above, different kinds of defects and impurities are inevitably introduced in CNTs due to the lack of complete control over CNT synthesis process. Till date, studies have mainly been carried out on the types of defects and impurities in CNTs [20]. However, not much is known as to how these defects affect the field emission properties of CNTs. For a clear understanding, a system level modeling approach incorporating structural defects, vacancies or charge impurities is missing. This study is important because by intoducing defects in CNTs, their properties can be tailored for certain applications.

In the conventional approach, a DC bias voltage is applied in order to observe field emission. It has not been demonstrated so far that phonon-assisted control of field emission current in CNT-based thin film is possible.

In addition to the problems discussd above, leaking of current from one circuit to the neighboring circuit (also known as crosstalk) is very common in field emission devices. In many field emission devices where multiple pixels of CNTs are used, crosstalk is undesirable. Not much has been reported about crosstalk in multi-pixel field emission devices. These investigations led to the setting of research objectives for this study, which are outlined in the next section.

1.3 Research Objectives

The following objectives are defined for this thesis:

Objective 1: *To develop a multiphysics model for characterization of field emission from CNT thin films.*

This objective is the core of this thesis. To achieve this objective, models for the processes of evolution, re-orientation (self-assembly of CNTs), electromechanical interaction among the CNTs in the film, and thermodynamics of electron-phonon interaction are developed. These models are coupled in a systematic manner and the field emission current is computed. From a system perspective, such a detailed study proves to be helpful in understanding the reason behind the experimentally observed fluctuation in the device current, which is undesirable for applications such as precision x-ray generation biomedical devices. To this end, we show experimental results and quantitative comparison with simulations confirming the reorientation and degradation of the CNTs.

Objective 2: *To model the effect of defects and impurities on field emission performance of CNT arrays.*

The formulation and results to be obtained for the abovementioned case are for ideal CNTs, which are without defects. The effect of defects and impurities is modeled by employing a Green's function based approach. A two-step approach is adopted in this case. First, a concept of effective stiffness degradation for CNTs is introduced, which is due to structural defects. Then, we incorporate the vacancy defects and charge impurity effects in our Green's function based approach. Based on this procedure, the impact of the defects and impurities on the field emission current has been computed.

Objective 3: *To optimize the design of field emission from a stacked CNT array.*

This objective is achieved by introducing two additional gates on the edges of the cathode substrate. The height of CNT is varied linearly as opposed to the uniform distribution, which is the general case. The field emission current is simulated for this configuration and compared with the uniformly distributed case.

Objective 4: *To prove/demonstrate that phonon-assisted control of field emission current in a CNT-based thin film is possible.*

To achieve this objective, a novel approach is proposed where a frquency dependent electric field is applied so that mode specific propagation of phonons, in correspondence with the strained band structure and the dispersion curves, takes place. This is a first approach of its kind, which gives a clear indication that phonon-assisted control of field emission current in CNT-based thin film is possible.

Objective 5: *To investigate the crosstalk phenomenon during field emission in a multi-pixel CNT array.*

This objective is achieved by using one CNT source and multiple anodes as opposed to the traditional multiple CNT sources and multiple gates/anodes. The effect of increasing the number of directions was analyzed and the optimal distance between neighboring gates/anodes in order to avoid crosstalk was obtained.

1.4 Organization

The remainder of the thesis will be organized as follows. Chapter 2 will provide a review of synthesis, properties and role of various processes in the degradation/fragmentation of CNTs. In Chapter 3, a multiphysics model is proposed, which takes into account the nucleation coupled model for CNT degradation, electro-mechanical forces, and thermodynamics of electron-phonon interaction. The displacement of the CNT sheet due to flow of electron gas on its surface is modeled in Chapter 4 with the help of quantum-hydrodynamic formalism, Maxwellian electromagnetics and mechanics of CNTs. Chapter 5 presents the experimental setup, computation scheme for solving the model, numerical simulations and their comparison with experimental results. Chapter 6 is a conclusion with recommendations for further studies.

Chapter 2

CNT Background

2.1 Introduction

In the previous chapter, the techniques of electron emission were reviewed and advantages of field emission over conventional thermionic emission were discussed. It was argued that CNTs are among the best field emitters currently available. The purpose of this chapter is to provide further justification to the significance of CNT based field emitters. This chapter is organized as follows. Section 2.2 will discuss different synthesis and purification techniques of CNTs. Section 2.3 discusses the electrical, electronic, mechanical and thermal properties of CNTs. In Section 2.4, significance of field emission as a characterization tool for CNTs is illustrated. The role of various physical processes in degradation of CNTs will be reviewed in Section 2.5. Section 2.6 contains general concluding remarks.

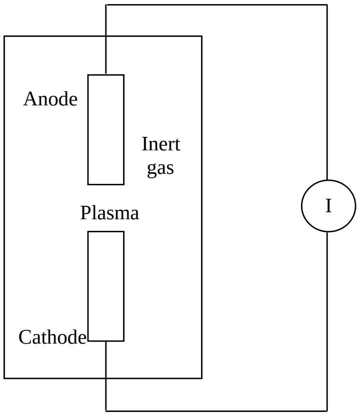

Figure 2.1: Schematic diagram of arc-discharge technique of producing CNTs.

2.2 Carbon Nanotube Synthesis Techniques

For synthesis of defect-free CNTs of macroscopic lengths in desired quantities, development of reliable synthesis techniques are essential. Controlling the chirality of CNTs for a specific application is very challenging. The state-of-the-art synthesis techniques produce statistical distributions of chiralities, and hence, electrical properties [21]. In general, following three techniques are used for synthesizing CNTs: (i) carbon arc-discharge technique; (ii) laser-ablation technique; and (iii) chemical vapor deposition (CVD) technique. The three techniques are discussed in detail below.

2.2.1 Carbon Arc-Discharge Technique

In the carbon arc-discharge technique, two carbon electrodes are kept in a vacuum chamber. The electrodes are used to generate an arc by DC current. An inert gas is supplied to the chamber to increase the speed of carbon deposition. After the stabilization of pressure, the power supply is turned on (about 20V) and the positive electrode is gradually brought closer to the negative electrode to strike the electric arc. The electrodes become red hot and a plasma forms. The rods are kept about a millimeter apart upon stabilization of the arc. During this period, the CNT deposits on the negative electrode. The power supply is cut-off and the machine is left for cooling once a specific length is reached. Figure 2.1 shows the schematic diagram of the arc-discharge technique. The two most important parameters to be taken care of in this method are: (i) the control of arcing current; and (ii) the optimal selection of inert gas pressure in the chamber [22]. Using arc-discharge technique, MWNTs were first discovered by Iijima [8] in 1991 when he saw very thin and long tubes of pure carbon under electron microscope. The growth of SWNTs for the first time was desmonstrated by Iijima and Ichihashi [23] and Bethune *et al.* [24] in 1993 using arc-discharge technique. Arc-discharge technique produces high quality CNTs. While MWNTs do not need a catalyst for growth, SWNTs can only be grown in presence of a catalyst. MWNTs can be obtained by controlling the pressure of inert gas in the discharge chamber and the arcing current. The by-products are polyhedron shaped multi-layered graphitic particles in case of MWNTs. Li *et al.* [25] synthesized SWNTs by modifying the arc-discharge method and by using FeS as a promoter. As evaluated by scanning electron microscopy, thermogravimetric analysis, and Raman spectroscopy, the synthesized SWNT fibers were 80% pure by volume. Later, Paladugu *et al.* [26] demonstrated that CNTs can be synthesized by arc-discharge in open air. As their method does not require a controlled atmosphere, therefore, the cost of production may be reduced.

2.2.2 Laser-Ablation Technique

Intense laser pulses are utilized in the laser-ablation technique to ablate a carbon target, which in the presence of an inert gas and catalyst forms CNTs. Figure 2.2

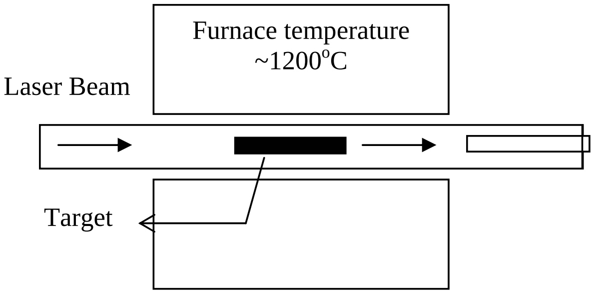

Figure 2.2: Schematic diagram of laser-ablation technique of producing CNTs.

shows the schematic diagram of the laser-ablation technique. An analysis by X-ray diffraction (XRD) and transmission electron microscopy (TEM) revealed that the SWNTs produced by Thess *et al.* [27] using laser-ablation were ropes (or bundles) of 5 to 20 nm diameter and tens to hundreds of micrometers of length. It was found by Arepalli *et al.* [28] that individual nanotubes of lengths tens of microns are formed in the vicinity of the target at the beginning, which subsequently coalesce into bundles. Based on spectral emission and laser-induced fluorescence measurements, Scott *et al.* [29] suggested that the carbon for the formation of CNTs comes from direct ablation as well as from carbon particles suspended in the reaction zone. In addition, the confinement of CNTs in the reaction zone within the laser beam leads to the purification and annealing of CNTs by laser heating. By using high vacuum laser-ablation, multi-layered MWNTs were grown selectively by Takahashi *et al.* [30] by dispersing graphite powder on a Si (100) substrate. In general, the amount and type of catalysts, laser power and wavelength, temperature, pressure, type of inert gas present, and the fluid dynamics near the carbon target are some of the parameters that determine the amount of CNTs produced [31]. The by-products of SWNTs in case of arc-discharge and laser-ablation techniques are fullerenes, graphitic polyhedrons with enclosed metal particles, and amorphous carbon [31].

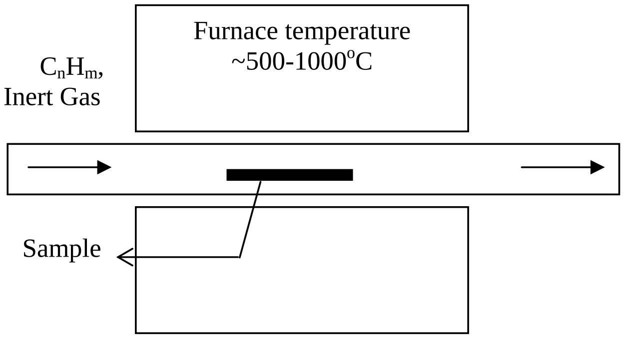

Figure 2.3: Schematic diagram of CVD technique of producing CNTs.

2.2.3 Chemical Vapor Deposition Technique

In CVD, energy is imparted to hydrocarbons (the commonly used sources are methane, ethylene, and acetylene) to break them into reactive radical species in the temperature range of 550-750°C. These reactive species diffuse down to a heated and catalyst coated surface where they remain bonded. As a result, CNTs are formed. Figure 2.3 shows the schematic diagram of the CVD technique. The commonly used energy sources are electron beam and resistive heating. By catalytic decomposition of acetylene over iron particles at 700°C, microtubules of up to 50 μm length of CNTs were synthesized by Yacaman *et al.* [32]. Vardan and Xie [33] developed a CVD technique, which used microwave energy for synthesizing MWNTs. The use of acetylene as the hydrocarbon and cobalt as the catalyst at a temperature of 700°C resulted in MWNTs with 26 layers and average diameter of 20 to 30 nm. A sequential combination of radio frequency plasma-enhanced CVD (RF PECVD) and thermal CVD was used by Park *et al.* [34] to synthesize CNTs from acetylene and hydrogen gas mixture on stainless steel plates. Wei *et al.* [35] used CVD with gas-phase catalyst delivery to direct the assembly of CNTs in a variety of predetermined orientations, building them into one-, two-, and three-dimensional arrangements. The key parameters that affect the synthesis of CNTs by CVD include the nature of hydrocarbons, catalysts, and the growth temperature.

2.2.4 Purification

In all the three synthesis techniques mentioned above, the CNTs come with a number of impurities. The type and amount of impurities depend on the synthesis technique that was used to produce CNTs. The purity of CNTs can be analyzed by spectroscopic techniques. For example, Raman spectroscopy is commonly used for qualitative evaluation of purity of CNTs, while near infrared spectroscopy can be used for the quantitative assessment. Carbonaceous materials are the most common impurities observed. The other types of impurities include metals. As carbonaceous impurities have high oxidation rates, the impurities in the carbon arc-discharge technique can be purified by oxidation. Generally, two approaches are followed for purification by oxidation: (i) gas phase oxidation, and (ii) liquid phase oxidation. Ebbesen *et al.* [36] used gas phase oxidation for purification of CNTs. As low yield of purification was observed by them, therefore, liquid phase oxidation for better homogeneity was tried by Hiura *et al.* [37]. Xu *et al.* [38] developed a process for purification of SWNTs grown by CVD of carbon monoxide that included sonication, oxidation, and acid washing steps. For MWNTs grown by CVD, Biro *et al.* [39] used wet and dry oxidation to remove impurities and traces of catalysts. Several other techniques have been proposed to purify CNTs. However, they may change the electrical and mechanical properties of CNTs since the structural surfaces of CNTs are modified after purification. Therefore, current research focus is on producing high purity CNTs directly.

2.3 Properties of Carbon Nanotubes

In general, an overview of their properties is very important because the applications of CNTs are related to some of their specific properties. For example, CNTs can be used as hydrogen storage media because they have the ability to elastically sustain loads at large deflection angles. It enables them to store or absorb considerable energy [40]. It has been theoretically predicted that the properties of a CNT are sensitively dependent on the tube diameter (d) and chiral angle (θ) [41], [42]. Depending upon these two parameters, a CNT can be either metallic or semiconducting. The diameter and the chiral angle can be obtained by an integer pair (n, m) using following equations [43]:

$$d = \frac{a\sqrt{m^2 + mn + n^2}}{\pi} \tag{2.1}$$

$$\theta = \tan^{-1}\left[\frac{\sqrt{3}n}{2m + n}\right] \tag{2.2}$$

where a is the lattice constant in the graphite sheet. The relation between n and m defines following three categories of CNTs:

(i) armchair ($n = m$ and chiral angle equal to 30°);

(ii) zigzag ($n = 0$ or $m = 0$ and chiral angle equal to 0°); and

(iii) chiral (other values of n and m and chiral angles between 0° and 30°) [44].

Fig. 2.4 shows all three categories of CNTs [45]. All armchair nanotubes are metals, as well as those with $n - m = 3j$ (j being a nonzero integer). All others are semiconductors, which have the band gap that is inversely related to the diameters of the nanotubes [46]. MWNTs are either nested CNT shells [47] or have cinnamon roll like structure [48].

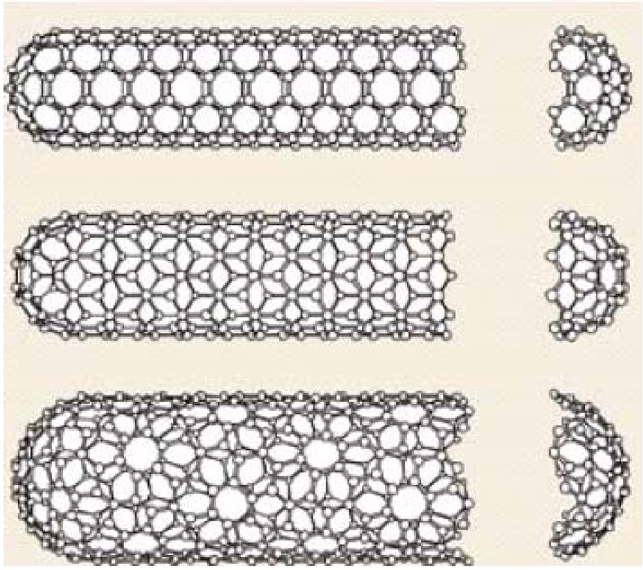

Figure 2.4: (a) Armchair, (b) zigzag and (c) chiral CNTs [45].

The dielectric responses of the carbon nanotubes are found to be highly anisotropic. Owing to their nearly one dimensional electronic structure, the electronic transport in metallic SWNTs and MWNTs occurs ballistically (without scattering) over long lengths. This enables nanotubes to carry high currents with negligible heating [49]. It was observed through experiments by Wei *et al.* [50] that MWNTs can carry high current densities up to 109-1010 A/cm^2 and can conduct current without any measurable change in their resistance or morphology for extended periods of time at temperature up to 250°C. This points to the potential of CNTs as interconnects in large-scale integrated nanoelectronic devices. However, gas adsorption and collisions affect the electrical transport in SWNTs. It was observed that the gas collisions with the nanotube wall increase thermoelectric power and resistivity [51].

The electrical and electronic properties of nanotubes are affected by distortions like bending and twisting. Pentagon-heptagon pair is introduced in CNTs by bending, which results in metal-metal and semiconductor-metal nanoscale junctions that can be used for nano-switches [52]. The effect of bending becomes important when bending angles are more than 45°. At this stage, kinks appear in the structure of the tube, resulting in the reduction in conductivity of CNTs [53]. However, the presence of a metal nanowire inside the nanotube greatly suppresses the tube-buckling instability. In this case, increased tube diameter leads to an increase in the bending strength [54]. A band gap opens upon twisting, which turns metallic CNTs to semiconducting. CNT structures collapse when twisted above a certain angle [55]. Also, superconductivity in SWNTs has been observed but only at low temperatures [56]. Doping of CNTs provide various possibilities for controlling their physical properties. Doped CNTs can find applications in nanoelectronics, spintronics, field emission, nonlinear optics, and chemical sensors [57].

Mechanically, CNTs are currently the strongest known fibers because the carbon-carbon bond observed in graphite is one of the strongest in nature. Elastic properties of CNTs can be obtained from experiment by assuming them as structural members. The Young's modulus (a measure of stiffness) of individual MWNTs was first determined by Treacy *et al.* [58]. They estimated the Young's modulus of isolated CNTs by measuring the amplitude of their intrinsic thermal vibrations in TEM. The average value of Young's modulus was found to be 1800 GPa. Atomic force microscopy (AFM) was used by Wong *et al.* [40] to determine the mechanical properties of MWNTs by pinning them at one end to molybdenum disulfide surfaces. The average value of Young's modulus was found to be 1280 GPa. Falvo *et al.* [59] observed that MWNTs can be bent repeatedly through large angles without undergoing catastrophic failures by using the tip of an atomic force microscope. All these studies suggest that multilayered CNTs are very strong in nature and are remarkably flexible and resistant to fracture when subjected to large strain. Later, Gaillard *et al.* [60] showed that the Young's modulus can be measured in individual

CVD grown MWNTs by electrostatically driving it into resonance. The bending modulus was found relatively more sensitive to wall defects than the nanotube diameter. However, a comparison of these studies indicates that the values of the mechanical parameters are quite confusing. For instance, a study by Lourie and Wagner [61] reported the Young's modulus of SWNTs as 2800-3600 GPa and that of MWNTs as 1700-2400 GPa; whereas studies by Yu *et al.* [62] reported the Young's modulus of SWNTs between 320-1470 GPa and that of MWNTs between 270-950 GPa. The reason behind different numerical values is that some researchers use the total occupied cross sectional area for defining the Young's modulus, while others use the much smaller van der Waals area. Because of their low density (1.3 g/cm^3), materials made of nanotubes are lighter. At the same time, they are more durable. As CNTs have very high aspect ratio, CNT structures are susceptible to structural instability. However, SWNTs have better defined shapes of cylinder than MWNTs, and hence, have less possibilities of structure defects. Therefore, SWNT is preferred over MWNT for carrying out research and for developing applications.

It is extremely challenging to measure the tensile strength of CNTs. Yu *et al.* [63] found the tensile strength of SWNT bundles in the range of 13 to 52 GPa, whereas the value was in the range of 11 to 63 GPa for MWNTs. In case of MWNTs, it was observed that only the outermost layer breaks during the tensile load testing process. Wong *et al.* measured the bending strength of large-diameter MWNTs. According to them, bending strength is the strain determined at the initial buckling point because the stiffness drops significantly at this point. The average value of bending strength determined by them was 14.2 ± 8.0 GPa, while the maximum value was 28.5 GPa. A compressive strength of 100-150 GPa and a compressive strain of 5% was found by Lourie *et al.* [65] as a result of compressive loading of MWNTs. It was also observed that the fracture strength and the elastic limit of nanotubes depend on their chirality [66], [67].

It was found that temperature plays a key role in the strength of CNTs because motion of dislocations is thermally activated. CNTs are brittle at low temperature, irrespective of their diameter and helicity. However, CNTs exhibit flexibility at room temperature due to their high strength and the distortion capability of hexagonal network for relaxing stress [68]. At high temperature, spontaneous formation of double pentagon-heptagon (or 5/7) pairs were observed in strained CNTs. It was found that such defects depend on the chirality of CNTs and are energetically favored in defect-free armchair nanotubes when the tensile strain is greater than 5%. These defects constitute the onset of the possible plastic deformation of CNTs [69]. It is important to mention here that the high strength and high stiffness properties of an individual SWNT does not necessarily imply that CNT structures will have the same properties [47].

CNTs show good load transfer characteristics with metal matrix composites. Efficient load transfer between a matrix and CNTs plays a key role in the mechanical properties of composites and can lead to the development of many superstrong nanocomposites. However, poor load transfer behavior of CNTs in tension compared to compression was observed because only the outermost nanotubes are loaded in tension due to weak interlayer bonding [68]. In another study, MWNTs were used as reinforcing phase in a polyacrylonitrile (PAN) fiber matrix to produce a PAN-derived carbon/MWNT composite fiber. Significant mechanical property increases were recorded for the composite fibers compared with the samples with no MWNT reinforcement: break strength +31%, initial modulus +36%, yield strength +46%, energy to yield +80%, and energy to break +83% [70]. Also, the mechanical properties of CNTs and their polymer nanocomposites have been reviewed extensively by Miyagawa *et al.* [71]. Viscoelasticity in carbon nanotube composites was studied by Suhr *et al.* [72]. Based on the direct shear testing, they concluded that nanotube fillers offer great improvement in damping without sacrificing mechanical properties and structural integrity.

The specific heat and thermal conductivity of CNTs are dominated by phonons as the electronic contribution is negligible due to low density of free charge carriers [73]. The experiments by Yi *et al.* [74] revealed linear dependence of the specific heat of MWNTs on the temperature over the entire temperature interval (10 to 300K). The specific heat of SWNT bundles was measured by Lasjaunias *et al.* [76] down to a temperature of 0.1K. The presence of sublinear temperature dependence of specific heat, dominant below 1K, was observed. This dependence could not be understood and warrants further investigation into the thermal properties of CNTs. For measuring thermal conductivities of CNTs to isotopic and other atomic defects, the domination of phonons leads to unusual sensitivity of the experiments [77]. Kim *et al.* [78] determined that at room temperature, the thermal conductivity for an individual MWNT ($>$ 3000 W/mK) is greater than that of graphite (2000 W/mK). It was observed by Zhang *et al.* [79] that the value of heat conductivity of zigzag nanotube is maximum, while the chiral nanotube has a minimum value. They also found that the thermal conductivity of SWNTs depends on their length, radius, temperature, and chirality. Therefore, nanoscale devices with different heat conductivities can be made with nanotubes of different chirality.

2.4 CNT Characterization using Field Emission

In general, field emission is studied with an ultimate goal of realizing a device. Advances in the growth techniques of CNT thin films have also taken place in order to have a better control of the film morphology for enhanced field emission properties. Though it has been investigated rarely, field emission has a huge potential as a characterization method. First, it offers the possibility of simultaneous determination of the electronic and structural properties of individual nanotubes. While the electronic density of states (DOS) can be measured by field emission electron energy distribution (FEED), the exact structure of the tube cap can be determined by field ionization microscopy (FIM) [80]. Second, the temperature dependence of the electrical and thermal conductivities of CNTs can be measured using field emission. This is due to the fact that field emission permits controlled Joule heating of individual emitters and estimation of the resistance of CNT [81]. Third, the mechanical properties of individual MWNTs can be studied within an assembly of emitters because field emission allows direct observation of the mechanical vibration resonances of CNTs. The tensile loading created by the applied field permits the tuning of these resonances, which can be observed by changes in the field emission pattern or current [82]. Finally, field emission enables the estimation of the growth rate during synthesis of CNTs using CVD [83]. In order to achieve this goal, a field emission microscope (FEM) is integrated with a CVD reactor and growth is followed by watching the spots (using FEM) corresponding to emitting CNTs and by measuring the field emitted current [84]. This information can be useful in controlling the length of CNTs.

2.5 Role of Various Physical Processes in the Degradation of CNT Field Emitters

In CNT thin films, spikes in the current have been observed experimentally. These can be attributed to change in gap between the CNT tip and the anode plate

Figure 2.5: CNTs were peeled off at very high bias and deposited on the anode.

either due to elongation of CNTs under high bias voltage or due to degradation/fragmentation of CNTs. Several studies have reported experimental observations in favour of considerable degradation and failure of CNT cathodes. These studies can be divided into two categories: (i) studies related to degradation of single nanotube emitter [85]-[90] and (ii) studies related to degradation of CNT thin films [91]-[96]. Dean *et al.* [86] found gradual decrease of field enhancement of single walled carbon nanotubes (SWNTs) due to evaporation when large field emitted current ($300\ nA\ to\ 2\ \mu A$) was extracted. It was observed by Lim *et al.* [96] that CNTs are susceptible to damage by exposure to gases such as oxygen and nitrogen during field emission. Wei *et al.* [87] observed that after field emission over 30 minutes at field emission currents between 50 and 120 nA, the length of CNTs became shorter by 10%. Occasional spikes in the current-voltage curves were observed by Chung *et al.* [89] when the voltage was increased. Avouris *et al.* [90] found that the CNTs break down when subjected to high bias for a long period of time. Usually, the breakdown process involves stepwise increases in the resistance. In the experiments performed by the us, peeling of the film from the substrate was observed at high bias (see Fig. 2.5). Some of the physics are known but the overall phenomenon out of such complex system is difficult to explain and quantify and requires further investigation.

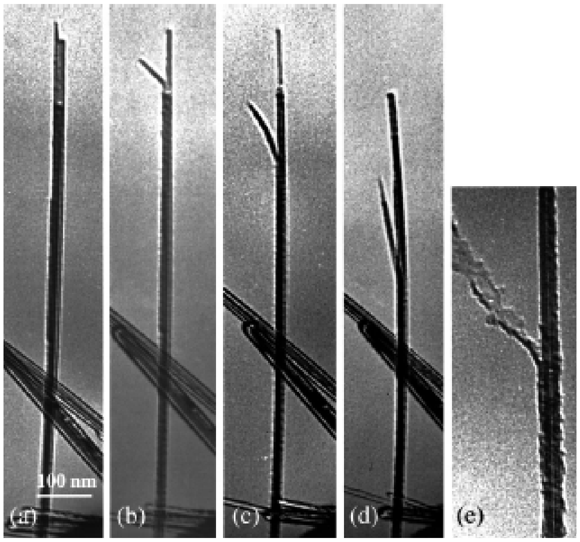

Figure 2.6: Series of TEM images showing the structural damage of a CNT by splitting effect during field emission [88].

There are several causes of CNT failures:

(i) In case of multi walled carbon nanotubes (MWNTs), the CNTs undergo layer-by-layer splitting and stripping during field emission (see Figs. 2.6, 2.7) [88]. The complete removal of the shells are most likely the reason for the spikes in the current voltage curves [89];

(ii) At high emitted currents CNTs are resistively heated. Thermal effect can sublime a CNT causing cathode-initiated vacuum breakdown [97]. Also, in case of thin films grown using chemical vapor deposition (CVD), fewer catalytic metals such as nickel, cobalt, and iron are observed as impurities in CNT thin films. These metal particles melt and evaporate by high emission currents, and abruptly surge the emission current. This results in vacuum breakdown followed by the failure of the CNT film [96];

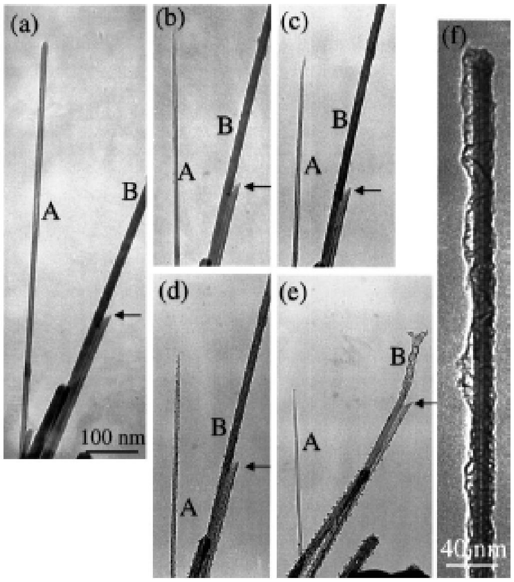

Figure 2.7: Series of TEM images showing the structural damage of a CNT by stripping effect during field emission [88].

(iii) Gas exposure induces chemisorption and physisorption of gas molecules on the surface of CNTs. In the low-voltage regime, the gas adsorbates remain on the surface of the emitters. On the other hand, in high-voltage regime, large emission currents resistively anneal the tips of the CNTs, and the strong electric field on the locally heated tips promotes the desorption of gas adsorbates from the tip surface. Adsorption of materials with high electronegativity hinders the electron emission by intensifying the local potential barriers. Surface morphology can be changed by erosion of the cap of the CNT as the gases desorb reactively from the surface of the CNTs [98];

(iv) CVD-grown CNTs tend to show more defects in the wall as their radius increases. Possibly, there are rearrangements of atomic structures (for example, vacancy migration) resulting in the reduction of length of CNTs [87].

In addition, the presence of defects may act as a centre for nucleation for voltage-induced oxidation, resulting in electrical breakdown [89];

(v) As the CNTs grow perpendicular to the substrate, the contact area of CNTs with the substrate is very small. This is weak point in CNT films grown on planar substrates, and CNTs may fail mechanically at applied fields due to tensile loading [93]. Overall, small nanotube diameters and lengths are an advantage from the stability point of view.

Although the mode of degradation and failure of single nanotube emitters can either be abrupt or gradual, degradation of a thin film emitter with CNT cluster is mostly gradual. The gradual degradation occurs either during initial current-voltage measurement [94] or during measurements at constant applied voltage over a long period of time [95]. Nevertheless, it can be concluded that the gradual degradation of thin films occurs due to the failure of individual emitters.

2.6 Conclusion

In a very short duration, carbon nanotubes appear to be the frontrunner that has the potential to dominate the future research. However, there remain challenges that need to be addressed before the full potential of CNTs for biomedical applications can be realized. For example, there is a lack of detailed understanding of growth mechanism of CNTs. As a result, an efficient growth approach to structurally perfect nanotubes at large scales is currently not available. Secondly, it is difficult to grow defect-free nanotubes continuously to macroscopic lengths. Thirdly, control over nanotubes growth on surfaces is required in order to obtain large-scale ordered nanowire structures. Finally, controlling the chirality of SWNTs by any existing growth method is very difficult. Also, properties of CNTs were reviewed in this chapter. Even though the properties of CNTs have been studied extensively in recent years, only tip of the iceberg has been addressed. A database of properties of CNTs as a function of concentration and type of defects, chemical environment, temperature, chemical environment, etc. should be established to reap their maximum benefits.

Chapter 3

Modeling the Evolution, Electromechanical Forces and Electron-Phonon Interaction

3.1 Introduction

As discussed earlier, the current density (J) due to field emission from a metallic surface is usually obtained by using the Fowler-Nordheim equation [2]. In the CNT thin film problem, under the influence of sufficiently high voltage at ultra-high vacuum, the electrons emitted from the CNTs (mainly from the CNT tip region and emitted parallel to the axis of the tubes) reach the anode. Unlike the metallic emitters, here, the surface of the cathode is not smooth. The cathode consists of CNTs (often in curved shapes) with certain spacings. In addition, certain amount of impurities and carbon clusters may be present within the otherwise empty spaces in the film. Moreover, the CNTs undergo re-orientation due to electromechanical interactions with the neighbouring CNTs during field emission. Analysis of these processes requires determination of the current density by considering the CNT ensemble geometry, their dynamic orientations and the variation in the electric field during electronic transport. In this chapter, the process of evolution, reorientation (self-assembly of CNTs), electromechanical interactions among the CNTs in the film and thermodynamics of electron-phonon interaction are analyzed, and a multiphysics model is developed. This chapter is organized as follows. Section 3.2 illustrates the coupling of models and computational scheme to calculate the device current. Section 3.3 discusses the idealization of the CNT thin film using few simplifications for the development of the multiphysics model. In Section 3.4, a nucleation coupled model for degradation of CNTs during field emission is proposed. Effects of CNT geometry and orientation is discussed in Section 3.5. Section 3.6 illustrates the approach to calculate electric field for estimation of current density. Electromechanical force calculations are described in Section 3.7. The dynamics of CNTs will be derived in Section 3.8. In Section 3.9, thermodynamics of electron-phonon interaction will be discussed. Section 3.10 contains concluding remarks.

3.2 Coupling of Models and Computational Scheme

A key characteristics is the device current, and in what follows we focus on the systematic integration of all the models at the computational level to calculate the device current. At a given time, the evolved concentration of carbon clusters due to the process of degradation and CNT fragmentation is obtained from the nucleation coupled model. This information is then used in a time-incremental manner to describe the evolved state of the CNTs in the cells. At each time step, the net electromechanical force is computed using the momentum balance equation

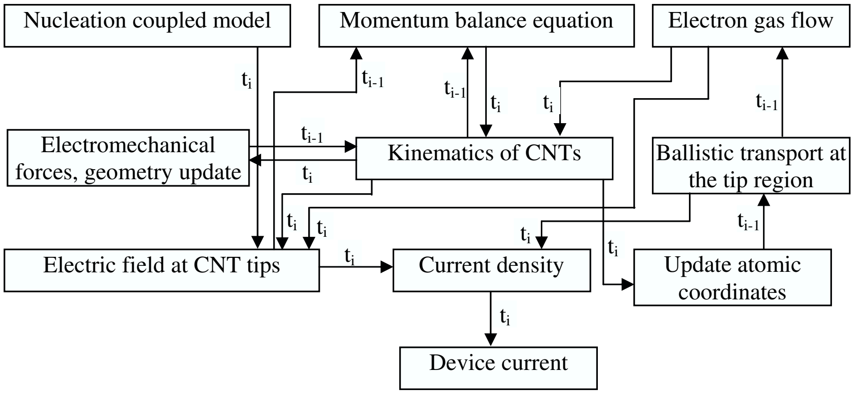

Figure 3.1: Computational flowchart for calculating the device current.

and equation for electron gas flow. Subsequently, the orientation angle of each CNT tip is obtained. Thereafter, we compute the electric field at the tip of CNTs at each time step. Finally, the current density and device current are calculated by employing Eq. (1.2). The computational flow chart for calculating the device current is shown in Fig. 3.1.

3.3 Idealization of the Thin Film

The CNT thin film is idealized in our mathematical model by using the following simplifications [99].

(i) CNTs are grown on a substrate to form a thin film. They are treated as aggregate while deriving the nucleation coupled model for degradation phenomenologically;

(ii) The film is discretized into a number of representative volume element (cell), in which a number of CNTs can be in oriented forms along with an estimated

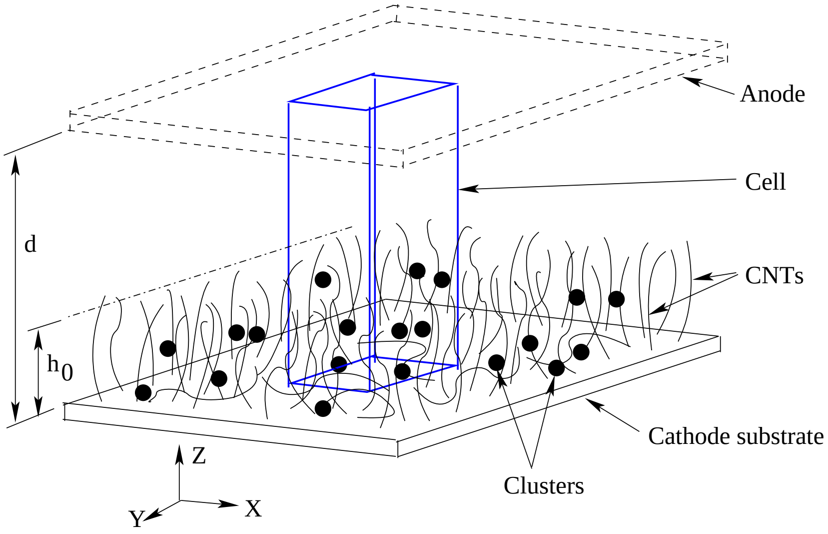

Figure 3.2: Schematic drawing of the CNT thin film for model idealization.

amount of carbon clusters. This is schematically shown in Fig. 3.2. The carbon clusters are assumed to be in the form of carbon chains and networks (monomers and polymers);

(iii) Each of the CNTs with hexagonal arrangement of carbon atoms (shown in Fig. 3.3(a)) are treated as effectively one-dimensional (1D) elastic members and discretized by nodes and segments along its axis as shown in Fig. 3.3(b). Deformation of this 1D representation is the combined effect of the orientations of the segments within the cell and fluctuation of the sheet of carbon atoms in the CNTs and hence the resulting state of atomic arrangements (due to electron flow).

The surface electron density can be decomposed into a steady (unstrained) part and a fluctuating part. Therefore,

$$\tilde{n} = \tilde{n}_0 + \tilde{n}_1 \ , \tag{3.1}$$

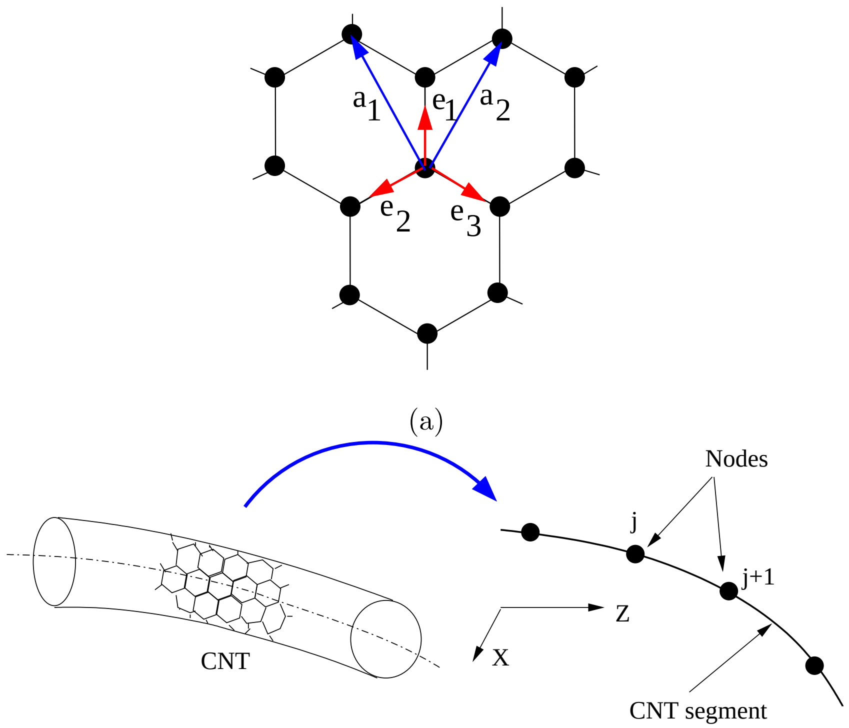

(a)

(b)

Figure 3.3: Schematic drawing showing (a) hexagonal arrangement of carbon atoms in CNT and (b) idealization of CNT as a one-dimensional elastic member.

where the the steady part $\tilde{n}_0$ is the surface electron density corresponding to the Fermi level energy in the unstrained CNT, and it can be approximated as in [100]

$$\tilde{n}_0 = \frac{kT}{\pi b^2 \Delta} \ , \tag{3.2}$$

where b is the interatomic distance and Δ is the overlap integral ($\approx 2eV$ for carbon). In Eq. (3.1), the fluctuating part $\tilde{n}_1$ is inhomogeneous along the length of the CNTs. Actually, $\tilde{n}_1$ should be coupled nonlinearly with the deformation and the electromagnetic field, which will be illustrated later in this thesis.

As discussed earlier, the displacement can be due to electromechanical forces and due to the fluctuation of the CNT sheet due to electron flow in the CNT. Therefore, the total displacement ($\mathbf{u_{total}}$) can be expressed as

$$\mathbf{u_{total}} = \mathbf{u^{(1)}} + \mathbf{u^{(2)}} \ , \tag{3.3}$$

where $\mathbf{u^{(1)}}$ and $\mathbf{u^{(2)}}$ are the displacement vectors due to electromechanical forces and fluctuation of the CNT sheet, respectively. The elements of displacement vector in the coordinate system (x', z') can be written as

$$\mathbf{u^{(1)}} = \left\{ \begin{array}{c} u_{x'}^{(1)} \\ u_{z'}^{(1)} \end{array} \right\} \ , \quad \mathbf{u^{(2)}} = \left\{ \begin{array}{c} u_{x'}^{(2)} \\ u_{z'}^{(2)} \end{array} \right\} \ , \tag{3.4}$$

where $\mathbf{u_{x'}}$ is the lateral displacement and $\mathbf{u_{z'}}$ is the longitudinal displacement.

3.4 Nucleation Coupled Model for Degradation of CNTs

Let N_T be the total number of carbon atoms (in CNTs and in cluster form) in a cell (see Fig. 3.2). The volume of a cell is given by $V_{\text{cell}} = \Delta A d$, where ΔA is the cell surface interfacing the anode and d is distance between the inner surfaces of cathode substrate and the anode. Let N be the number of CNTs in the cell, and N_{CNT} be the total number of carbon atoms present in the CNTs. We assume that during field emission some CNTs are decomposed and form clusters. Such degradation and fragmentation of CNTs can be treated as the reverse process of CVD or a similar growth process used for producing the CNTs on a substrate. Hence,

$$N_T = N N_{CNT} + N_{\text{cluster}} \ , \tag{3.5}$$

where N_{cluster} is the total number of carbon atoms in the clusters in a cell at time t and is given by

$$N_{\text{cluster}} = V_{\text{cell}} \int_0^t dn_1(t) \ , \tag{3.6}$$

where n_1 is the concentration of carbon cluster in the cell. By combining Eqs. (3.5) and (3.6), one has [101]

$$N = \frac{1}{N_{CNT}} \left[N_T - V_{\text{cell}} \int_0^t dn_1(t) \right] . \tag{3.7}$$

The number of carbon atoms in a CNT is proportional to its length. Let the length of a CNT be a function of time, denoted as $L(t)$. Therefore, one can write

$$N_{CNT} = N_{\text{ring}} L(t) \ , \tag{3.8}$$

where N_{ring} is the number of carbon atoms per unit length of a CNT and can be determined from the geometry of the hexagonal arrangement of carbon atoms in the CNT. By combining Eqs. (3.7) and (3.8), one can write

$$N = \frac{1}{N_{\text{ring}} L(t)} \left[N_T - V_{\text{cell}} \int_0^t dn_1(t) \right] . \tag{3.9}$$

In order to determine $n_1(t)$ phenomenologically, we need to know the nature of evolution of the aggregate in the cell. From the physical point of view, one may expect the rate of formation of the carbon clusters from CNTs to be a function of thermodynamic quantities, such as temperature (T), the relative distances (r_{ij}) between the carbon atoms in the CNTs, the relative distances between the clusters and a set of parameters (p^*) describing the critical cluster geometry. The relative distance r_{ij} between carbon atoms in CNTs is a function of the electromechanical forces. Modeling of this effect is discussed in Sec. 3.5. On the other hand, the relative distances between the clusters influence in homogenizing the thermodynamic energy, that is, the decreasing distances between the clusters (hence increasing densities of clusters) slow down the rate of degradation and fragmentation of CNTs and lead to a saturation in the concentration of clusters in a cell. Thus, one can write

$$\frac{dn_1}{dt} = f(T, r_{ij}, p^*) \ . \tag{3.10}$$

To proceed further, we introduce a nucleation coupled model [102, 103], which was originally proposed to simulate aerosol formation. Here, we modify the original model by assuming the degradation as a reverse process of growth and model the phenomena of CNT degradation [104]. The nucleation theory has been used for the growth of CNTs [105] and other nano-particles [106, 107] also. With this model the relative distance function is replaced by a collision frequency function (β_{ij}) describing the frequency of collision between the i-mers and j-mers, with

$$\beta_{ij} = \left(\frac{3v_j}{4\pi}\right)^{1/6} \sqrt{\frac{6kT}{\rho_p}\left(\frac{1}{i} + \frac{1}{j}\right)} \left(i^{1/3} + j^{1/3}\right)^2 , \tag{3.11}$$

and the set of parameters describing the critical cluster geometry by

$$p^* = \{v_j \ s_j \ g^* \ d_p^*\} , \tag{3.12}$$

where v_j is the j-mer volume, s_j is the surface area of j-mer, g^* is the normalized critical cluster size, d_p^* is the critical cluster diameter and ρ_p is the particle mass density. In this thesis, we have considered $i = 1$ and $j = 1$ for numerical simulations, that is, only monomer type clusters are considered. The detailed form of Eq. (3.10) is given by four nonlinear ordinary differential equations:

$$\frac{dN_{\rm kin}}{dt} = J_{\rm kin} \ , \tag{3.13}$$

$$\frac{dS}{dt} = -\frac{J_{\rm kin} S g^*}{n_1} - (S-1)\frac{B_1 A_n}{2v_1} \ , \tag{3.14}$$

$$\frac{dM_1}{dt} = J_{\rm kin} d_p^* + (S-1) B_1 N_{\rm kin} \ , \tag{3.15}$$

$$\frac{dA_n}{dt} = \frac{J_{\rm kin} S g^{*2/3} s_1}{n_1} + \frac{2\pi B_1 S (S-1) M_1}{n_1} \ , \tag{3.16}$$

where $N_{\rm kin}$ is the kinetic normalization constant, $J_{\rm kin}$ is the kinetic nucleation rate, S is the saturation ratio, A_n is the total surface area of the stable carbon cluster and M_1 is the moment of cluster size distribution. The quantities involved are expressed as

$$S = \frac{n_1}{n_s} \ , \quad M_1 = \int_{d_p^*}^{d_p^{\rm max}} \Big(n(d_p, t) d_p \Big) d(d_p) \ , \tag{3.17}$$

$$N_{\rm kin} = \frac{n_1}{S} \exp(\Theta) \ , \quad J_{\rm kin} = \frac{\beta_{ij} n_1^2}{12 S} \sqrt{\frac{\Theta}{2\pi}} \exp\left(\Theta - \frac{4\Theta^3}{27 (\ln S)^2} \right) \ , \tag{3.18}$$

$$g^* = \left(\frac{2}{3} \frac{\Theta}{\ln S} \right)^3 \ , \quad d_p^* = \frac{4\sigma v_1}{kT \ln S} \ , \quad B_1 = 2 n_s v_1 \sqrt{\frac{kT}{2\pi m_1}} \ , \tag{3.19}$$

where n_s is the equilibrium saturation concentration of carbon cluster, $d_p^{\rm max}$ is the maximum diameter of the clusters, $n(d_p, t)$ is the cluster size distribution function, d_p is the cluster diameter, m_1 is the mass of the monomer, and Θ is the dimensionless surface tension given by

$$\Theta = \frac{\sigma s_1}{kT} \ , \tag{3.20}$$

where σ is the surface tension. Our main intention in this context is to find n_1 using Eq. (3.13). However, during the growth of clusters, the change in the particle size (distribution) with time is governed by the saturation ratio (ratio of atomic concentration to the concentration at saturation). Therefore, Eq. (3.14) is required. In growth related kinetics, the growth is measured by the moment of cluster size distribution [108]. M_1 in Eqs. (3.15) and (3.16) tells us about the distribution of the cluster size over time. That is, at different locations in the cell, different size of clusters can form and that also affects the equilibrium to occur. During growth of the clusters, a critical sized nucleus is a cluster of size such that its rate of growth is equal to its rate of decay. A_n indicates the area of the stable carbon cluster. To know the area of the cluster, A_n is required. So, based on the established growth kinetic theory, we need to include all the four equations. For instance in Eq. (3.16) for dA_n/dt, the first term on the right hand side of the equation describes an increase/decrease in the surface area due to newly formed stable cluster and the second term denotes an increase in area of the existing stable cluster. In the expression for moment $M_1(t)$ in Eq. (3.17), the cluster size distribution in the cell is assumed to be Gaussian, however, random distribution can be incorporated. Eqs. (3.13)-(3.16) form a set of four nonlinear coupled ordinary differential equations in $n_1(t)$, $S(t)$, $M_1(t)$ and $A_n(t)$. This system of equations is solved with the help of a finite difference scheme as discussed in Appendix A. Finally, the average number of CNTs in a cell, and hence the average height distribution with a known number of CNTs in the ensemble are obtained with the help of Eq. (3.7), where the reduced length $L(t)$ is determined using geometric properties of the individual CNTs as formulated next.

3.5 CNT Geometry and Orientation

It has been discussed earlier that the geometry and orientation of the tip of the CNTs are important factors in the overall field emission performance of the film and must be considered in the model.

As an initial condition, let $L(0) = h$ at $t = 0$, and let h_0 be the average height of the CNT region as shown in Fig. 3.2. This average height h_0 is approximately equal to the height of the CNTs that are aligned vertically. If Δh is the decrease in the length of a CNT (aligned vertically or oriented as a segment) over a time interval Δt due to degradation and fragmentation, and if d_t is the diameter of the CNT, then the surface area of the CNT decreased is $\pi d_t \Delta h$. By using the geometry of the CNT, the decreased surface area can be expressed as

$$\pi d_t \Delta h = V_{\text{cell}} n_1(t) \Big[s(s-a_1)(s-a_2)(s-a_3) \Big]^{1/2} , \tag{3.21}$$

where V_{cell} is the volume of the cell as introduced in Sec. 3.4, a_1, a_2, a_3 are the lattice constants, and $s = \frac{1}{2}(a_1 + a_2 + a_3)$ (see Fig. 3.3(a)). The chiral vector for the CNT is expressed as

$$\overrightarrow{C}_h = n\vec{a}_1 + m\vec{a}_2 , \tag{3.22}$$

where n and m are integers ($n \geq |m| \geq 0$) and the pair (n, m) defines the chirality of the CNT. The following properties hold: $\vec{a}_1.\vec{a}_1 = a_1^2$, $\vec{a}_2.\vec{a}_2 = a_2^2$, and $2\vec{a}_1.\vec{a}_2 = a_1^2 + a_2^2 - a_3^2$. With the help of these properties the circumference and the diameter of the CNT can be expressed as, respectively [109],

$$|\overrightarrow{C}_h| = \sqrt{n^2 a_1^2 + m^2 a_2^2 + nm(a_1^2 + a_2^2 - a_3^2)} , \quad d_t = \frac{|\overrightarrow{C}_h|}{\pi} , \tag{3.23}$$

Let us now introduce the rate of degradation of the CNT or simply the burning rate as $v_{\text{burn}} = \lim\limits_{\Delta t \to 0} \Delta h / \Delta t$. By dividing both side of Eq. (3.21) by Δt and by passing on the limit, one has

$$\pi d_t v_{\text{burn}} = V_{\text{cell}} \frac{dn_1(t)}{dt} \Big[s(s-a_1)(s-a_2)(s-a_3) \Big]^{1/2} , \tag{3.24}$$

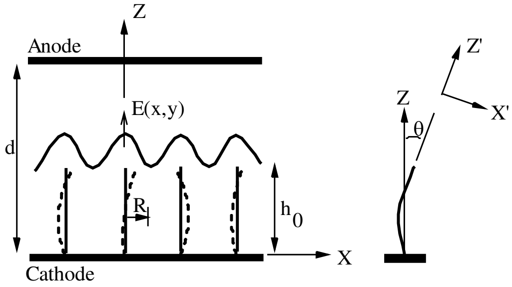

Figure 3.4: CNT array configuration.

By combining Eqs. (3.23) and (3.24), the burning rate is finally obtained as [110]

$$v_{\text{burn}} = V_{\text{cell}} \frac{dn_1(t)}{dt} \left[\frac{s(s-a_1)(s-a_2)(s-a_3)}{n^2 a_1^2 + m^2 a_2^2 + nm(a_1^2 + a_2^2 - a_3^2)} \right]^{1/2} . \tag{3.25}$$

In Fig. 3.4 we show a schematic drawing of the CNTs almost vertically aligned, that is along the direction of the electric field $E(x,y)$. This electric field $E(x,y)$ is assumed to be due to the applied bias voltage. However, there will be an additional but small amount of electric field due to several localized phenomena (e.g., electron flow in curved CNTs, field emission from the CNT tip etc.). Effectively, we assume that the distribution of the field parallel to z-axis is of periodic nature (as shown in Fig. 3.4) when the CNT tips are vertically oriented. Only a cross-sectional view in the xz plane is shown in Fig. 3.4 because only an array of CNTs across x-direction will be considered in the model for simplicity. Thus, in this study, we shall restrict our attention to a two-dimensional problem, and out-of-plane motion of the CNTs will not be incorporated in the model.

3.6 Electric Field

In the absence of electronic transport within a CNT and field emission from its tip, the background electric field is simply $E_0 = -V_0/d$, where $V_0 = V_d - V_s$ is the applied bias voltage, V_s is the constant source potential on the substrate side, V_d is the drain potential on the anode side and d is the clearance between the electrodes. The total electrostatic energy consists of a linear drop due to the uniform background electric field and the potential energy due to the charges on the CNTs. Therefore, the total electrostatic energy can be expressed as

$$\mathcal{V}(x,z) = -eV_s - e(V_d - V_s)\frac{z}{d} + \sum_j G(i,j)(\tilde{n}_j - n) \ , \tag{3.26}$$

where e is the positive electronic charge, $G(i,j)$ is the Green's function [111] with i indicating the ring position, $\tilde{n}_j$ describing the electron density at node position j on the ring and (n,m) representing the chirality parameters. In the present case, while computing the Green's function, we also consider the nodal charges of the neighboring CNTs. This essentially introduces non-local contributions due to the CNT distribution in the film. We compute the total electric field $\mathbf{E}(z) = -\nabla\mathcal{V}(z)/e$, numerically. The effective electric field component for field emission calculation in Eq. (1.2) is expressed as

$$E_z = -\frac{1}{e}\frac{d\mathcal{V}(z)}{dz} \ . \tag{3.27}$$

Computation is performed at every time step, followed by update of the geometry of the CNTs. As a result, the charge distribution among the CNTs also changes and such a change affects Eq. (5.1). The field emission current (I_{cell}) from the anode surface corresponding to an elemental volume V_{cell} of the film is then obtained as

$$I_{\text{cell}} = A_{\text{cell}} \sum_{j=1}^{N} J_j \ , \tag{3.28}$$

where A_{cell} is the anode surface area and N is the number of CNTs in the volume element. The total current is obtained by summing the cell-wise current (I_{cell}).

The above formulation takes into account the effect of CNT tip orientations, and one can perform statistical analysis of the device current for randomly distributed and randomly oriented CNTs. However, due to the deformation of the CNTs under electromechanical forces, the evolution process requires a much more detailed treatment. In order to account for the changing orientations and deformation, we first estimate the effects of electromechanical forces as discussed next.

3.7 Electromechanical Forces

For each CNT, the angle of orientation $\theta(t)$ is dependent on the electromechanical forces. Such dependence is geometrically nonlinear and it is not practical to solve the problem exactly, especially in the present situation where a large number of CNTs are to be dealt with. However, it is possible to solve the problem in time-dependent manner with an incremental update scheme. In this section we derive the components of the electromechanical forces acting on a generally oriented CNT segment.

From the studies reported in published literature and based on the discussions so far, it is reasonable to expect that the major contribution is due to (i) the Lorentz force under electron gas flow in CNTs (a hydrodynamic formalism), (ii) the ponderomotive force acting on the CNTs, (iii) the electrostatic force (background charge in the cell) and (iv) the van der Waals force against bending and shearing of MWNT.

3.7.1 Lorentz Force

Within the quantum-hydrodynamic formalism, one generally assumes the flow of electron gas along the cylindrical sheet of CNTs. The associated electron density distribution is related to the energy states along the length of the CNTs including the tip region. What is important for the present modeling is that the CNTs experience Lorentz force under the influence of the bias electric field as the electrons flow from the cathode substrate to the tip of a CNT. The Lorentz force is expressed as

$$\vec{f_l} = e(\tilde{n}_0 + \tilde{n}_1)\vec{E} \approx e\tilde{n}_0\vec{E} \ , \tag{3.29}$$

where e is the electronic charge. The components of the Lorentz force acting along z and x directions can now be written as, respectively,

$$f_{lz} = \pi d_t e\tilde{n}_0 E_z \ , \quad f_{lx} = \pi d_t e\tilde{n}_0 E_x \approx 0 \ . \tag{3.30}$$

3.7.2 Ponderomotive Force

Ponderomotive force, which acts on free charges on the surface of CNTs under oscillatory high field, tends to straighten the bent CNTs in the Z-direction. Furthermore, the ponderomotive forces induced by the applied electric field stretch every CNT [112]. In order to estimate the components of the ponderomotive force (f_{p_x}, f_{p_z}) acting on the tip region (see ref. [113]), the following approximations are used:

$$f_{p_z} \approx \frac{q^2}{2m_e\omega^2} E_z \frac{\partial E_z}{\partial z} \ , \quad f_{p_x} \approx 0 \ , \tag{3.31}$$

where $q = (\pi d_t e\hat{n})ds$ is the total charge on an elemental segment ds of a CNT, m_e is the mass of an electron, $\omega = 2\pi/\tau$ with τ is the relaxation frequency and f_{p_z} is the Z component of the ponderomotive force. X component of the ponderomotive force f_{p_x} is assumed to be negligible.

3.7.3 Electrostatic Force

In order to calculate the electrostatic force, the interaction among two neighboring CNTs is considered. For such calculation, let us consider a segment ds_1 on a CNT (denoted 1) and another segment ds_2 on its neighboring CNT (denoted 2). These are parts of the representative 1D member idealized as shown in Fig. 3.3(b). The charges associated with these two segments can be expressed as

$$q_1 = e\tilde{n}_0 \pi d_t^{(1)} ds_1 \ , \quad q_2 = e\tilde{n}_0 \pi d_t^{(2)} ds_2 \ , \tag{3.32}$$

where $d_t^{(1)}$ and $d_t^{(2)}$ are diameters of two neighbouring CNTs (1) and (2). The electrostatic force on the segment ds_1 by the segment ds_2 is

$$\frac{1}{4\pi\epsilon\epsilon_0} \frac{q_1 q_2}{r_{12}^2} \ ,$$

where ϵ is the effective permittivity of the aggregate of CNTs and carbon clusters, ϵ_0 is the permittivity of free space, and r_{12} is the effective distance between the centroids of ds_1 and ds_2. The electrostatic force on the segment ds_1 due to charge in the entire segment (s_2) of the neighboring CNT (see Fig. 3.5) can be written as

$$\frac{1}{4\pi\epsilon\epsilon_0} \int_0^{s_2} \frac{1}{r_{12}^2} \left(e\tilde{n}_0 \pi d_t^{(1)} ds_1 e\tilde{n}_0 \pi d_t^{(2)} \right) ds_2 \ .$$

The electrostatic force per unit length on s_1 due to s_2 is then

$$f_c = \frac{1}{4\pi\epsilon\epsilon_0} \int_0^{s_2} \frac{(\pi e\tilde{n}_0)^2 d_t^{(1)} d_t^{(2)}}{r_{12}^2} \, ds_2 \ . \tag{3.33}$$

The differential of the force df_c acts along the line joining the centroids of the segments ds_1 and ds_2 as shown in Fig. 3.5. Therefore, the components of the total electrostatic force per unit length of CNT (1) in X and Z directions can be written as, respectively,

$$\begin{aligned} f_{c_x} &= \int df_c \cos\phi = \frac{1}{4\pi\epsilon\epsilon_0} \int_0^{s_2} \frac{(\pi e\tilde{n}_0)^2 d_t^{(1)} d_t^{(2)}}{r_{12}^2} \cos\phi \; ds_2 \\ &\equiv \frac{1}{4\pi\epsilon\epsilon_0} \sum_{j=1}^{h_0/\Delta s_2} \frac{(\pi e\tilde{n}_0)^2 d_t^{(1)} d_t^{(2)}}{r_{12}^2} \; \cos\phi \; \Delta s_2 \; , \end{aligned} \tag{3.34}$$

$$\begin{aligned} f_{c_z} &= \int df_c \sin\phi = \frac{1}{4\pi\epsilon\epsilon_0} \int_0^{s_2} \frac{(\pi e\hat{n}_0)^2 d_t^{(1)} d_t^{(2)}}{r_{12}^2} \sin\phi \; ds_2 \\ &\equiv \frac{1}{4\pi\epsilon\epsilon_0} \sum_{j=1}^{h_0/\Delta s_2} \frac{(\pi e\tilde{n}_0)^2 d_t^{(1)} d_t^{(2)}}{r_{12}^2} \; \sin\phi \; \Delta s_2 \; , \end{aligned} \tag{3.35}$$

where ϕ is the angle the force vector df_c makes with the X-axis. For numerical computation of the above integrals, we compute the angle $\phi = \phi(s_1^k, s_2^j)$ and $r_{12} = r_{12}(s_1^k, s_2^j)$ at each of the centroids of the segments between the nodes $k+1$ and k, where the length of the segments are assumed to be uniform and denoted as Δs_1 for CNT (1) and Δs_2 for CNT (2). As shown in Fig. 3.5, the distance r_{12} between the centroids of the segments ds_1 and ds_2 is obtained as

$$r_{12} = \left[(d_1 - l_{x_2} + l_{x_1})^2 + (l_{z_1} - l_{z_2})^2 \right]^{1/2} \; , \tag{3.36}$$

where d_1 is the spacing between the CNTs at the cathode substrate, l_{x_1} and l_{x_2} are the deflections along X-axis, and l_{z_1} and l_{z_2} are the deflections along Z-axis. The angle of projection ϕ is expressed as

$$\phi = \tan^{-1} \left(\frac{l_{z_1} - l_{z_2}}{d_1 - l_{x_2} + l_{x_1}} \right) \; . \tag{3.37}$$

The deflections l_{x_1}, l_{z_1}, l_{x_2}, and l_{z_2} are defined as, respectively,

$$l_{x_1} = \int_0^{s_1} ds_1 \;\; \sin\theta_1 \equiv \sum_j \Delta s_1 \sin\theta_1^j \tag{3.38}$$

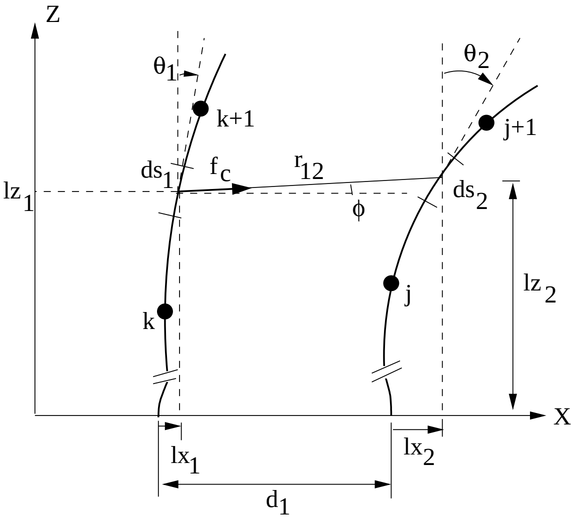

Figure 3.5: Schematic description of neighboring CNT pair interaction for calculation of electrostatic force.

$$l_{z_1} = \int_0^{s_1} ds_1 \ \cos\theta_1 \equiv \sum_j \Delta s_1 \cos\theta_1^j \tag{3.39}$$

$$l_{x_2} = \int_0^{s_2} ds_2 \ \sin\theta_2 \equiv \sum_j \Delta s_2 \sin\theta_2^j \tag{3.40}$$

$$l_{z_2} = \int_0^{s_2} ds_2 \ \cos\theta_2 \equiv \sum_j \Delta s_2 \cos\theta_2^j \,. \tag{3.41}$$

Note that the total electrostatic force on a particular CNT is to be obtained by summing up all the binary contributions within the cell, that is by summing up Eqs. (3.34) and (3.35) over the upper integer number of the quantity $N-1$, where N is the number of CNTs in the cell as discussed in Sec. 3.4.

3.7.4 The van der Waals Force

Next, we consider the van der Waals effect. The van der Waals force plays an important role not only in the interaction of the CNTs with the substrate, but also in the interaction between the walls of MWNTs and CNT bundles. Due to the overall effect of forces and flexibility of the CNTs (here assumed to be elastic 1D members), the cylindrical symmetry of CNTs is destroyed, leading to their axial and radial deformations. The change in cylindrical symmetry may significantly affect the properties of CNTs [114, 115]. Here we estimate the van der Waals forces due to the interaction between two concentric walls of the MWCNTs.

Let us assume that the lateral and the longitudinal displacements of a CNT be $u_{x'}$ and $u_{z'}$, respectively. We use updated Lagrangian approach with local coordinate system for this description [similar to (X', Z') system shown in Fig. 3.4], where the longitudinal axis coincides with Z' and the lateral axis coincides with X'. Such a description is consistent with the incremental procedure to update the CNT orientations in the cells as adopted in the computational scheme. Also, due to the large length-to-diameter ratio $(L(t)/d_t)$, let the kinematics of the CNTs, which are idealized in this work as 1D elastic members, be governed by that of an Euler-Bernoulli beam. Therefore, the kinematics can be written as

$$u_{z'}^{(m)} = u_{z'0}^{(m)} - r^{(m)} \frac{\partial u_{x'}^{(m)}}{\partial z'} \quad , \tag{3.42}$$

where the superscript (m) indicates the mth wall of the MWNT with $r^{(m)}$ as its radius and $u_{z'0}$ is the longitudinal displacement of the center of the cylindrical cross-section. Under tension, bending moment and lateral shear force, the elongation of one wall relative to its neighboring wall is

$$\Delta_{z'}^{(m)} = u_{z'}^{(m+1)} - u_{z'}^{(m)} = r^{(m+1)} \frac{\partial u_{x'}^{(m+1)}}{\partial z'} - r^{(m)} \frac{\partial u_{x'}^{(m)}}{\partial z'} \approx (r^{(m+1)} - r^{(m)}) \frac{\partial \Delta_{x'}}{\partial s} \ , \tag{3.43}$$

where we assume $u_{x'}^{(m)} = u_{x'}^{(m+1)} = \Delta_{x'}$ as the lateral displacement as some function of tensile force or compression buckling or pressure in the thin film device. The lateral shear stress ($\tau_{vs}^{(m)}$) due to the van der Waals effect can now be written as

$$\tau_{vs}^{(m)} = C_{vs} \frac{\Delta_z^{(m)}}{\Delta_x} \ , \tag{3.44}$$

where $\mathrm{C_{vs}}$ is the van der Waals coefficient. Hence, the shear force per unit length can be obtained by integrating Eq. (3.44) over the individual wall circumferences and then by summing up for all the neighboring pair interactions, that is,

$$f_{vs} = \sum_m \int_0^{2\pi} C_{vs} \frac{\Delta_{z'}^{(m)}}{\Delta_{x'}} r_{\text{eff}} \, d\psi = \sum_m \int_0^{2\pi} C_{vs} \frac{\left(r^{(m+1)} - r^{(m)}\right) \frac{\partial \Delta_{x'}}{\partial s}}{\Delta_{x'}} \left(\frac{r^{(m+1)} + r^{(m)}}{2} \right) d\psi$$

$$\Rightarrow f_{vs} = \sum_m \pi C_{vs} [(r^{(m+1)})^2 - (r^{(m)})^2] \frac{1}{\Delta_{x'}} \frac{\partial \Delta_{x'}}{\partial s} \ . \tag{3.45}$$

The components of van der Waals force in the cell coordinate system (X', Z') is then obtained as

$$f_{vs_z} = f_{vs} \sin\theta(t) \ , \quad f_{vs_x} = f_{vs} \cos\theta(t) \ . \tag{3.46}$$

3.8 Dynamics of CNTs

The force components derived in the previous section are employed in the expression of work done on the ensemble of CNTs and formulate an energy conservation law (see e.g., ref. [116]). Under the assumption of small strain and small curvature, the longitudinal strain ε_{zz} (including thermal strain) and stress σ_{zz} can be written as, respectively,

$$\varepsilon_{zz} = \frac{\partial u_{z'0}^{(m)}}{\partial z'} - r^{(m)} \frac{\partial^2 u_{x'}^{(m)}}{\partial z'^2} + \alpha \Delta T(z') \ , \quad \sigma_{zz} = E' \varepsilon_{zz} \ , \tag{3.47}$$

where E' is the effective modulus of elasticity of CNTs under consideration, $\Delta T(z') = T(z') - T_0$ is the difference between the absolute temperature (T) during field emission and a reference temperature (T_0), and α is the effective coefficient of thermal expansion (longitudinal). The longitudinal strain and stress from Eq. (3.47) are employed in the strain energy expression. Subsequently, the kinetic energy is expressed in terms of the velocities $\dot{u}_{x'}$ and $\dot{u}_{z'}$. Next, by applying Hamilton's principle, we obtain the governing equations in $(u_{x'}, u_{z'})$ for each CNT, which can be expressed as, respectively,

$$E' A_2 \frac{\partial^4 u_{x'}}{\partial z'^4} + \rho A_0 \ddot{u}_{x'} - \rho A_2 \frac{\partial^2 \ddot{u}_{x'}}{\partial z'^2} - f_{x'} = 0 \ , \tag{3.48}$$

$$- E' A_0 \frac{\partial^2 u_{z'0}}{\partial z'^2} - \frac{E' A_0 \alpha}{2} \frac{\partial \Delta T(z')}{\partial z'} + \rho A_0 \ddot{u}_{z'0} - f_{z'} = 0 \ , \tag{3.49}$$

where A_2 is the second moment of cross-sectional area about Z-axis, A_0 is the effective cross-sectional area, and ρ is the mass per unit length of CNT. We assume fixed boundary conditions ($u = 0$) at the substrate-CNT interface ($z = 0$) and forced boundary conditions at the CNT tip ($z = h(t)$).

3.9 Thermodynamics of Electron-Phonon Interaction

During field emission, an electron flowing from the cathode substrate towards the anode along the CNT surface acquires energy and escapes from the tip region towards the anode by crossing the Fermi energy level. Thus, the thermodynamic process is similar to the thermionic emission, except that the temperature for thermionic emission is much higher than the temperature for field emission from CNTs. The energy lost in the replacement of the emitted electron is likely to create intense temperature gradient in the emitter [117]. For a metallic cone tip with hemispherical cap having $\approx 0.3\mu$m or smaller diameter, an empirical estimate of energy loss per emitted electron from the tip was reported to be $W = \Phi + \beta_1 kT$ (see [118]), where β_1 is a constant or an empirical function of temperature. On the other hand, due to particular atomic arrangement at the tip and the rolled graphene sheet in a CNT, the electrical potential across the CNT tip and hence the field emission characteristics are different than those due a metallic surface. Experimental studies using free-standing CNT shows that the temperature distribution is broadened as its length decreases [119] and most of the energy provided by the electric field to each electron is converted into phonons within the nanotube. This correlates well with the observations reported in [119] that the electron mean-free path is shorter than the Umklapp scattering mean-free path for inter-phonon scattering. Thus, a diffusive thermal transport model in the ballistic regime appears suitable to analyze the temperature rise in the CNTs. In the ballistic regime, the heat flux carried away by the phonons can be obtained by integrating the non-equilibrium phonon distribution associated with several photon modes [120]. Further simplification of this integral based on the analogy with the Landauer formula for ballistic conduction of electron leads to an approximate thermal conductance quantum $k_Q = \pi k^2 T/(6\hbar)$, where $\hbar = h/2\pi$ is the Dirac's constant. We employ this temperature dependent thermal conductance to derive the thermal transport model, which is discussed next. The heat flux in a CNT segment is first written as

$$dQ = I^2 \frac{\rho_c \pi d_t^2}{4L} dz' \ , \tag{3.50}$$

where I is the current, ρ_c is the electrical resistivity, and L is the length of the CNT. The current I and electrical resistivity ρ_c are expressed as

$$I = \pi d_t e \dot{\tilde{n}} \ , \quad \rho_c \approx \frac{E_{z'} l_e}{e \dot{\tilde{n}}} \ , \tag{3.51}$$

where l_e is the electron mean-free path. Next, the Fourier heat conduction can be expressed as

$$q_F = -k_Q \nabla T \ , \tag{3.52}$$

where k_Q is the thermal conductance quantum and is approximated as

$$k_Q = \frac{\pi k^2 T}{6\hbar} \ , \tag{3.53}$$

By considering the Fourier heat conduction and thermal radiation from the surface of CNT, the energy rate balance equation can be written as

$$dQ - \frac{\pi d_t^2}{4} dq_F - \pi d_t \sigma_{SB}(T^4 - T_0^4) dz' = \beta_{in} \frac{\partial T}{\partial t} dz' \ , \tag{3.54}$$

where σ_{SB} is the Stefan-Boltzmann constant and β_{in} is a constant. Here the emissivity is assumed to be unity. At the substrate-CNT interface ($z' = 0$), the boundary condition $T = T_0$ is applied and at the tip we assign a reported estimate of the power dissipated by phonons exiting the CNT tip to conductive flux, i.e., $q =$ at $z' = L$, where $M \approx 0.1875 kT d_t^2 / \hbar a_1 c$ and $c \approx 1.5 \times 10^4$ m/s is the in-plane speed of sound in graphite [45]. We assume $a_1{=}a_2{=}a_3$.

Equation (3.54) is discretized in $T(z')$ using a 4-point finite differencing scheme over each segment $0 \leq z' \leq L$. Note that in the developed model, the temperature distribution, the electron density, the displacement, and the electric field $E_{z'}$ are strongly coupled. This means that all the respective governing equations are to be solved simultaneously. Based on Eq. (3.27), we first compute $E_{z'}$ at the nodes, and then solve in ($\tilde{n}$, $u_{z'}$, $u_{x'}$, T). This is done at each time step $t_{i+1} = t_i + \Delta t$ and the state of each CNT is updated. The angle of orientation θ between the nodes $j+1$ and j at the two ends of a CNT segment of length Δs_j is expressed as

$$\theta(t) = \tan^{-1}\left(\frac{(x^{j+1} + u_x^{j+1}) - (x^j + u_x^j)}{(z^{j+1} + u_z^{j+1}) - (z^j + u_z^j)} \right) \ , \tag{3.55}$$

$$\begin{bmatrix} u_x^j \\ u_z^j \end{bmatrix} = [\Gamma(\theta(t - \Delta t)^j)] \begin{bmatrix} u_{x'}^j \\ u_{z'}^j \end{bmatrix} \ , \tag{3.56}$$

where Γ is the usual coordinate transformation matrix. Field emission current at each time step is calculated based on Eq. (3.28).

3.10 Conclusion

In this chapter, a multiphysics model has been proposed, which incorporates degradation, electrodynamic, mechanical, and thermodynamical phenomena during field emission. In particular, it is shown how the electric field, the electronic transport, the mechanical deformation of the CNTs, and the heat conduction in the CNTs due to ballistic phonon scattering are interrelated. The next chapter focusses on modeling the deformation of the CNT sheet due to electron gas flow on its surface.

Chapter 4

Modeling the Deformation due to Electron Gas Flow

4.1 Introduction

In the previous chapter, models for degradation, reorientations, electromechanical interactions among the CNTs in the film, and thermodynamics of electron-phonon interaction were developed. The objective of this chapter is by extending the model developed in Chapter 3 to include the deformation due to fluctuation of the CNT sheet under electron flow. This is done by developing a hydrodynamic model with mechanical coupling, which assumes a thin layer of electron gas at the surface of CNTs. The remainder of the chapter is organized as follows: a quantum-hydrodynamic model under realistic assumptions is developed in Section 4.2. In Section 4.3, the coupling between the quantum fluctuationand the electromagnetic field is modeled using Maxwell's equations. Governing equations for displacement due to fluctuation of CNT sheet are derived in Section 4.4. In Section 4.5, solution methodology using Fourier transforms for obtaining dispersion relation is described. The chapter ends with concluding remarks in Section 4.6.

4.2 Quantum-Hydrodynamic Formalism

In this study, the following assumptions have been made for the quantum-hydrodynamic formalism [121]:

(i) CNTs are deformed due to electrodynamic forces, thus changing the atomic coordinates leading to change in energy band structure;

(ii) The valence electrons flow as uniformly distributed electron gas over the cylindrical surface; and

(iii) An electromagnetic wave propagates along the CNT axis and perturbs the homogeneous electron gas density.

The hydrodynamic model for electron density on the CNT surface in (z', θ_0, r) coordinate system can be described by the continuity equation

$$\frac{\partial \tilde{n}}{\partial t} + \tilde{n}_0 \left(\frac{\partial \dot{u}^{(2)}_{z'}}{\partial z'} + \frac{1}{r} \frac{\partial \dot{u}^{(2)}_{\theta_0}}{\partial \theta_0} + \frac{\partial \dot{u}^{(2)}_{r}}{\partial r} \right) = 0 \tag{4.1}$$

and the momentum conservation equation

$$\begin{aligned} \frac{\partial^2 u^{(2)}_{z'}}{\partial t^2} = &-\frac{e}{m_e} E_{z'} - \frac{\alpha_2}{\tilde{n}_0} \frac{\partial \tilde{n}_1}{\partial z'} + \frac{\beta_2}{\tilde{n}_0} \frac{\partial^3 \tilde{n}_1}{\partial z'^3} + \frac{\beta_2}{\tilde{n}_0} \frac{\partial}{\partial z'} \left(\frac{\partial^2 \tilde{n}_1}{\partial r^2} \right) + \frac{\beta_2}{\tilde{n}_0} \frac{1}{r} \frac{\partial}{\partial z'} \left(\frac{\partial \tilde{n}_1}{\partial r} \right) \\ &+ \frac{\beta_2}{\tilde{n}_0} \frac{1}{r^2} \frac{\partial}{\partial z'} \left(\frac{\partial^2 \tilde{n}_1}{\partial \theta_0^2} \right) + \frac{f_{lz'}}{m_e} + \frac{f_{pz'}}{m_e} \, , \end{aligned} \tag{4.2}$$

$$\frac{\partial^2 u^{(2)}_{r}}{\partial t^2} = -\frac{e}{m_e} E_r - \frac{\alpha_2}{\tilde{n}_0} \frac{\partial \tilde{n}_1}{\partial r} + \frac{\beta_2}{\tilde{n}_0} \frac{\partial^3 \tilde{n}_1}{\partial r^3} + \frac{\beta_2}{\tilde{n}_0} \frac{1}{r} \frac{\partial^2 \tilde{n}_1}{\partial r^2} - \frac{\beta_2}{\tilde{n}_0} \frac{1}{r^2} \frac{\partial \tilde{n}_1}{\partial r} - \frac{\beta_2}{\tilde{n}_0} \frac{2}{r^3} \frac{\partial^2 \tilde{n}_1}{\partial \theta_0^2} + \frac{\beta_2}{\tilde{n}_0} \frac{1}{r^2} \frac{\partial}{\partial r} \left(\frac{\partial^2 \tilde{n}_1}{\partial \theta_0^2} \right)$$

$$+\frac{\beta_2}{\tilde{n}_0}\frac{\partial}{\partial r}\left(\frac{\partial^2\tilde{n}_1}{\partial z'^2}\right)+\frac{f_{lr}}{m_e}+\frac{f_{pr}}{m_e}\ , \tag{4.3}$$

$$\frac{\partial^2 u^{(2)}_{\theta_0}}{\partial t^2}=-\frac{e}{m_e}E_{\theta_0}-\frac{1}{r}\frac{\alpha_2}{\tilde{n}_0}\frac{\partial\tilde{n}_1}{\partial\theta_0}+\frac{\beta_2}{\tilde{n}_0}\frac{1}{r}\frac{\partial}{\partial\theta_0}\left(\frac{\partial^2\tilde{n}_1}{\partial r^2}\right)+\frac{\beta_2}{\tilde{n}_0}\frac{1}{r^2}\frac{\partial}{\partial\theta_0}\left(\frac{\partial\tilde{n}_1}{\partial r}\right)+\frac{\beta_2}{\tilde{n}_0}\frac{1}{r^3}\frac{\partial^3\tilde{n}_1}{\partial\theta_0^3}$$

$$+\frac{\beta_2}{\tilde{n}_0}\frac{1}{r}\frac{\partial}{\partial\theta_0}\left(\frac{\partial^2\tilde{n}_1}{\partial z'^2}\right)+\frac{f_{l\theta_0}}{m_e}+\frac{f_{p\theta_0}}{m_e}\ , \tag{4.4}$$

where m_e is the mass of the electron, α_2 is the speed of propagation of density disturbances, β_2 is the single electron excitation in the electron gas, f_l is the Lorentz force, f_p is the ponderomotive force, and $E_{z'}$, E_{θ_0} and E_r are the axial, circumferential and out-of-plane components of the electromagnetic field, respectively. The speed of propagation of density disturbances (α_2) is expressed in terms of the Fermi velocity (v_F) as [122]

$$\alpha_2=\frac{v_F^2}{2}\ , \tag{4.5}$$

The Fermi velocity is given by

$$v_F=(2\pi\tilde{n}_0 a_B^2)^{1/2}v_B\ , \tag{4.6}$$

where a_B and v_B are Bohr radius and Bohr velocity, respectively. The single electron excitation in the electron gas (β_2) is expressed as

$$\beta_2=\frac{(a_B v_B)^2}{4}\ , \tag{4.7}$$

In the present problem, it is assumed that the total fluctuation is the combined effect of the deformation of the CNT sheet and temperature fluctuation. Effect of temperature on $\tilde{n}$ is not directly taken into consideration. Instead, thermodynamics of electron-phonon is modeled separately in a decoupled manner through quantum thermal conductance (see Section 3.8). Under this condition, $\tilde{n}_0$ in this case is expressed as

$$\tilde{n}_0=\frac{kT_0}{\pi b^2\Delta}\ , \tag{4.8}$$

Next, the differential of Eq. (4.1) with respect to time can be written as

$$\frac{\partial^2 \tilde{n}}{\partial t^2}+\tilde{n}_0\left[\frac{\partial}{\partial z'}\left(\frac{\partial^2 u_{z'}^{(2)}}{\partial t^2}\right)+\frac{1}{r}\frac{\partial}{\partial \theta_0}\left(\frac{\partial^2 u_{\theta_0}^{(2)}}{\partial t^2}\right)+\frac{\partial}{\partial r}\left(\frac{\partial^2 u_{r}^{(2)}}{\partial t^2}\right)\right]=0 \tag{4.9}$$

As $\tilde{n}=\tilde{n}_0+\tilde{n}_1$ and $\partial\tilde{n}_0/\partial t=0$, one can write

$$\frac{\partial^2 \tilde{n}_1}{\partial t^2}+\tilde{n}_0\left[\frac{\partial}{\partial z'}\left(\frac{\partial^2 u_{z'}^{(2)}}{\partial t^2}\right)+\frac{1}{r}\frac{\partial}{\partial \theta_0}\left(\frac{\partial^2 u_{\theta_0}^{(2)}}{\partial t^2}\right)+\frac{\partial}{\partial r}\left(\frac{\partial^2 u_{r}^{(2)}}{\partial t^2}\right)\right]=0 \tag{4.10}$$

By substituting Eq. (4.2)-(4.4) in Eq. (4.10), we get

$$\begin{aligned}
&\frac{\partial^2 \tilde{n}_1}{\partial t^2}+\tilde{n}_0\Bigg[\frac{\partial}{\partial z'}\Bigg(-\frac{e}{m_e}E_{z'}-\frac{\alpha_2}{\tilde{n}_0}\frac{\partial \tilde{n}_1}{\partial z'}+\frac{\beta_2}{\tilde{n}_0}\frac{\partial^3 \tilde{n}_1}{\partial z'^3}+\frac{\beta_2}{\tilde{n}_0}\frac{\partial}{\partial z'}\left(\frac{\partial^2 \tilde{n}_1}{\partial r^2}\right)+\frac{\beta_2}{\tilde{n}_0}\frac{1}{r}\frac{\partial}{\partial z'}\left(\frac{\partial \tilde{n}_1}{\partial r}\right)\\
&+\frac{\beta_2}{\tilde{n}_0}\frac{1}{r^2}\frac{\partial}{\partial z'}\left(\frac{\partial^2 \tilde{n}_1}{\partial \theta_0^2}\right)+\frac{f_{lz'}}{m_e}+\frac{f_{pz'}}{m_e}\Bigg)+\frac{1}{r}\frac{\partial}{\partial \theta_0}\Bigg(-\frac{e}{m_e}E_{\theta_0}-\frac{1}{r}\frac{\alpha_2}{\tilde{n}_0}\frac{\partial \tilde{n}_1}{\partial \theta_0}+\frac{\beta_2}{\tilde{n}_0}\frac{1}{r}\frac{\partial}{\partial \theta_0}\left(\frac{\partial^2 \tilde{n}_1}{\partial r^2}\right)\\
&+\frac{\beta_2}{\tilde{n}_0}\frac{1}{r^2}\frac{\partial}{\partial \theta_0}\left(\frac{\partial \tilde{n}_1}{\partial r}\right)+\frac{\beta_2}{\tilde{n}_0}\frac{1}{r^3}\frac{\partial^3 \tilde{n}_1}{\partial \theta_0^3}+\frac{\beta_2}{\tilde{n}_0}\frac{1}{r}\frac{\partial}{\partial \theta_0}\left(\frac{\partial^2 \tilde{n}_1}{\partial z'^2}\right)+\frac{f_{l\theta_0}}{m_e}+\frac{f_{p\theta_0}}{m_e}\Bigg)+\frac{\partial}{\partial r}\Bigg(-\frac{e}{m_e}E_r\\
&\quad-\frac{\alpha_2}{\tilde{n}_0}\frac{\partial \tilde{n}_1}{\partial r}+\frac{\beta_2}{\tilde{n}_0}\frac{\partial^3 \tilde{n}_1}{\partial r^3}+\frac{\beta_2}{\tilde{n}_0}\frac{1}{r}\frac{\partial^2 \tilde{n}_1}{\partial r^2}-\frac{\beta_2}{\tilde{n}_0}\frac{1}{r^2}\frac{\partial \tilde{n}_1}{\partial r}-\frac{\beta_2}{\tilde{n}_0}\frac{2}{r^3}\frac{\partial^2 \tilde{n}_1}{\partial \theta_0^2}+\frac{\beta_2}{\tilde{n}_0}\frac{1}{r^2}\frac{\partial}{\partial r}\left(\frac{\partial^2 \tilde{n}_1}{\partial \theta_0^2}\right)\\
&\qquad+\frac{\beta_2}{\tilde{n}_0}\frac{\partial}{\partial r}\left(\frac{\partial^2 \tilde{n}_1}{\partial z'^2}\right)+\frac{f_{lr}}{m_e}+\frac{f_{pr}}{m_e}\Bigg)\Bigg]=0
\end{aligned} \tag{4.11}$$

When interpreted physically, the terms $\partial\tilde{n}_1/\partial r$, $\partial^2\tilde{n}_1/\partial r^2$, $\partial^3\tilde{n}_1/\partial r^3$, $\frac{\partial}{\partial r}\left(\partial^2\tilde{n}_1/\partial\theta_0^2\right)$ and $\frac{\partial}{\partial r}\left(\partial^2\tilde{n}_1/\partial z'^2\right)$ are equal to zero. Therefore, Eq. (4.11) is reduced to

$$\begin{aligned}
&\frac{\partial^2 \tilde{n}_1}{\partial t^2}-\frac{e\tilde{n}_0}{m_e}\frac{\partial E_{z'}}{\partial z'}-\alpha_2\frac{\partial^2 \tilde{n}_1}{\partial z'^2}+\beta_2\frac{\partial^4 \tilde{n}_1}{\partial z'^4}+\frac{\beta_2}{r^2}\frac{\partial^2}{\partial z'^2}\left(\frac{\partial^2 \tilde{n}_1}{\partial \theta_0^2}\right)+\frac{n_0}{m_e}\frac{\partial f_{lz'}}{\partial z'}-\frac{e\tilde{n}_0}{m_e}\frac{1}{r}\frac{\partial E_{\theta_0}}{\partial \theta_0}\\
&-\frac{\alpha_2}{r^2}\frac{\partial^2 \tilde{n}_1}{\partial \theta_0^2}+\frac{\beta_2}{r^4}\frac{\partial^4 \tilde{n}_1}{\partial \theta_0^4}+\frac{\beta_2}{r^2}\frac{\partial^2}{\partial \theta_0^2}\left(\frac{\partial^2 \tilde{n}_1}{\partial z'^2}\right)+\frac{n_0}{m_e}\frac{1}{r}\frac{\partial f_{l\theta_0}}{\partial \theta_0}-\frac{en_0}{m_e}\frac{\partial E_r}{\partial r}+\frac{n_0}{m_e}\frac{\partial f_{lr}}{\partial r}+\frac{n_0}{m_e}\frac{\partial f_{pr}}{\partial r}=0
\end{aligned} \tag{4.12}$$

The coupling between the quantum fluctuation and the electromagnetic field is modeled next.

4.3 Maxwellian Electromagnetics

In order to introduce coupling between the quantum fluctuation and the electromagnetic field, we consider the Maxwell's equations in general form, which is combined to the following form:

$$\nabla^2 E - \mu\sigma\frac{\partial E}{\partial t} - \mu\epsilon\frac{\partial^2 E}{\partial t^2} = \mu\frac{\partial J}{\partial t} \ , \tag{4.13}$$

where μ, σ, ϵ, and J are permeability, conductivity, permittivity, and current density, respectively. In this study, magnetic field fluctuation is neglected for simplicity. In the present case, the current density in the CNT sheet is given by

$$J = e\tilde{n}\frac{\partial u_{z'}^{(2)}}{\partial t}, \tag{4.14}$$

Therefore, by simplifying Eq. (4.13) further, one can obtain the equations in (z', θ_0, r) coordinate system as

$$\frac{\partial^2 E_{z'}(r)}{\partial z'^2} + \frac{1}{r^2}\frac{\partial^2 E_{z'}(r)}{\partial \theta_0^2} + \frac{1}{r}\frac{\partial}{\partial r}\left(r\frac{\partial E_{z'}(r)}{\partial r}\right) - \mu\sigma\frac{\partial E_{z'}(r)}{\partial t} - \mu\epsilon\frac{\partial^2 E_{z'}(r)}{\partial t^2} = \mu\frac{\partial}{\partial t}\left(e\tilde{n}\frac{\partial u_{z'}^{(2)}}{\partial t}\right) \ , \tag{4.15}$$

$$\frac{\partial^2 E_{\theta_0}(r)}{\partial z'^2} + \frac{1}{r^2}\frac{\partial^2 E_{\theta_0}(r)}{\partial \theta_0^2} + \frac{1}{r}\frac{\partial}{\partial r}\left(r\frac{\partial E_{\theta_0}(r)}{\partial r}\right) - \mu\sigma\frac{\partial E_{\theta_0}(r)}{\partial t} - \mu\epsilon\frac{\partial^2 E_{\theta_0}(r)}{\partial t^2} = 0 \ , \tag{4.16}$$

$$\frac{\partial^2 E_r(r)}{\partial z'^2} + \frac{1}{r^2}\frac{\partial^2 E_r(r)}{\partial \theta_0^2} + \frac{1}{r}\frac{\partial}{\partial r}\left(r\frac{\partial E_r(r)}{\partial r}\right) - \mu\sigma\frac{\partial E_r(r)}{\partial t} - \mu\epsilon\frac{\partial^2 E_r(r)}{\partial t^2} = 0 \ , \tag{4.17}$$

Next, we employ the concepts of structural mechanics to model the displacement due to fluctuation of CNT sheet.

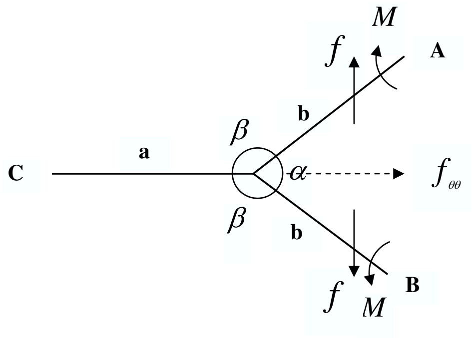

Figure 4.1: Analytical model for tension of a CNT.

4.4 Displacement due to Fluctuation of the CNT Sheet

In order to obtain the governing equations for displacement, we consider a CNT subjected to a longitudinal tensile loading. Torsion loadings on CNTs have not been considered in this study. Fig. 4.1 represents an analytical model for tension of a CNT with bond lengths a, b, b, and three bond angles α, β, β resulting from a bond elongation Δa and two bond angle variances $\Delta\alpha$ and $\Delta\beta$. By considering the equilibrium of the CNT structure, the relationship between stress and the bond stretch and bond angle variation can be determined as described next.

In the tensile response model, for axial equilibrium, the stretch force can be expressed as

$$f sin(\alpha/2) = 2\beta_3 D_e(1 - e^{-\beta_3\Delta b})e^{-\beta_3\Delta b} \ , \tag{4.18}$$

where the right hand side of the above equation is obtained from differentiation of the modified Morse potential defined by Xiao *et al.* [123]. In Eq. (4.18), D_e and β_3 are parameters calibrated by Belytschko *et al.* [67] with the Brenner potential.

The value of $\mathrm{D_e}$ and β_3 are 0.6031 nN.nm and 26.25 nm^{-1}, respectively. Therefore,

$$f = \frac{2\beta_3 D_e(1 - e^{-\beta_3 \Delta b})e^{-\beta_3 \Delta b}}{sin(\alpha/2)} \ , \tag{4.19}$$

The axial stress ($\sigma_{z'z'}$), the circumferential stress ($\sigma_{\theta_0\theta_0}$), and the shear stress ($\tau_{\theta_0 z'}$) in the CNT can be defined as, respectively,

$$\sigma_{z'z'} = \frac{f}{t_h b(1+\cos(\alpha/2))} \ , \tag{4.20}$$

$$\sigma_{\theta_0\theta_0} = \frac{f_{\theta_0\theta_0}}{t_h b(1+\cos(\alpha/2))} = \frac{f \sin\beta}{t_h b \sin(\alpha/2)(1+\cos(\alpha/2))} \ , \tag{4.21}$$

$$\tau_{\theta_0 z'} = \frac{f}{t_h a(1+\cos(\alpha/2))} \ , \tag{4.22}$$

where t_h is the thickness of CNT. After substituting the value of f from Eq. (4.19) and using the first order approximation, the three stresses can be expressed as

$$\sigma_{z'z'} = \frac{2\beta_3^2 D_e}{t_h b \sin(\alpha/2)(1+\cos(\alpha/2))}\Delta b \ , \tag{4.23}$$

$$\sigma_{\theta_0\theta_0} = \frac{2\beta_3^2 D_e \sin\beta}{t_h b \sin^2(\alpha/2)(1+\cos(\alpha/2))}\Delta b \ . \tag{4.24}$$

$$\tau_{\theta_0 z'} = \frac{2\beta_3^2 D_e}{t_h a \sin(\alpha/2)(1+\cos(\alpha/2))}\Delta a \ , \tag{4.25}$$

Arranging Eqs. (4.23)-(4.25) in the matrix form, one can write

$$\begin{bmatrix} \sigma_{z'z'} \\ \sigma_{\theta_0\theta_0} \\ \tau_{\theta_0 z'} \end{bmatrix} = \begin{bmatrix} 0 & \frac{2\beta_3^2 D_e}{t_h b \sin(\alpha/2)(1+\cos(\alpha/2))} & 0 \\ 0 & \frac{2\beta_3^2 D_e \sin\beta}{t_h b \sin^2(\alpha/2)(1+\cos(\alpha/2))} & 0 \\ \frac{2\beta_3^2 D_e}{t_h a \sin(\alpha/2)(1+\cos(\alpha/2))} & 0 & 0 \end{bmatrix} \begin{bmatrix} \Delta a \\ \Delta b \\ \Delta\alpha \end{bmatrix} \ , \tag{4.26}$$

Next, the strains of CNTs can be calculated as, respectively,

$$\varepsilon_{z'z'} = \frac{\Delta b \sin(\alpha/2)}{b \sin(\alpha/2)} + \frac{\cos(\alpha/2)\Delta\alpha}{2\sin(\alpha/2)} \ , \tag{4.27}$$

$$\varepsilon_{\theta_0\theta_0} = \frac{\Delta b \cos(\alpha/2)}{a + b\cos(\alpha/2)} - \frac{b \sin(\alpha/2)\Delta\alpha}{2(a + b\cos(\alpha/2))} \ , \tag{4.28}$$

$$\gamma_{\theta_0 z'} = \frac{c\Delta\beta + \Delta b\sin(\alpha/2)}{a(1+\cos(\alpha/2))} + \frac{(\Delta a + \Delta b)\cos(\alpha/2)}{2b\sin(\alpha/2)} \ , \tag{4.29}$$

where $\varepsilon_{z'z'}$ is axial strain, $\varepsilon_{\theta_0\theta_0}$ is circumferential strain and $\gamma_{\theta_0 z'}$ is shear strain. By expressing Eqs. (4.27)-(4.29) in matrix form, one can write

$$\begin{bmatrix} \varepsilon_{z'z'} \\ \varepsilon_{\theta_0\theta_0} \\ \gamma_{\theta_0 z'} \end{bmatrix} = \begin{bmatrix} 0 & \frac{1}{b} & \frac{\cot(\alpha/2)}{2} \\ 0 & \frac{\cos(\alpha/2)}{a+b\cos(\alpha/2)} & -\frac{b\sin(\alpha/2)}{2(a+b\cos(\alpha/2))} \\ \frac{\cot(\alpha/2)}{2b} & \frac{\cot(\alpha/2)}{2b} + \frac{\sin(\alpha/2)}{a(1+\cos(\alpha/2))} & -\frac{c\sin(\alpha/2)\cos(\pi/2n_1)}{2a(1+\cos(\alpha/2))\sin\beta} \end{bmatrix} \begin{bmatrix} \Delta a \\ \Delta b \\ \Delta\alpha \end{bmatrix} , \tag{4.30}$$

The relationship between the stresses and respective strains is given by

$$\sigma_{z'z'} = c_{11}\varepsilon_{z'z'} + c_{12}\varepsilon_{\theta_0\theta_0} + c_{13}\gamma_{\theta_0 z'} \ , \tag{4.31}$$

$$\sigma_{\theta_0\theta_0} = c_{21}\varepsilon_{z'z'} + c_{22}\varepsilon_{\theta_0\theta_0} + c_{23}\gamma_{\theta_0 z'} \ , \tag{4.32}$$

$$\tau_{\theta_0 z'} = c_{31}\varepsilon_{z'z'} + c_{32}\varepsilon_{\theta_0\theta_0} + c_{33}\gamma_{\theta_0 z'} \ , \tag{4.33}$$

where the terms c_{11} to c_{33} are parameters, whose values depend on $\mathrm{D_e}$, β, t_h, b and α. Rearranging Eqs. (4.31)-(4.33) into matrix form, one can write

$$\begin{bmatrix} \sigma_{z'z'} \\ \sigma_{\theta_0\theta_0} \\ \tau_{\theta_0 z'} \end{bmatrix} = \begin{bmatrix} c_{11} & c_{12} & c_{13} \\ c_{21} & c_{22} & c_{23} \\ c_{31} & c_{32} & c_{33} \end{bmatrix} \begin{bmatrix} \varepsilon_{z'z'} \\ \varepsilon_{\theta_0\theta_0} \\ \gamma_{\theta_0 z'} \end{bmatrix} \ , \tag{4.34}$$

From Eqs. (4.26), (4.30) and (4.34), we get

$$\begin{gathered} \begin{bmatrix} 0 & \frac{2\beta_3^2 D_e}{t_h b\sin(\alpha/2)(1+\cos(\alpha/2))} & 0 \\ 0 & \frac{2\beta_3^2 D_e\sin\beta}{t_h b\sin^2(\alpha/2)(1+\cos(\alpha/2))} & 0 \\ \frac{2\beta_3^2 D_e}{t_h a\sin(\alpha/2)(1+\cos(\alpha/2))} & 0 & 0 \end{bmatrix} = \begin{bmatrix} c_{11} & c_{12} & c_{13} \\ c_{21} & c_{22} & c_{23} \\ c_{31} & c_{32} & c_{33} \end{bmatrix} \\ \begin{bmatrix} 0 & \frac{1}{b} & \frac{\cot(\alpha/2)}{2} \\ 0 & \frac{\cos(\alpha/2)}{a+b\cos(\alpha/2)} & -\frac{b\sin(\alpha/2)}{2(a+b\cos(\alpha/2))} \\ \frac{\cot(\alpha/2)}{2b} & \frac{\cot(\alpha/2)}{2b} + \frac{\sin(\alpha/2)}{a(1+\cos(\alpha/2))} & -\frac{c\sin(\alpha/2)\cos(\pi/2n_1)}{2a(1+\cos(\alpha/2))\sin\beta} \end{bmatrix} , \end{gathered} \tag{4.35}$$

Now, comparing term by term of both the sides in Eq. (4.35), one can write

$$c_{11} = \frac{2\beta_3^2 D_e \sin(\alpha/2)}{t_h(1+\cos(\alpha/2))} \tag{4.36}$$

$$c_{12} = \frac{2\beta_3^2 D_e \cos(\alpha/2)(a+b\cos(\alpha/2))}{t_h b \sin(\alpha/2)(1+\cos(\alpha/2))} \tag{4.37}$$

$$c_{13} = 0 \tag{4.38}$$

$$c_{21} = \frac{2\beta_3^2 D_e \sin\beta}{t_h(1+\cos(\alpha/2))} \tag{4.39}$$

$$c_{22} = \frac{2\beta_3^2 D_e \sin\beta\cos(\alpha/2)(a+b\cos(\alpha/2))}{t_h b \sin^2(\alpha/2)(1+\cos(\alpha/2))} \tag{4.40}$$

$$c_{23} = 0 \tag{4.41}$$

$$\begin{aligned} c_{31} = &-\frac{2\beta_3^2 D_e \cos(\alpha/2)(a+b\cos(\alpha/2))}{t_h a(1+\cos(\alpha/2))}\frac{b\sin(\alpha/2)}{\cot(\alpha/2)(a+b\cos(\alpha/2))} \\ &\left(\frac{2c\sin^2(\alpha/2)\cos(\pi/2n_1)}{a\cos^2(\alpha/2)\sin\beta(1+\cos(\alpha/2))} + \frac{1}{\sin(\alpha/2)} + \frac{2b\sin(\alpha/2)}{a\cos(\alpha/2)(1+\cos(\alpha/2))}\right) \\ &+ \frac{4\beta_3^2 bcD_e \sin(\alpha/2)\cos(\pi/2n_1)}{t_h a^2 \cot(\alpha/2)\cos(\alpha/2)\sin\beta(1+\cos(\alpha/2))^2} \end{aligned} \tag{4.42}$$

$$\begin{aligned} c_{32} = &-\frac{2\beta_3^2 D_e \cos(\alpha/2)(a+b\cos(\alpha/2))}{t_h a(1+\cos(\alpha/2))}\left(\frac{2c\sin^2(\alpha/2)\cos(\pi/2n_1)}{a\cos^2(\alpha/2)\sin\beta(1+\cos(\alpha/2))} + \frac{1}{\sin(\alpha/2)}\right. \\ &\left. + \frac{2b\sin(\alpha/2)}{a\cos(\alpha/2)(1+\cos(\alpha/2))}\right) \end{aligned} \tag{4.43}$$

$$c_{33} = \frac{4\beta_3^2 b D_e}{t_h a\cos(\alpha/2)(1+\cos(\alpha/2))} \tag{4.44}$$

The details of all the derivations are presented in Appendix B. Next, the relationship between the strains and displacements can be defined as

$$\varepsilon_{z'z'} = \frac{\partial u_{z'}^{(2)}}{\partial z'} \tag{4.45}$$

$$\varepsilon_{\theta_0\theta_0} = \frac{u_r^{(2)}}{r} + \frac{1}{r}\frac{\partial u_{\theta_0}^{(2)}}{\partial \theta_0} \tag{4.46}$$

$$\gamma_{\theta_0 z'} = \frac{1}{r}\frac{\partial u_{z'}^{(2)}}{\partial \theta_0} + \frac{\partial u_{\theta_0}^{(2)}}{\partial z'} \tag{4.47}$$

From Eqs. (4.31)-(4.33) and Eqs. (4.45)-(4.47), the relationship between stresses and displacements can be expressed as, respectively,

$$\sigma_{z'z'} = c_{11}\frac{\partial u_{z'}^{(2)}}{\partial z'} + c_{12}\left(\frac{u_r^{(2)}}{r} + \frac{1}{r}\frac{\partial u_{\theta_0}^{(2)}}{\partial \theta_0}\right) + c_{13}\left(\frac{1}{r}\frac{\partial u_{z'}^{(2)}}{\partial \theta_0} + \frac{\partial u_{\theta_0}^{(2)}}{\partial z'}\right) \tag{4.48}$$

$$\sigma_{\theta_0\theta_0} = c_{21}\frac{\partial u_{z'}^{(2)}}{\partial z'} + c_{22}\left(\frac{u_r^{(2)}}{r} + \frac{1}{r}\frac{\partial u_{\theta_0}^{(2)}}{\partial \theta_0}\right) + c_{23}\left(\frac{1}{r}\frac{\partial u_{z'}^{(2)}}{\partial \theta_0} + \frac{\partial u_{\theta_0}^{(2)}}{\partial z'}\right) \tag{4.49}$$

$$\tau_{\theta_0 z'} = c_{31}\frac{\partial u_{z'}^{(2)}}{\partial z'} + c_{32}\left(\frac{u_r^{(2)}}{r} + \frac{1}{r}\frac{\partial u_{\theta_0}^{(2)}}{\partial \theta_0}\right) + c_{33}\left(\frac{1}{r}\frac{\partial u_{z'}^{(2)}}{\partial \theta_0} + \frac{\partial u_{\theta_0}^{(2)}}{\partial z'}\right) \tag{4.50}$$

Now, we consider the equilibrium equations in cylindrical coordinates, which can be expressed as

$$\frac{1}{r}\frac{\partial \sigma_{\theta_0\theta_0}}{\partial \theta_0} + \frac{\partial \tau_{\theta_0 z'}}{\partial z'} + e\tilde{n}_0 E_{\theta_0} = \frac{\partial^2 u_{\theta_0}^{(2)}}{\partial t^2}\ , \tag{4.51}$$

$$\frac{\partial \sigma_{rr}}{\partial r} + \frac{\sigma_{rr} - \sigma_{\theta_0\theta_0}}{r} + e\tilde{n}_0 E_r = \frac{\partial^2 u_r^{(2)}}{\partial t^2}\ , \tag{4.52}$$

$$\frac{\partial \sigma_{z'z'}}{\partial z'} + \frac{1}{r}\frac{\partial \tau_{\theta_0 z'}}{\partial \theta_0} + e\tilde{n}_0 E_{z'} = \frac{\partial^2 u_{z'}^{(2)}}{\partial t^2}\ , \tag{4.53}$$

where σ_{rr} is out-of-plane stress and it is expressed as

$$\sigma_{rr} = -\frac{2k_3}{3\sqrt{3}a^2}\frac{\partial^2 u_r^{(2)}}{\partial s^2}\left(1 + 2\cos(\bar{\alpha}/2)\right)^2\ , \tag{4.54}$$

The steps for derivation of σ_{rr} are outlined in Appendix C. From Eqs. (4.48)-(4.50) and Eqs. (4.51)-(4.53), the displacement equations are obtained as, respectively,

$$\begin{aligned} &c_{21}\frac{1}{r}\frac{\partial}{\partial \theta_0}\left(\frac{\partial u_{z'}^{(2)}}{\partial z'}\right) + c_{22}\frac{1}{r^2}\frac{\partial u_r^{(2)}}{\partial \theta_0} + c_{22}\frac{1}{r^2}\frac{\partial^2 u_{\theta_0}^{(2)}}{\partial \theta_0^2} + c_{31}\frac{\partial^2 u_{z'}^{(2)}}{\partial z'^2} + c_{32}\frac{1}{r}\frac{\partial u_r^{(2)}}{\partial z'} \\ &+ c_{32}\frac{1}{r}\frac{\partial}{\partial z'}\left(\frac{\partial u_{\theta_0}^{(2)}}{\partial \theta_0}\right) + c_{33}\frac{1}{r}\frac{\partial}{\partial z'}\left(\frac{\partial u_{z'}^{(2)}}{\partial \theta_0}\right) + c_{33}\frac{\partial^2 u_{\theta_0}^{(2)}}{\partial z'^2} + e\tilde{n}_0 E_{\theta_0} = \frac{\partial^2 u_{\theta_0}^{(2)}}{\partial t^2}\ , \end{aligned} \tag{4.55}$$

$$\frac{2k_3}{3\sqrt{3}a^2}(1+2\cos(\bar{\alpha}/2))^2\frac{1}{r^3}\frac{\partial^2 u_r^{(2)}}{\partial\theta_0^2} - c_{21}\frac{1}{r}\frac{\partial u_{z'}^{(2)}}{\partial z'} - c_{22}\frac{u_r^{(2)}}{r^2} - c_{22}\frac{1}{r^2}\frac{\partial u_{\theta_0}^{(2)}}{\partial\theta_0} - c_{23}\frac{1}{r^2}\frac{\partial u_{z'}^{(2)}}{\partial\theta_0}$$
$$- c_{23}\frac{1}{r}\frac{\partial u_{\theta_0}^{(2)}}{\partial z'} + e\tilde{n}_0 E_r = \frac{\partial^2 u_r^{(2)}}{\partial t^2}\ , \tag{4.56}$$

$$c_{11}\frac{\partial^2 u_{z'}^{(2)}}{\partial z'^2} + c_{12}\frac{1}{r}\frac{\partial u_r^{(2)}}{\partial z'} + c_{12}\frac{1}{r}\frac{\partial}{\partial z'}\left(\frac{\partial u_{\theta_0}^{(2)}}{\partial\theta_0}\right) + c_{13}\frac{1}{r}\frac{\partial}{\partial z'}\left(\frac{\partial u_{z'}^{(2)}}{\partial\theta_0}\right) + c_{13}\frac{\partial^2 u_{\theta_0}^{(2)}}{\partial z'^2}$$
$$+c_{31}\frac{1}{r}\frac{\partial}{\partial\theta_0}\left(\frac{\partial u_{z'}^{(2)}}{\partial z'}\right) + c_{32}\frac{1}{r^2}\frac{\partial u_r^{(2)}}{\partial\theta_0} + c_{32}\frac{1}{r^2}\frac{\partial^2 u_{\theta_0}^{(2)}}{\partial\theta_0^2} + c_{33}\frac{1}{r^2}\frac{\partial^2 u_{z'}^{(2)}}{\partial\theta_0^2} + c_{33}\frac{1}{r}\frac{\partial}{\partial\theta_0}\left(\frac{\partial u_{\theta_0}^{(2)}}{\partial z'}\right)$$
$$+ e\tilde{n}_0 E_{z'} = \frac{\partial^2 u_{z'}^{(2)}}{\partial t^2}\ , \tag{4.57}$$

The solution methodology using field approximation is described next.

4.5 Field Approximation

In the theoretical model of the electron-phonon interaction, we have eight partial differential equations. By using space-time Fourier transforms, the variables $E_{z'}(r)$, $E_{\theta_0}(r)$, $E_r(r)$, $\tilde{n}_1$, $u_{z'}^{(2)}$, $u_{\theta_0}^{(2)}$, $u_r^{(2)}$ and T can be expanded as, respectively,

$$E_{z'}(r) = \sum_k \tilde{E}_{z'_k}(r)e^{j(m_k\theta_0+q_kz'-\omega_kt)} \tag{4.58}$$

$$E_{\theta_0}(r) = \sum_k \tilde{E}_{\theta_{0_k}}(r)e^{j(m_k\theta_0+q_kz'-\omega_kt)} \tag{4.59}$$

$$E_r(r) = \sum_k \tilde{E}_{r_k}(r)e^{j(m_k\theta_0+q_kz'-\omega_kt)} \tag{4.60}$$

$$\tilde{n}_1 = \sum_k \tilde{\tilde{n}}_{1_k}e^{j(m_k\theta_0+q_kz'-\omega_kt)} \tag{4.61}$$

$$u_{z'}^{(2)} = \sum_k \tilde{u}_{z'_k}^{(2)}e^{j(m_k\theta_0+q_kz'-\omega_kt)} \tag{4.62}$$

$$u_{\theta_0}^{(2)} = \sum_k \tilde{u}_{\theta_{0_k}}^{(2)}e^{j(m_k\theta_0+q_kz'-\omega_kt)} \tag{4.63}$$

$$u_r^{(2)} = \sum_k \tilde{u}_{r_k}^{(2)} e^{j(m_k\theta_0 + q_k z' - \omega_k t)} \tag{4.64}$$

$$T = \sum_k \tilde{T}_k e^{j(m_k\theta_0 + q_k z' - \omega_k t)} \tag{4.65}$$

where m_k and q_k are radial and axial wave numbers, respectively, and ω_k is the frequency of the electromagnetic wave. By neglecting nonlinear terms in the governing equations and by substituting Fourier transformations into these equations, we get the dispersion equation, which is expressed as

$$\begin{bmatrix} a_{11} & 0 & 0 & 0 & 0 & 0 & 0 & 0 \\ 0 & a_{22} & 0 & 0 & 0 & a_{26} & a_{27} & a_{28} \\ 0 & 0 & a_{33} & a_{34} & a_{35} & a_{36} & 0 & 0 \\ 0 & 0 & a_{43} & a_{44} & a_{45} & 0 & a_{47} & 0 \\ 0 & 0 & a_{53} & a_{54} & a_{55} & 0 & 0 & a_{58} \\ 0 & 0 & 0 & 0 & 0 & a_{66} & 0 & 0 \\ 0 & 0 & 0 & 0 & 0 & 0 & a_{77} & 0 \\ 0 & 0 & 0 & 0 & 0 & 0 & 0 & a_{88} \end{bmatrix} \begin{bmatrix} \tilde{T}_k \\ \tilde{\tilde{n}}_{1_k} \\ \tilde{u}_{z'_k}^{(2)} \\ \tilde{u}_{r_k}^{(2)} \\ \tilde{u}_{\theta_{0_k}}^{(2)} \\ \tilde{\tilde{E}}_{z'_k} \\ \tilde{\tilde{E}}_{r_k} \\ \tilde{\tilde{E}}_{\theta_{0_k}} \end{bmatrix} = 0\ , \tag{4.66}$$

where the terms $\tilde{\tilde{E}}_{z'_k}$, $\tilde{\tilde{E}}_{\theta_{0_k}}$ and $\tilde{\tilde{E}}_{r_k}$ are defined as

$$\tilde{\tilde{E}}_{z'_k} = \frac{\tilde{E}_{z'_k}}{J_{m_k}(r)} \tag{4.67}$$

$$\tilde{\tilde{E}}_{\theta_{0_k}} = \frac{\tilde{E}_{\theta_{0_k}}}{J_{m_k}(r)} \tag{4.68}$$

$$\tilde{\tilde{E}}_{r_k} = \frac{\tilde{E}_{r_k}}{J_{m_k}(r)} \tag{4.69}$$

and J_{m_k} is the Bessel solution of the first kind and is expressed as

$$J_{m_k}(r) = \sum_{p=0}^{\infty} \frac{(-1)^p \left[\frac{r}{2}(\mu\sigma j\omega_k + \mu\epsilon\omega_k^2 - q_k)^{1/2}\right]^{(m_k+2p)}}{p!\Gamma(m_k+p+1)} \tag{4.70}$$

The steps for deriving the Bessel form are detailed in Appendix D. The non-zero terms in the matrix in Eq. (4.66) are

$$a_{11} = k_Q q_k^2 + \beta_{in} k j \omega_k \ ,$$

$$a_{22} = \alpha_2 q_k^2 + \beta_2 q_k^4 + \frac{2}{R^2}\beta_2 m_k^2 q_k^2 + + \frac{1}{R^2}\alpha_2 m_k^2 + \frac{1}{R^4}\beta_2 m_k^4 - \omega_k^2 \ ,$$

$$a_{26} = \frac{e\tilde{n}_0}{m_e} j q_k J_{m_k}(R)\Big(\tilde{n}_0 - 1\Big) \ ,$$

$$a_{27} = \frac{e\tilde{n}_0}{m_e}\Big(\tilde{n}_0 - 1\Big)\dot{J}_{m_k}(r) \ ,$$

$$a_{28} = \frac{e\tilde{n}_0}{m_e}\frac{1}{R} j m_k J_{m_k}(R)\Big(\tilde{n}_0 - 1\Big) \ ,$$

$$a_{33} = -c_{11}q_k^2 + c_{13}\frac{1}{R} j m_k j q_k + c_{31}\frac{1}{R} j m_k j q_k - c_{33}\frac{1}{R^2} m_k^2 + \omega_k^2,$$

$$a_{34} = c_{12}\frac{1}{R} j q_k + c_{32}\frac{1}{R^2} j m_k,$$

$$a_{35} = c_{12}\frac{1}{R} j m_k j q_k - c_{13} q_k^2 - c_{32}\frac{1}{R^2} m_k^2 + c_{33}\frac{1}{R} j m_k j q_k,$$

$$a_{36} = e\tilde{n}_0 J_{m_k}(R),$$

$$a_{43} = -c_{21}\frac{1}{R} j q_k - c_{23}\frac{1}{R^2} j m_k,$$

$$a_{44} = -\frac{2k_3}{3\sqrt{3}a^2}\frac{1}{R^3} m_k^2\Big(1 + 2\cos(\bar{\alpha}/2)\Big)^2 - c_{22}\frac{1}{R^2} + \omega_k^2,$$

$$a_{45} = -c_{22}\frac{1}{R^2} j m_k - c_{23}\frac{1}{R} j q_k,$$

$$a_{47} = e\tilde{n}_0 J_{m_k}(R),$$

$$a_{53} = -c_{21}\frac{1}{R} q_k m_k - c_{31} q_k^2 - c_{33}\frac{1}{R} q_k m_k,$$

$$a_{54} = c_{22}\frac{1}{R^2} j m_k + c_{32}\frac{1}{R} j q_k,$$

$$a_{55} = -c_{22}\frac{1}{R^2} m_k^2 - c_{32}\frac{1}{R} q_k m_k - c_{33} q_k^2 + \omega_k^2,$$

$$a_{58} = e\tilde{n}_0 J_{m_k}(R) \ ,$$

$$a_{66} = \ddot{J}_{m_k}(r) + \frac{1}{R}\dot{J}_{m_k}(r) - \frac{1}{R^2}m_k^2 J_{m_k}(R) - q_k^2 J_{m_k}(R) + \mu\sigma j\omega_k J_{m_k}(R) + \mu\epsilon\omega_k^2 J_{m_k}(R),$$

$$a_{77} = \ddot{J}_{m_k}(r) + \frac{1}{R}\dot{J}_{m_k}(r) - \frac{1}{R^2}m_k^2 J_{m_k}(R) - q_k^2 J_{m_k}(R) + \mu\sigma j\omega_k J_{m_k}(R) + \mu\epsilon\omega_k^2 J_{m_k}(R),$$

$$a_{88} = \ddot{J}_{m_k}(r) + \frac{1}{R}\dot{J}_{m_k}(r) - \frac{1}{R^2}m_k^2 J_{m_k}(R) - q_k^2 J_{m_k}(R) + \mu\sigma j\omega_k J_{m_k}(R) + \mu\epsilon\omega_k^2 J_{m_k}(R)\ ,$$

Eq. (4.66) represents the dispersion relation in generic form. Using this equation, it possible to study various special cases such as electrostatic condition ($\omega_k = 0$) and degeneracy of phonons ($m_k = 0, q_k = 0$).

4.6 Conclusion

In this chapter, a modeling approach for deformation of CNT sheet due to electron gas flow on its surface was proposed. The model incorporated a quantum-hydrodynamic formalism, Maxwellian electromagnetics, displacement, and thermodynamics of electron-phonon interaction, which resulted in eight partial differential equations. By applying Fourier transform from time domain to frequency domain, and by substituting them into the eight governing equations, dispersion relation is obtained. Results pertaining to the models developed in chapters 3 and 4 are presented in the next chapter.

Chapter 5

Results and Discussions

5.1 Introduction

This chapter is intended to demonstrate how the multiphysics model developed in chapters 3 and 4 can be employed to evaluate the field emission properties of CNTs in a thin film. The simulation results in this study have been obtained using MATLAB. Actual experiments have been performed in a vacuum chamber under a diode configuration to compare the theoretical results. The remainder of this chapter is organized as follows: experimental setup is explained in Section 5.2. Numerical simulations and experimental results for degradation of CNT thin films are presented in Section 5.3. Estimation of current-voltage characteristics and its comparison with experimental results is shown in Section 5.4. In Section 5.5, field emission current histories are presented, while results related to stress and temperature are described in Section 5.6. Sensitivity analysis of the parameters affecting the device current is illustrated in Section 5.7. Section 5.8 shows the influence of defects and impurities in CNTs on their field emission performance. Results related to design optimization studies are presented in Section 5.9. Field emission current history for applied AC voltage is described in Section 5.10. In Section 5.11, results of crosstalk phenomenon in a multi-pixel CNT array are explained. Section 5.12 consists of concluding remarks.

5.2 Experimental Setup

The MWNT films used for this study were realized by plasma-enhanced hot filament chemical vapor deposition (PECVD) at NanoLab Inc. Acetylene (C_2H_2) gas was used as the carbon source for the growth of CNTs and ammonia (NH_3) gas was used for both catalysis and dilution. Nickel (Ni) was used as a catalyst. In this process, the intensity of plasma was found to be critical in determining the aspect ratios of CNTs and their range of both site and height distributions within a given film. As the plasma intensity was increased, two structural changes were observed: (i) decrease in average tube diameters, and (ii) significant increase in tube lengths. The experimental details for the growth of the films have been described elsewhere [124], the only difference is the substrates. The influence of substrate materials on the field emission stability of CNT thin films has been investigated by us [125]. CNT films grown on a metallic (stainless steel) and a non-metallic (quartz) substrate were taken. The stability was analyzed by measuring the change in emission current over a period of time (5 hour in the present study) at a constant applied voltage. The applied voltages were selected such that the initial current was similar for the two films. The current fluctuation behavior was analyzed by fitting Gaussian function in the distribution of field emission current in 5 hour (see Fig. 5.1). The probability distribution can be represented by the half-peak width. The values of mean, standard deviation and half-peak width for the two films are summarized

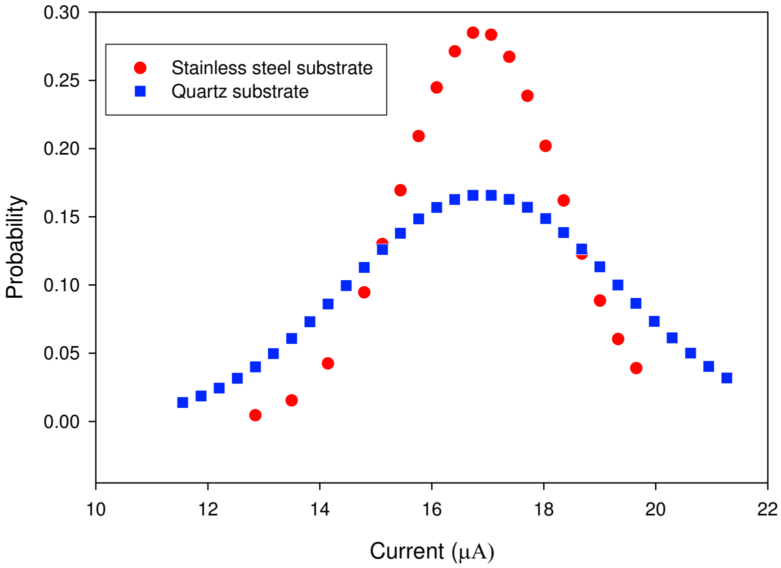

Figure 5.1: Probability distribution of emission current fitted with Gaussian function.

in Table 5.1. The preliminary results of this study reveal that the morphology of the film and emitting site density are more dominant than the substrate material. However, the interaction between CNTs and substrate material requires detailed investigation, which is an open area of research.

For detailed analysis, the film was grown on a copper-chromium (Cu-Cr) substrate. The area of the film was 1 cm^2. The density of the film amounted to 10^9 CNTs/cm^2. The field emission current was measured under a diode configuration. The measurements were carried out at a distance of approximately $150\mu m$ between the MWNT film cathode and the anode. The emission current values were recorded using a data acquisition (DAQ) card connected to a computer. The diode configuration was put inside a vacuum chamber mounted on an ion pump. The vacuum level was maintained at approximately 10^{-8} Torr to remove the gaseous molecules in the vacuum chamber. The schematic diagram of the experimental system is

Table 5.1: Constant current requirements for the four anodes.

Type of substrate	Mean	Standard deviation	Half-peak width
Stainless steel	16.867	1.395	3.285
Quartz	16.902	2.402	5.656

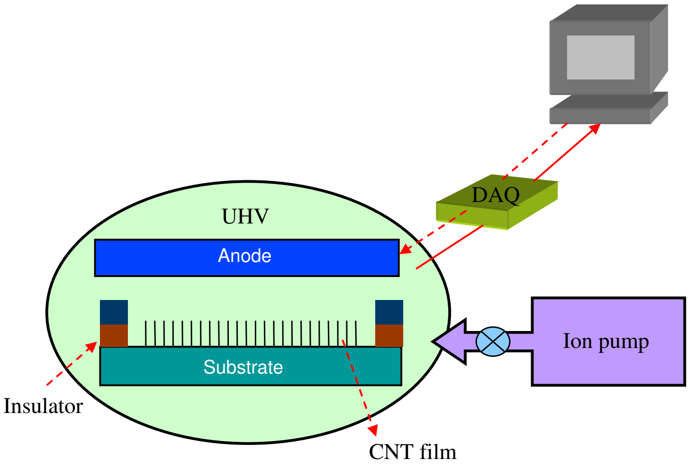

Figure 5.2: Schematic diagram of the experimental system.

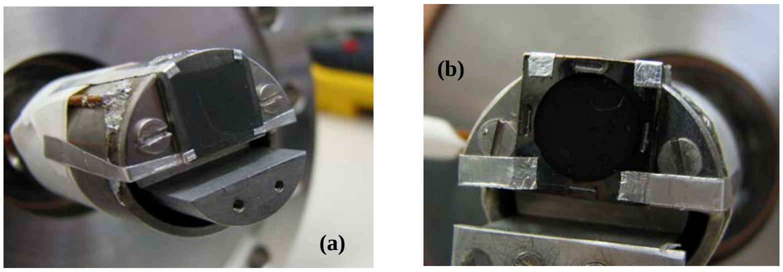

Figure 5.3: Close up showing the CNTs mounted on the holder.

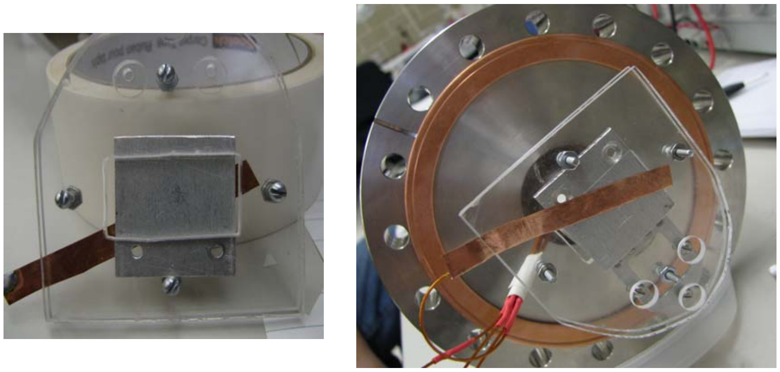

Figure 5.4: Front view of the gate holder (left) and circuit assembly before putting into the chamber.

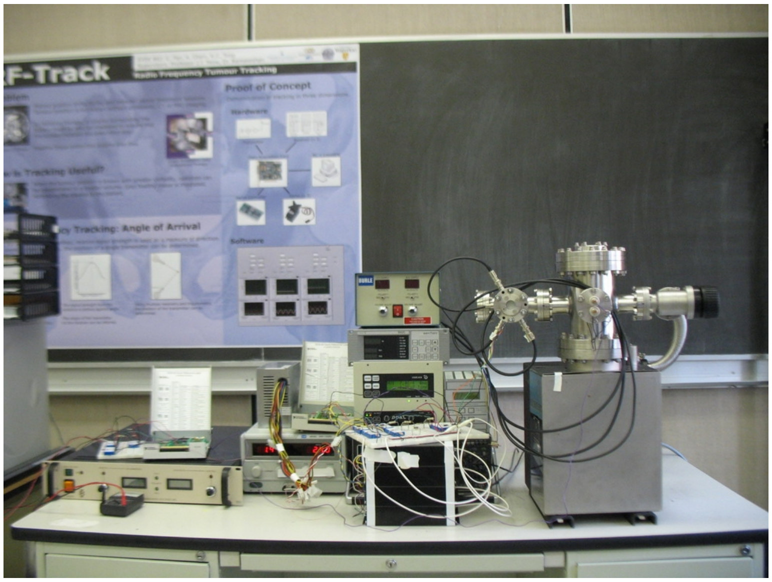

Figure 5.5: The complete experimental setup.

shown in Fig. 5.2. Some of the snapshots of the actual experimental setup are shown in Figs. 5.3-5.5. The details of the design of vacuum chamber is discussed in Appendix E [126].

5.3 Degradation of the CNT Thin Films

We have assumed that at $t = 0$, the diode contains minimal amount of carbon clusters. The CNTs degrade over time (due to both fragmentation and self-assembly) and the carbon cluster concentration in each cell also changes (mostly increases) accordingly. Based on this assumption, the initial conditions were set as $n_1(0) = 100$, $S(0) = 5000$, $M_1(0) = 2.12 \times 10^{-16}$, $A_n(0) = 0$, and $T = T_0 = 303K$. Figure 5.6 shows the $n_1(t)$ history over a small time interval of $160s$. Such evolution indicates that the carbon cluster concentration increases exponentially at the beginning and tends to a steady state afterward at $\approx 93s$, indicating a saturation. Therefore, Fig. 5.6 indicates the time that the degradation process takes to reach a saturation ($S(0) = 5000$) in the present analysis. Assuming that saturation has taken place within the computational cell, and assuming that this is the case for all the cells encompassing the entire volume between the cathode substrate and the anode, one can estimate $N_{\text{cluster}} = 5000 \times (0.04993)^2 \times 14 \times 10^{-6}$. Here, the film area is 49.93 mm^2 (as stated earlier) and the cathode to anode gap is assumed to be 14μm (a less conservative estimate since the free space above the CNT film is excluded). From Fig. 5.7, we obtain the effective area projected on anode for degradation process to be approximately 10^{-3} times the total film area. Multipying this factor to the number of clusters above, we estimate $N_{\text{cluster}} \approx 3.495 \times 10^{-10}$. The clusters assumed to be formed in this way are partly deposited on the cathode and partly pulled up ballistically and deposited on the anode. Results are discussed next.

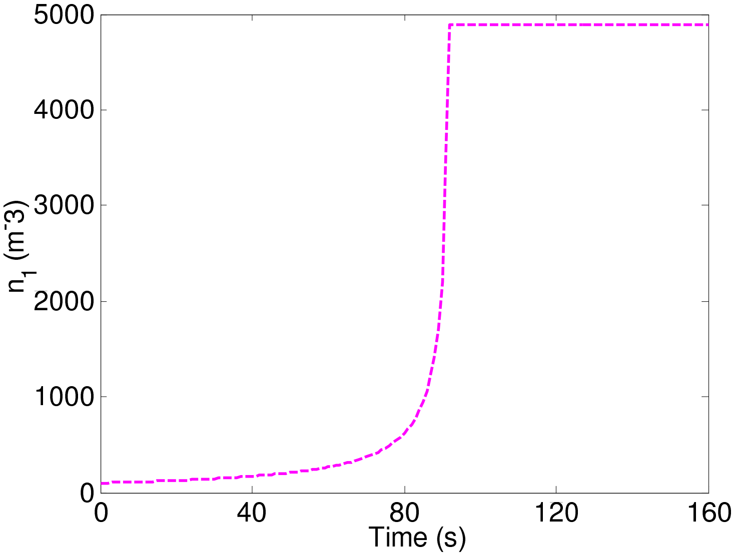

Figure 5.6: Variation of carbon cluster concentration over time. Initial condition: $S(0) = 5000$, $T = 303K$, $M_1(0) = 2.12 \times 10^{-16}$, $A_n(0) = 0$.

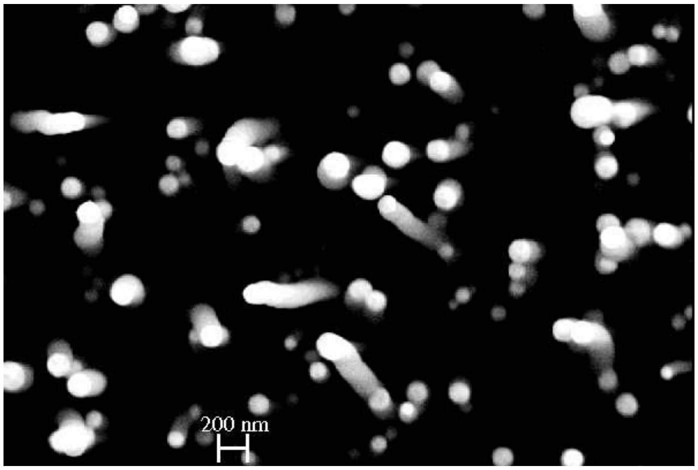

Figure 5.7: CNT tip distribution showing the area coverage under the anode. The shown area is approximately 5.08μm × 5.08μm.

Our experiments have revealed that degradation of CNTs into clusters is indeed one of the important processes that takes place during field emission. Interestingly, dark spots on the originally polished surface of the anode were found after 10 hour of field emission from a vertically aligned CNTs. The spots were visible by naked eye. Fig. 5.8 shows an optical image of these spots. The spot diameters were found to be in the range of 0.4mm to 0.7mm. The thin film substrate is made of Cu-Cr alloy. In order to find out if there is any degradation of CNTs with any trace of exposed metal substrate and any trace of carbon clusters on the anode, we perform energy-dispersive x-ray spectroscopy (EDS) on the film and on the anode surface.

The EDS results in Fig. 5.9 shown for one of the sample substrates after 10 hour of field emission indicates that the carbon clusters and the CNTs at various places were pulled up and the substrate was exposed. Along with nickel (Ni) impurities, which are present due to catalytic processing of CNTs, the spectral peaks of the Cr can be clearly seen in Fig. 5.9. On the other hand, traces of carbon cluster is observed on the anode surface (as shown in Fig. 5.8). EDS results reveal that the

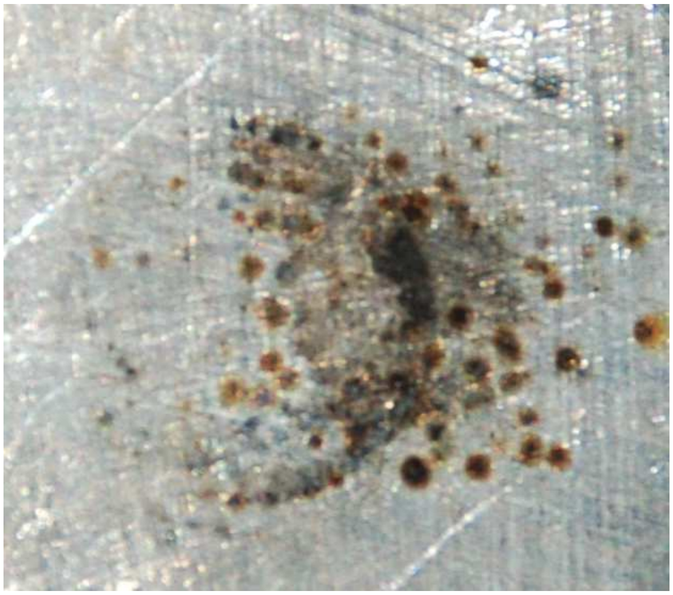

Figure 5.8: Dark spots on the anode after field emission showing the traces of clusters ejected from the CNT tips. Largest spot diameter ≈ 0.7 mm.

anode surface contains carbon as indicated by the spectral peaks in Fig. 5.10. We quantify the possible nature of degradation process as follows. With the area of the anode exposed to x-rays corresponding to $\approx 100\mu$m diameter spot containing 45.04 At% amorphous carbon, we get $N_{\text{cluster}} \approx 3.353 \times 10^{-9}$. Comparing this estimate with the previously simulated value of 3.495×10^{-10} from the degradation model, it is reasonable to assume that the reorientation of the CNT tips actually activate or deactivate the degradation process differently in different cells and at different times. As a result, one may observe a much slower degradation in the ensemble. However, at present, it is not possible to observe the occurance of the spots on the anode in a time-resolved manner.

The results analyzed above establish the fact that the degradation of CNTs is an important process. Influence of such degradation, along with the electro-mechanical

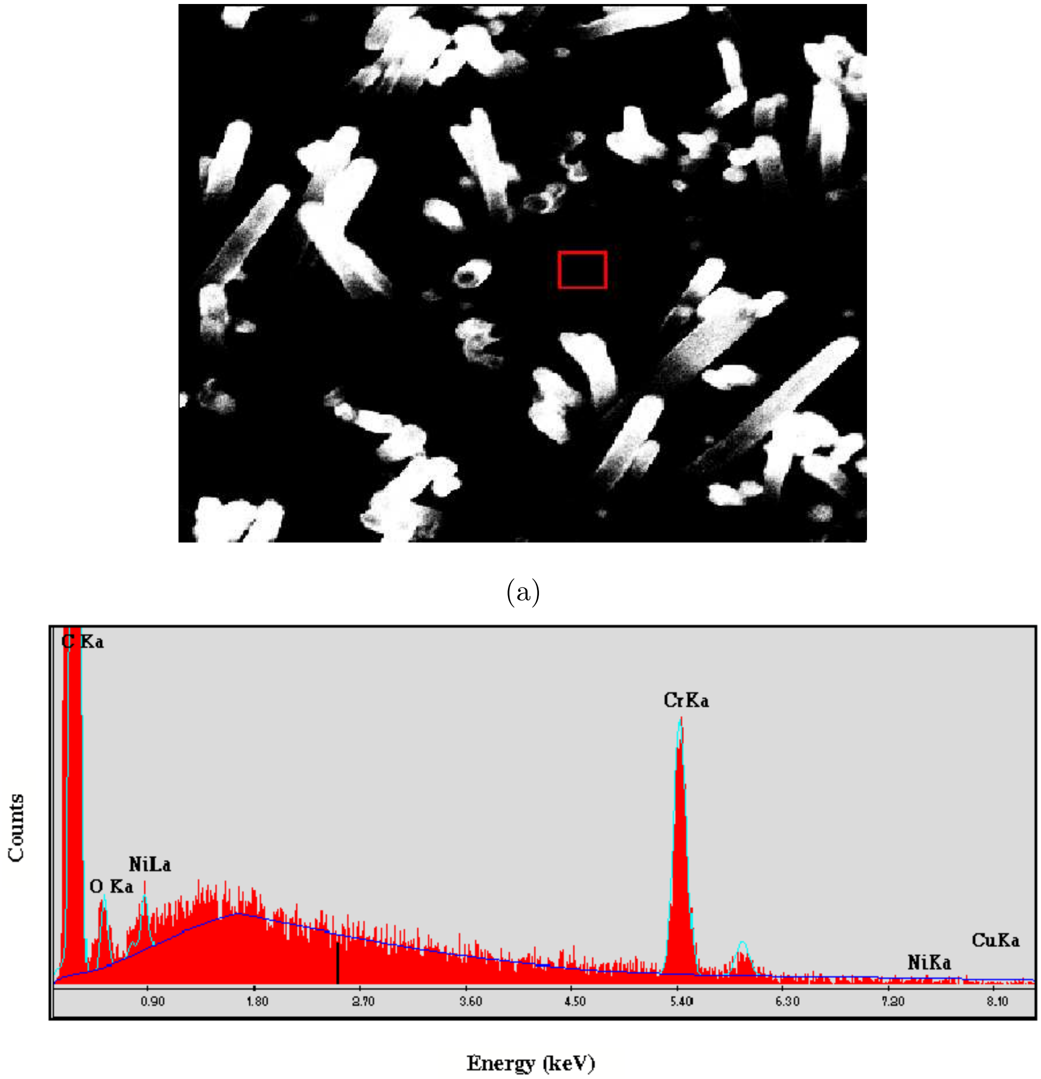

(a)

(b)

Figure 5.9: EDS results showing the exposed substrate surface made of Cr and Cu after the field emission. Energy spectrum shown in (b) corresponds to the region marked in (a).

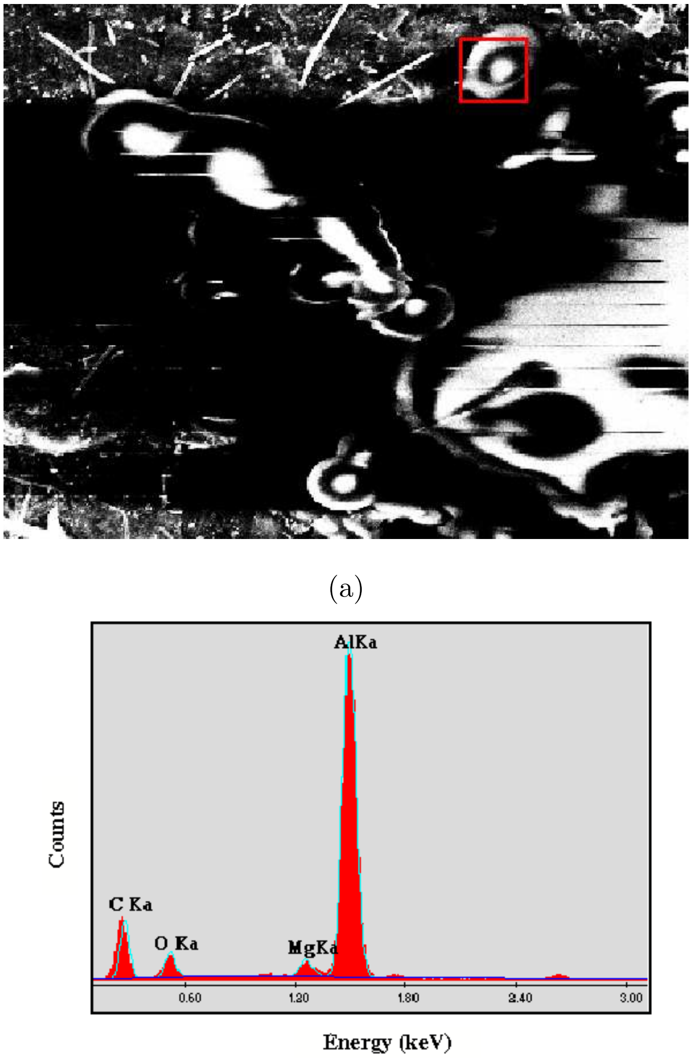
(a)

(b)

Figure 5.10: EDS results showing the deposited carbon clusters on the anode after field emission. Energy spectrum shown in (b) corresponds to the region marked in (a). Optical image of the spots are shown in Fig. 5.8.

Table 5.2: Trace of particles and their concentrations obtained from EDS measurements.

Emitter region	Element	Wt%	At%
Cathode	C K	87.20	96.25
	O K	0.84	0.70
	CrK	11.96	3.05
	NiK	0.00	0.00
	CuK	0.00	0.00
Anode	C K	32.47	45.84
	O K	29.11	30.86
	MgK	1.11	0.77
	AlK	31.14	19.57
	ClK	6.18	2.96

forces are expected to play significant role on the device current. However, a more detailed investigation on the physical mechanism of cluster formation and CNT fragmentation may be necessary, which is an open area of research.

5.4 Current-Voltage Characteristics

In the present study (as is common with most of the field emission studies), the FN equation has been used to calculate the current density. In such a semi-empirical calculation, the work function Φ [127] for the CNTs must be known accurately under a range of conditions for which the device-level simulations are being carried out. For CNTs, the field emission electrons originate from several excited energy

Table 5.3: Summary of work function values for CNTs.

Type of CNT	Φ (eV)	Method
SWNT	4.8	Ultraviolet photoelectron spectroscopy [130]
MWNT	4.3	Ultraviolet photoelectron spectroscopy [131]
MWNT	7.3±0.5	Field emission electronic energy distribution [132]
SWNT	5.05	Photoelectron emission [133]
MWNT	4.95	Photoelectron emission [133]
SWNT	1.1	Experiments [134]
MWNT	1.4	Experiments [134]
MWNT	0.2-1.0	Numerical approximation [135]

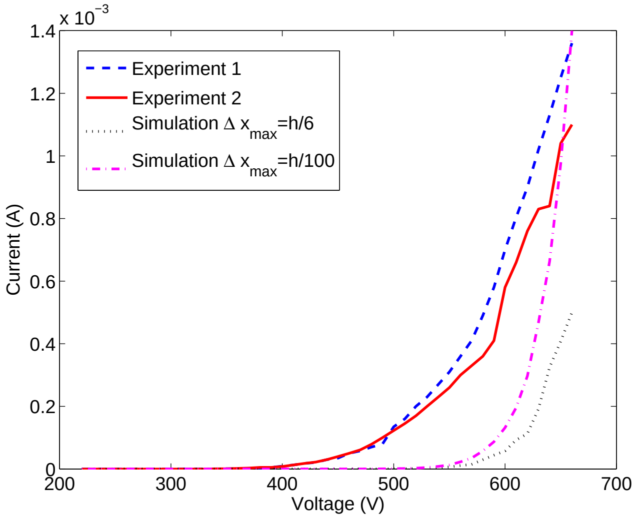

Figure 5.11: Comparision of simulated I-V curve with experiments without electron-phonon coupling and without heat transport at various tip deflections.

states (non metallic electronic states) [128]-[129]. Therefore, the work function for CNTs is usually not well identified and is more complicated to compute than for metals. Several methodologies for calculating the work function for CNTs have been proposed in literature. On the experimental side, ultraviolet photoelectron spectroscopy (UPS) was used by Suzuki *et al.* [130] to calculate the work function for SWNTs. They reported a work function value of 4.8 eV for SWNTs. By using UPS, Ago *et al.* [131] measured the work function for MWNTs as 4.3 eV. Fransen *et al.* [132] used the field emission electronic energy distribution (FEED) to investigate the work function for an individual MWNT that was mounted on a tungsten tip. From their experiments, the work function was found to be 7.3 ± 0.5 eV. Photoelectron emission (PEE) was used by Shiraishi *et al.* [133] to measure the work function for SWNTs and MWNTs. They measured the work function for SWNTs to be 5.05 eV and for MWNTs to be 4.95 eV. Experimental estimates of work function for CNTs were carried out also by Sinitsyn *et al.* [134]. They investigated two types of CNTs: (i) 0.8-1.1 nm diameter SWNTs twisted into ropes of 10 nm diameter, and (ii) 10 nm diameter MWNTs twisted into 30-100 nm diameter ropes. The work functions for SWNTs and MWNTs were estimated to be 1.1 eV and 1.4 eV, respectively. Obraztsov *et al.* [135] reported the work function for MWNTs grown by CVD to be in the range 0.2-1.0 eV. These work function values are much smaller than the work function values of metals ($\approx 3.6 - 5.4eV$), silicon($\approx 3.30 - 4.30eV$), and graphite($\approx 4.6 - 5.4eV$). The calculated values of work function of CNTs by different techniques is summarized in Table 5.3. The wide range of work functions in different studies indicates that there are possibly other important effects (such as electromechanical interactions and strain) which also depend on the method of sample preparation and different experimental techniques used in those studies. In the present study, a representative value $\Phi = 2.2eV$ was taken. The constants B

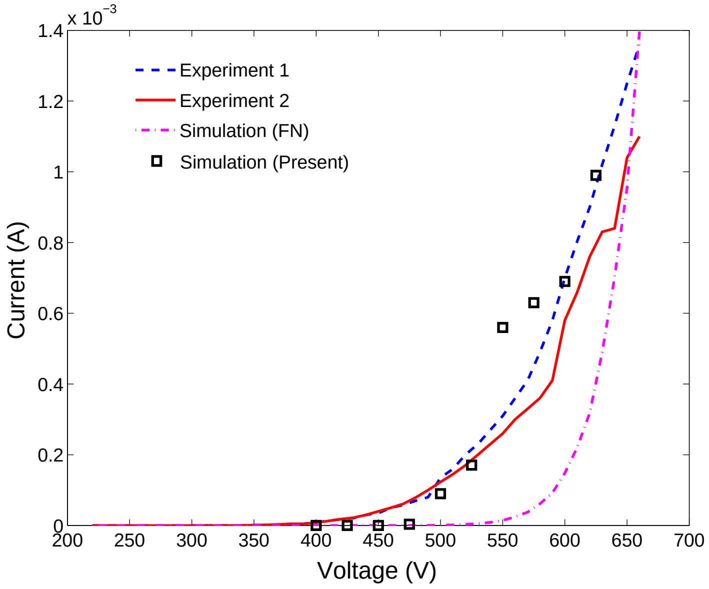

Figure 5.12: Comparision of simulated I-V curve with experiments with electron-phonon coupling and heat transport.

and C in Eq. (1.2) were taken as $(1.4 \times 10^{-6}) \times \exp((9.8929) \times \Phi^{-1/2})$ and 6.5×10^7, respectively [136].

The simulated current-voltage (I-V) characteristics of a film sample for a gap $d = 34.7\mu m$ is compared with the experimental measurement in Fig. 5.11 when the electron-phonon coupling and thermal transport is not considered. The average height, the average radius, and the average spacing between neighboring CNTs in the film sample are taken as $h_0 = 12\mu m$, $d_t = 3.92nm$, and $d_1 = 2\mu m$. The two simulated curves in the figure correspond to the cases where the bounds of the tip deflection are small in one case and large in the other case. The output current is low for the case with high average deflection, which is physically consistent. However, there is a deviation of the simulated current from the experimental curve in the voltage range of 400V to 600V. Next, we include these effects and present the

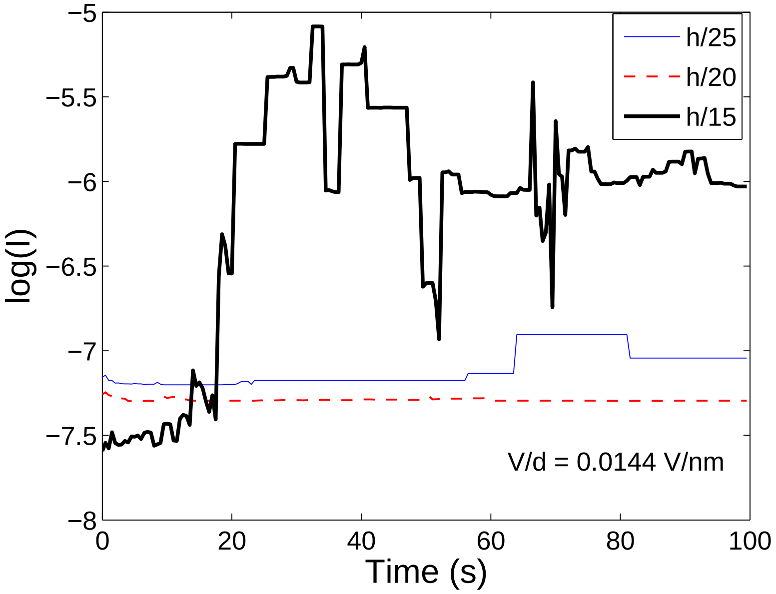

Figure 5.13: Field emission current histories for various initial average tip deflections h/m' and under bias voltage $V_0 = 500V$.

I-V results (see Fig. 5.12). The two simulation curves represent the cases with and without electron-phonon coupling and heat transport. It is clearly seen from this figure that the model is able to predict the current more accurately than the model involving only the reorientation of the CNTs and associated variation in the force field and without the effects of electron-phonon interaction and thermal transport. This is the first and preliminary simulation of its kind based on a multiphysics based modeling approach and the present model predicts the I-V characteristics.

5.5 Field Emission Current History

Here, we report experimental results of field emission current fluctuation and analyze such behavior based on the proposed model and by comparing the simulations

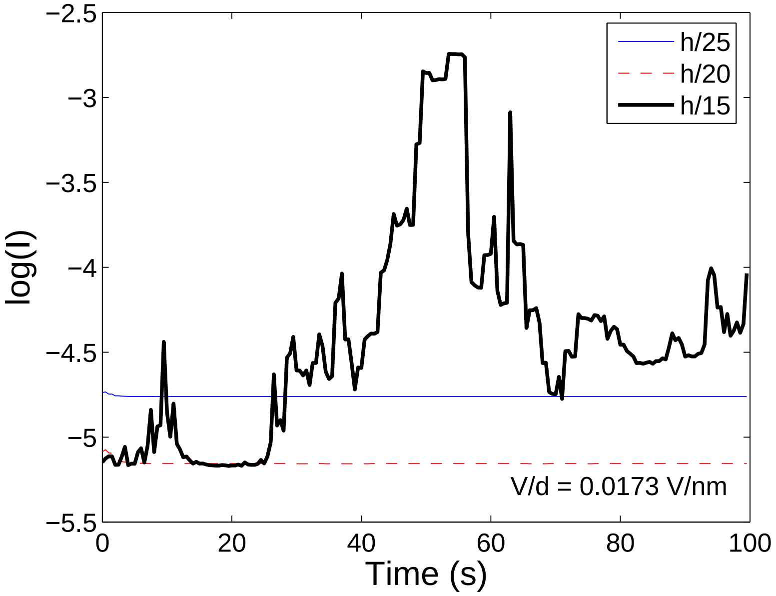

Figure 5.14: Field emission current histories for various initial average tip deflections h/m' and under bias voltage $V_0 = 600V$.

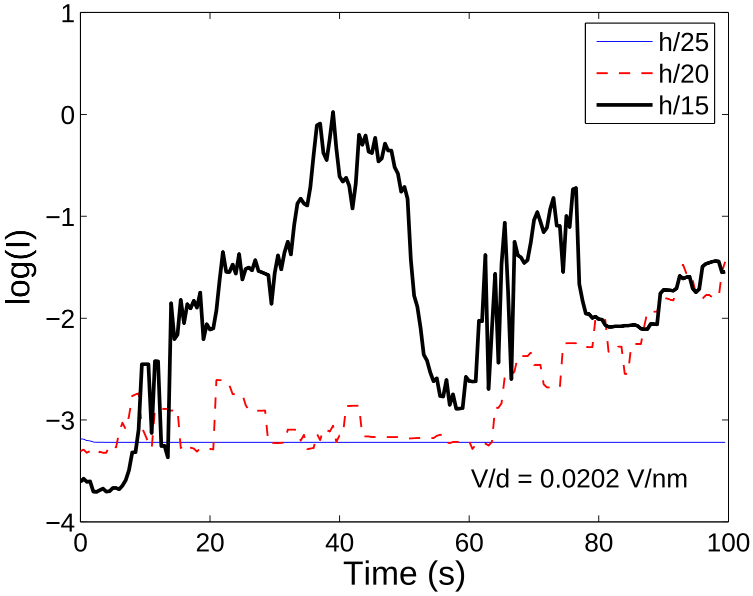

Figure 5.15: Field emission current histories for various initial average tip deflections h/m' and under bias voltage $V_0 = 700V$.

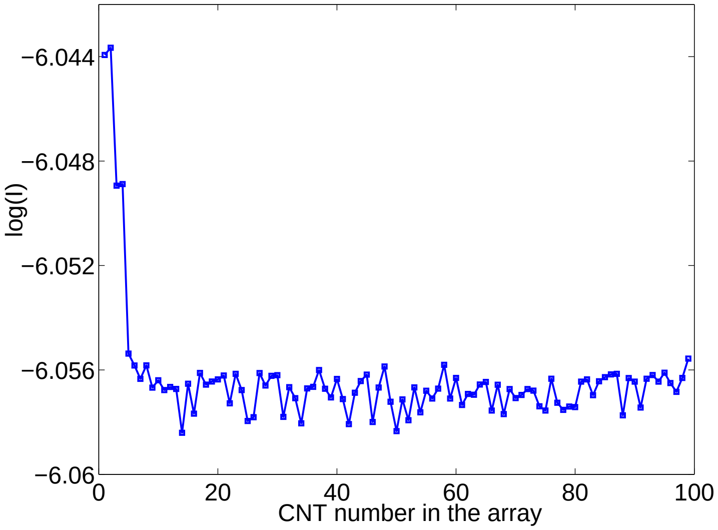

Figure 5.16: Current at the CNT tips during 100 s of field emission.

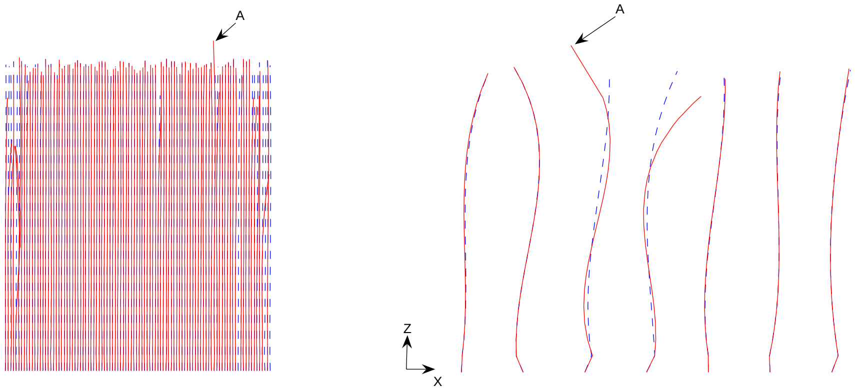

(a) (b)

Figure 5.17: (a) Array of 100 CNTs (non-uniform height distribution with maximum initial tip deflections of $h/20$) (b) enlarged view of the region near the pulled up CNT (marked as 'A' and deflected horizontally $\approx 2\mu$m). The Initial shape is shown by dashed line and the deflected shapes at $t = 100s$ are shown in solid line.

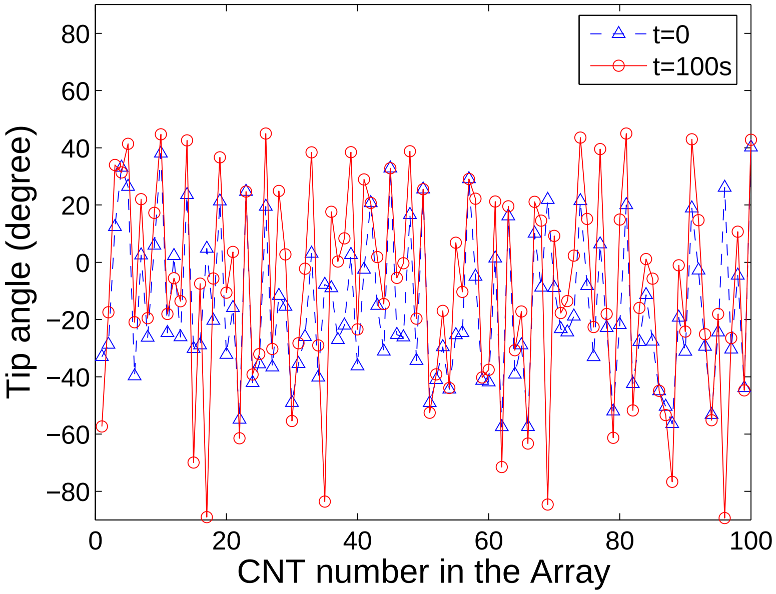

Figure 5.18: Comparison of tip orientation angles $\theta(t)$ at $t = 0$ and $t = 100$ s.

with the experimental data. Figures 5.13-5.15 show the simulated effects of the largely deflected CNT tips in the film (higher h/m' values) and the effects of increasing bias voltages on the field emission current histories. Figure 5.16 shows the tip current distribution at $t = 100s$ for an array of 100 CNTs [137]. By comparing the curves in these figures, the following two important observations can be drawn: (i) for a constant bias voltage, as the initial average deflections/angle of the CNTs are increased from $h/25$ to $h/20$, the average current reduces. With further increase in the initial state of deflection/angle (e.g., $h/15$), the electrodynamic interaction among CNTs and the mechanical deformation produces sudden stretching of the deflected tips towards the anode (see the CNT tip marked as 'A' in Fig. 5.17 and deflected horizontally $\approx 2\mu$m); (ii) the trends in the current fluctuation for higher h/m' in Fig. 5.15 (for high bias) indicate current spikes with an amplitude factor of $\approx 10^3$, whereas in Fig. 5.13 and 5.14 (for low bias voltage) the trend indicates cur-

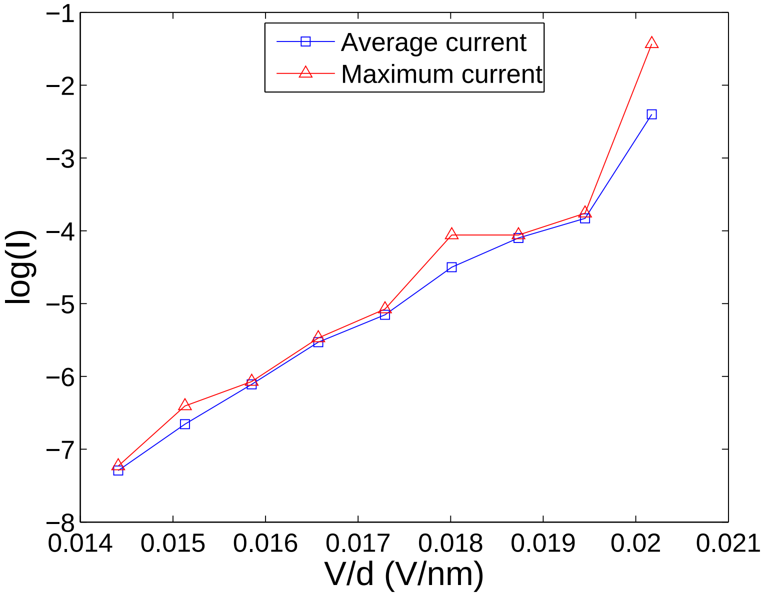

Figure 5.19: Variation in the maximum current and the average current due to field emission under increasing bias electric field.

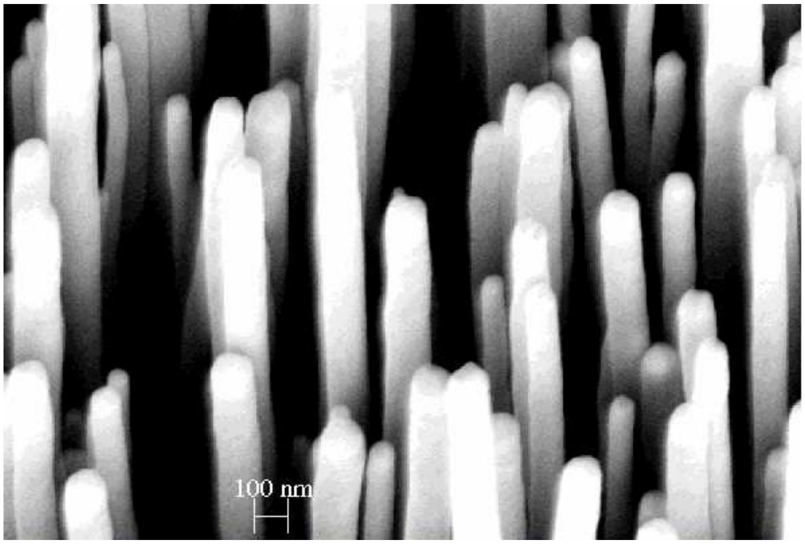

Figure 5.20: Vertically aligned CNTs before field emission.

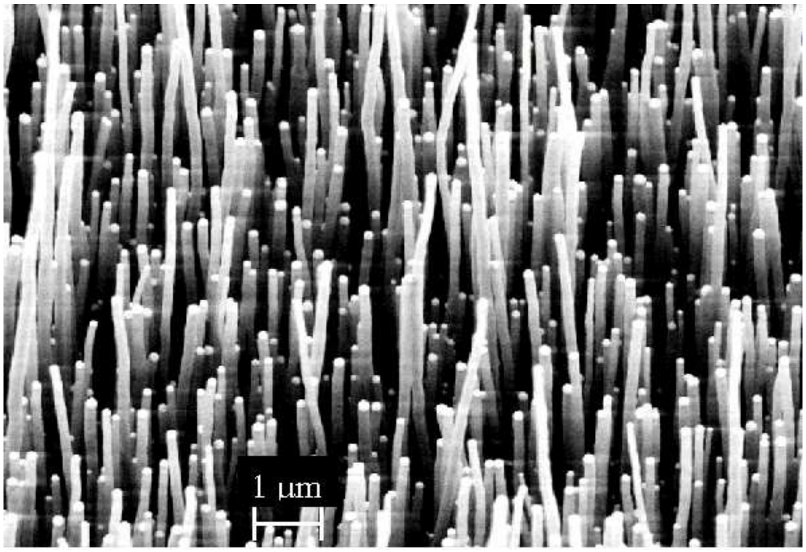

Figure 5.21: Small reorientations and electrodynamic force induced stretching of CNTs before long duration exposure.

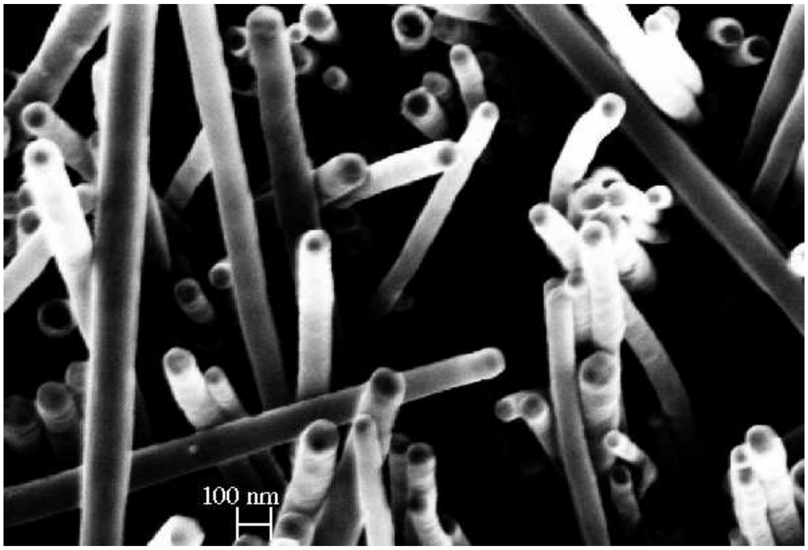

Figure 5.22: Reoriented CNTs after 10 hr of field emission.

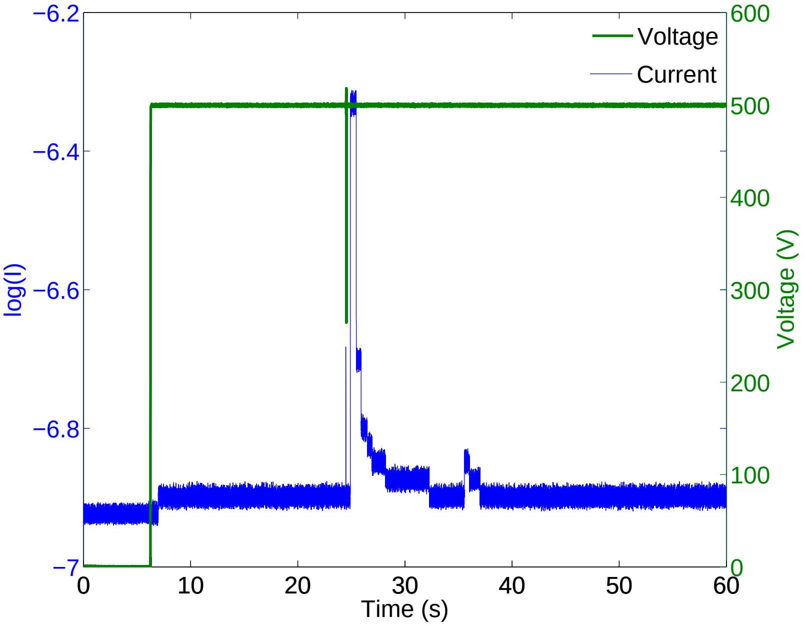

Figure 5.23: Spikes in the field emission current at low bias voltage due to reorientation and pull-up of few CNTs.

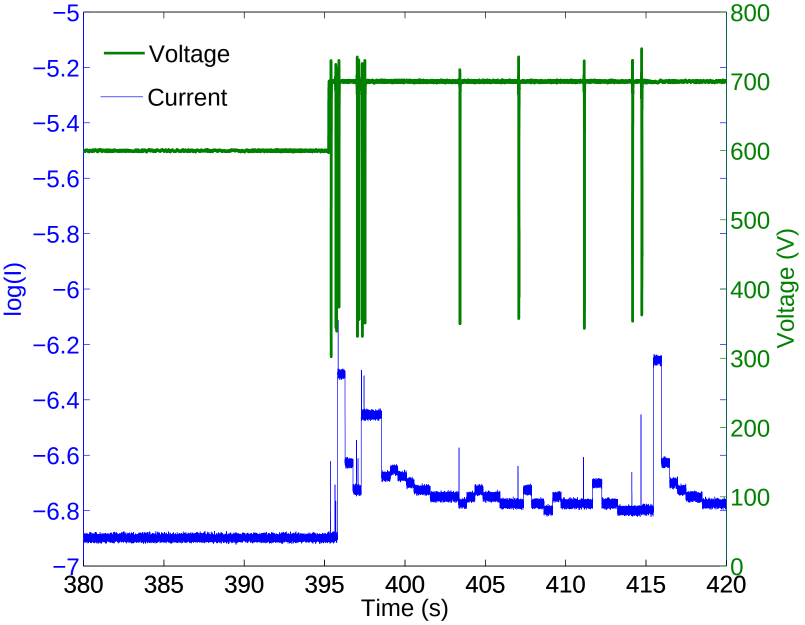

Figure 5.24: Fluctuation of field emission current from a baked sample having vertically aligned CNTs.

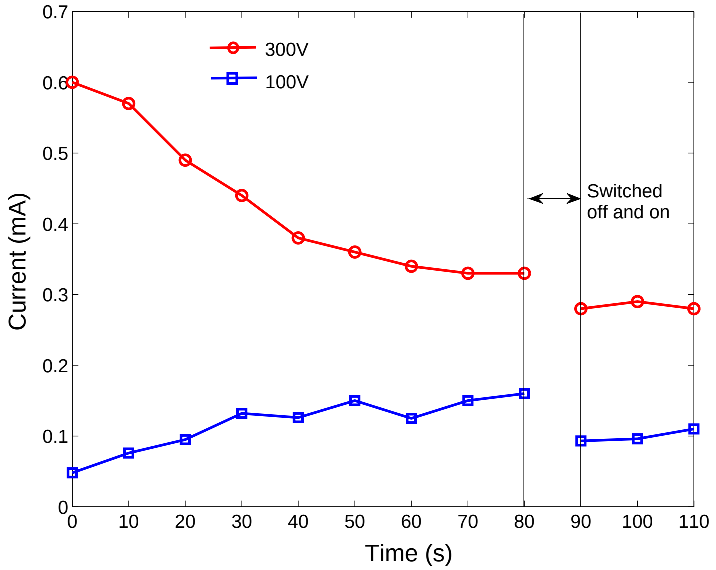

Figure 5.25: Effect of low bias voltage switching on/off indicating negligible effect of electrodynamic transients on the field emission at low voltage.

rent spikes with an amplitude factor of $\approx 10^2$. The current spikes are the results of electrodynamic stretching, causing reorientation of the CNTs. Figure 5.18 shows a comparison of the distribution of the tip angle θ over an array of 100 CNTs at $t = 0$ with $h/20$ and $t = 100s$ under bias voltage $V_0 = 700V$ (0.0202 V/nm). Figure 5.18 reveals that after experiencing the electrodynamic stretching, some of the CNTs with angle $+\theta$ may reorient to $-\theta$, whereas some of the already largely deflected CNTs move further away with increasing $|\theta|$ due to Coulombic repulsion. The above results also justify several experimental observations, which have been reported in literature from a comparative perspective of using single CNT and then different types of CNTs in thin films and the effect of their alignments [12], [16], [85]. For example, Collins and Zettl [16] attribute change in currents to interactions between neighboring CNTs. Based on the statistical analysis of the simulated data, we plot the maximum current and the average current in Fig. 5.19 for various bias voltages. A linear $log(I)$ vs. V/d behaviour can be observed in Fig. 5.19. However, at higher bias voltages, the maximum current tends to differ from the average current.

In the field emission experiments, we have exposed several experimental CNT samples. Fig. 5.20 shows the SEM image of one such sample having vertically aligned CNTs. In Fig. 5.21, the SEM image of the sample after a short period of exposure is shown. Fig. 5.22 shows the SEM of the same sample as in Fig. 5.20 but after 10 hour of field emission. Figures 5.23 and 5.24 represent the current history as observed experimentally. These experimental results confirm a strong electromechanical interaction among the CNTs along with certain amount of degradations. Occasional shorting of the electrical circuit were observed for smaller gaps between the electrodes. Such short circuit condition is the result of pull up of one or more CNTs under the increased electrodynamic force. Figure 5.24 shows more number of spikes as the bias voltage is increased to 700V. The current history due to switching on/off for low bias voltages for a duration of 10 seconds are shown in Fig. 5.25. It is clear from this figure that at very low bias voltages, the electrodynamic transient force field on the emission current is negligible. Also, the pattern of current saturation over time changes from $(1 - e^{\alpha t})$ like shape to $e^{-\alpha t}$ like shape as the bias voltage is increased from 100V to 300V.

Fig. 5.22 is more interesting in comparison to Figs. 5.21 and 5.20. While Fig. 5.21 depicts small reorientations and electromechanical force induced stretching of CNTs for a short-term exposure, Fig. 5.22 clearly shows a combined effect of reorientations and degradation of few CNTs (pulling up and exposing substrate as discussed earlier) after 10 hour of field emission. With these experimental results, the proposed modeling framework and the simulated results regarding CNT tip deflections in Fig. 5.17 proves to be an important insight towards understanding

Table 5.4: Maximum tensile stress σ_{zz} (GPa) due to electro-mechanical pull-up of CNTs for various initial tip deflections and background electric field V_0/d.

Initial tip deflection	0.0144 V/nm	0.0173 V/nm	0.0202 V/nm
h/25	0.309	0.024	0.403
h/20	0.091	0.975	1.056
h/15	1.223	1.173	1.095

the nature of field emission response. The results in Fig. 5.17 are also in agreement with previous reported study [138].

5.6 Stress and Temperature

As seen in Figs. 5.13-5.15, since the current spikes can cause high stress and growth of defects in CNT, we further analyze the stress accumulated in the CNTs based on Eq. (3.47). It may be noted that the bias electric field (V/d) used in the numerical simulation is much smaller than those used in the reported literature regarding degradation and breakdown of a single CNT [93, 136]. Usually, $V/d > 1$ V/nm is considered to be high enough to produce defects in the CNTs. Based on the simulation, the maximum tensile stress attained during 100 s of field emission corresponding to Fig. 5.13-5.15 is given in Table 5.4. Data in this table indicate non-monotonic increase in the stress for increasing h/m'. The highest stress is observed for $h/15$ under low bias field of 0.0144 V/nm. For higher bias field, the stress increases monotonically for increasing h/m'. Corresponding changes in the

Table 5.5: Strained bandgaps (eV) corresponding to the maximum stress values in Table 5.4 for various initial tip deflections and background electric field V_0/d.

Initial tip deflection	0.0144 V/nm	0.0173 V/nm	0.0202 V/nm
h/25	4.921	4.925	4.920
h/20	4.924	4.912	4.910
h/15	4.908	4.909	4.910

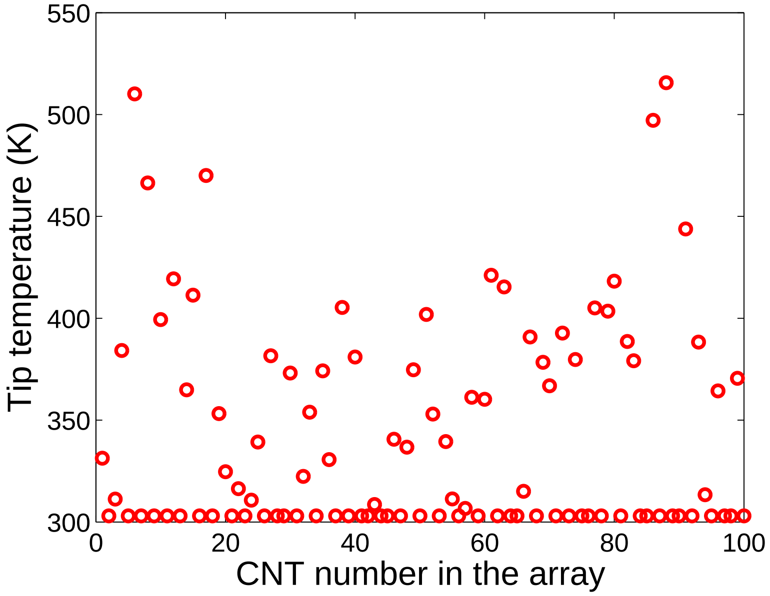

Figure 5.26: Maximum temperature of the CNT tips during 100 s of field emission.

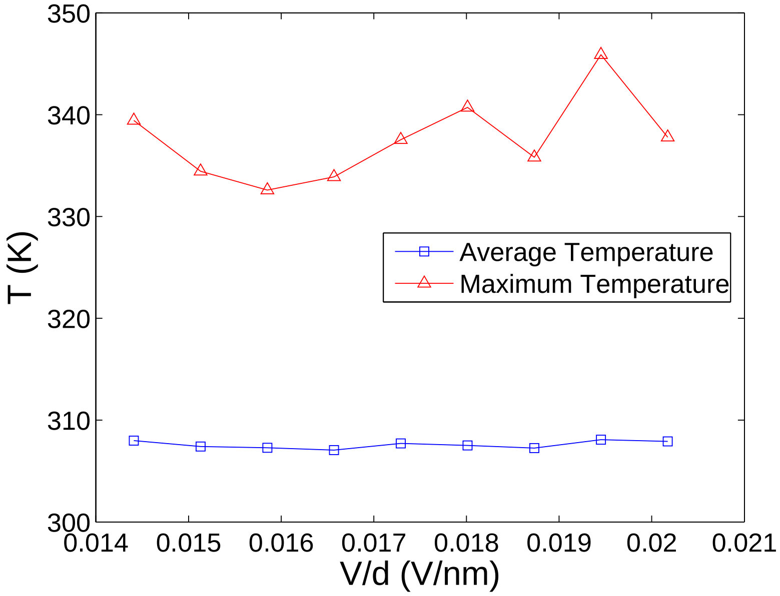

Figure 5.27: Variation in the maximum and average temperature due to field emission under increasing bias electric field.

bandgap is calculated by assuming the Young's modulus value of 0.27 TPa and tightbinding formulation for bandstructure as function of small strain [139]. The strained bandgap values are tabulated in Table 5.5. Unstrained bandgap is estimated as 4.926 eV. Table 5.5 indicates a maximum deviation of ≈ 15 meV in the bandgaps among various conditions of bias voltage and maximum stresses.

The maximum stress in all the cases is found to be 1.223 GPa, which is much smaller than the fracture stress [67] (> 65 GPa). Therefore, it is less likely in the present case that the CNTs in the film could fail by fracture under the chosen initial film pattern and bias field. This is confirmed from Fig. 5.23. However, electric breakdown process is possibly accelerated as the current spikes also give rise to temperature spikes. At a breakdown temperature T_c (generally > 900 K), one may expect degradation of CNTs, and hence a proportional decrease in the electron density at a rate $\tilde{n}\omega_c \exp(-\Delta_c/(kT_c))$, where ω_c is the highest frequency in the spectrum of the temperature spike and $\Delta_c \approx 3-4$ eV (see ref. [119]). In Fig. 5.26, we plot the maximum tip temperature distribution over an array of 100 CNTs during field emission at a bias voltage of 700 V over 100 s duration (corresponding to the tip angle distribution shown in Fig. 5.18). This result indicates a temperature rise up to ≈ 520 K for a bias field of 0.0202 V/nm. This temperature rise was observed at $t = 40$ s. Based on the statistical analysis of the simulated data, we plot the maximum temperature and the average temperature for various bias voltages are plotted in Fig. 5.27. From Fig. 5.27, it can be seen that the average temperature is almost independent of the bias voltage, whereas the maximum temperature fluctuates by more than 10 K over the range of bias field.

5.7 Sensitivity Analysis of Parameters Affecting Device Current

As described earlier in this thesis, field emission requires UHV environment. However, as observed by Lim *et al.* [96], presence of different gases have different effects when CNTs are used as cathodes. For example, CNTs have been found to be highly sensitive to the presence of oxygen, which results in oxidative etching and failure of CNTs. CNTs are also susceptible to damage by the presence of nitrogen. The presence of hydrogen during field emission enhances the output current but marginally. However, the presence of water vapor considerably enhances the field emission properties of CNTs. In addition, the simulation results in this thesis reveal that following parameters have significant effect on field emission current.

(i) CNT geometry: This study found that change in height, diameter and spacing between neighboring CNTs affects the field emission current. This is to due change in distance between CNT tips and anode, sharpening of tips and change in screening effect. However, the influence of variation in height on field emission current was found to be most dominant;

(ii) Chirality: During simulations in this thesis, different values of the integer pair (n, m) were used. The simulation results reveal that the use of arm chair CNTs appreciably increases the device current;

(iii) Orientation: As evident from simulation plots related to current-voltage and current-time, the output current decreases when the state of deflection of CNTs is more. These results are physically consisten because the distance between the tips of CNTs and the anode increases;

(iv) Electromechanical forces: The simulation studies reveal that in high voltage regime, ponderomotive and electrostatic forces become dominant, resulting in reorientation and more fluctuations in device current. van der Waals forces have been found to be very weak when the applied voltage is high;

(v) Temperature, surface electron density and electric field: Initially, in this study, thermodynamics of electron-phonon interaction, fluctation in surface electron density and electric field were not taken into consideration [99]. As a result, a shift in simulated I-V characteristics from experiments was observed. In addition, the simulated results were not able to capture apikes in the current history. Incorporation of these parameters and the results there in are in close agreement to experimental studies. This proves that the device current is highly sensitive to variation in these parameters.

5.8 Influence of Defects and Impurities

In the context of field emission from CNT tips, a simple estimate of defects has been proposed by introducing a correction factor in the FN equation. However, it is clear that a more detailed physics based treatment is required for a better understanding of processes at the device-scale level. The novelty of our present approach is twofold. Firstly, we employ a concept of effective stiffness degradation for segments of CNTs, which is due to structural defects, by modifying the chiral vector in Eq. (3.22). The effective stiffness degradation is modeled by introducing an effective chiral vector $\alpha\vec{C}_h$, where $0 < \alpha < 1$ describes the extent of structural defects over the tube circumference at a particular cross-section of a CNT in the array. Secondly, we incorporate the vacancy defects and charge impurity effects in our Green's function based approach. This is done by computing the effective

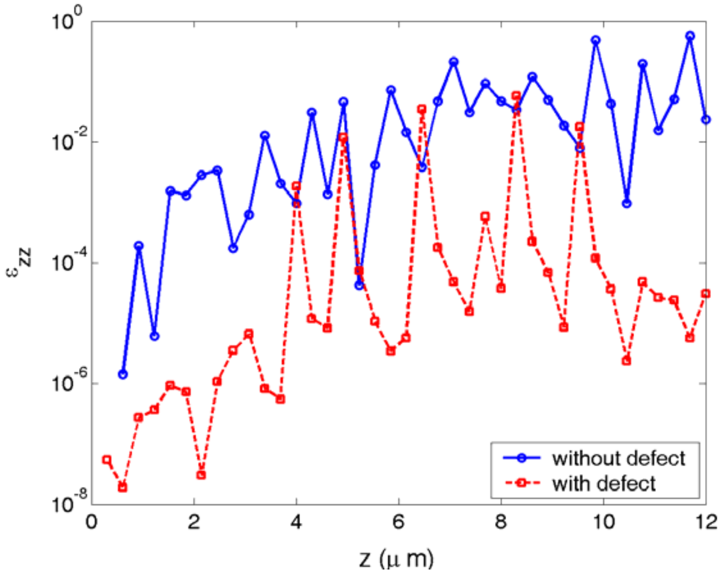

Figure 5.28: Cross-sectional average longitudinal strain distribution along the CNT at t=0.1s.

electric potential energy as [140],

$$\mathcal{V}(x,z) = -eV_s - e(V_d - V_s)\frac{z}{d} + \sum_j G(i,j)(\tilde{n}_j - n \pm \overline{m}_l + \delta_{kj}) \ , \tag{5.1}$$

where $\overline{m}_l$ denotes the charge due to impurity at coordinate l, and δ_{kj} denotes the vacancy at atom position k.

An array of 10 vertically aligned and each 12 μm long CNTs is considered for the device scale analysis. Defect regions are introduced randomly over the CNT length with $\alpha = 0.2$ and positive charge density of $\overline{m}_l = 10$. Figure 5.28 shows the decrease in the longitudinal strain due to defects. Contrary to the expected influence of purely mechanical degradation, this result indicates that the charge impurity, and hence weaker transport, can lead to a different electromechanical force field, which ultimately can reduce the strain. However, there could be significant fluctuations in such strain field due to electron-phonon coupling. The effect of such

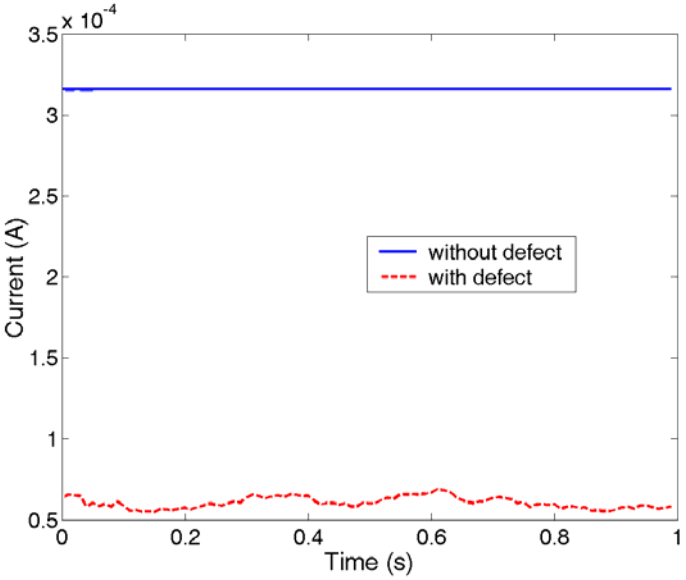

Figure 5.29: Field emission current history for gate voltage of 600V from an array of 10 CNTs with and without defects.

fluctuations (with defects) can be seen in Fig. 5.29 where we provide the plot of the field emission current history. The average current also decreases significantly due to such defects.

5.9 Design Optimization Results

In the proposed design, we introduce two additional gates on the edges of the cathode substrate. The height of CNTs in arrays was varied between 6 μm to 12 μm. The height of the CNTs is such that a symmetric force field is maintained in each pixel with respect to the central axis parallel to z-axis (see Fig. 5.30) [141]. As a result, it is expected that a maximum current density and well-shaped beam can be produced under DC voltage across the cathode-anode structure. In the present

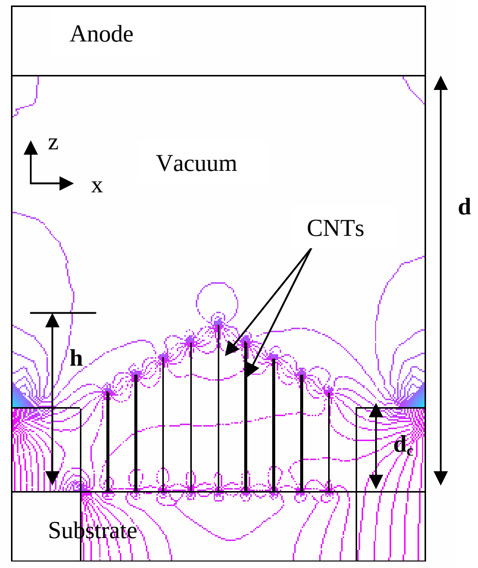

Figure 5.30: Contour plots of electric field showing the concentration near the CNT tips.

design, the anode is assumed to be simply a uniform conducting slab. However, such an anode can be replaced with a porous thin film along with MEMS-based beam control mechanism. Figure 5.30 shows the transverse electric field distribution in the pixel, which directly influences the field emission current.

We simulate the field emission current histories for two different parametric variations: diameter and spacing between CNTs at the cathode substrate. The current histories are simulated for a constant bias voltage of 650V. In the first case, the spacing between neighboring CNTs is kept constant, while the diameter is varied. The current histories for different values of diameters are shown in Fig. 5.31. As evident from the figure, the output current is low at large diameter values. This is due to the fact that current amplification is less with large diameter of CNTs. In the second case, the diameter is kept constant, while the spacing between

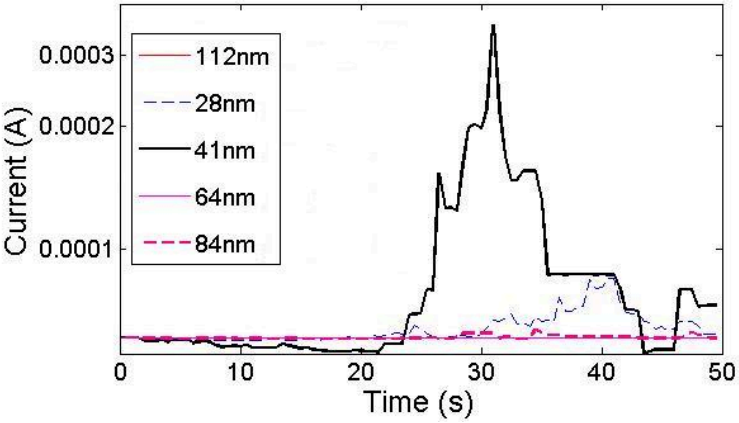

Figure 5.31: Simulated field emission current histories for varying diameters of CNTs under a DC voltage of 650V.

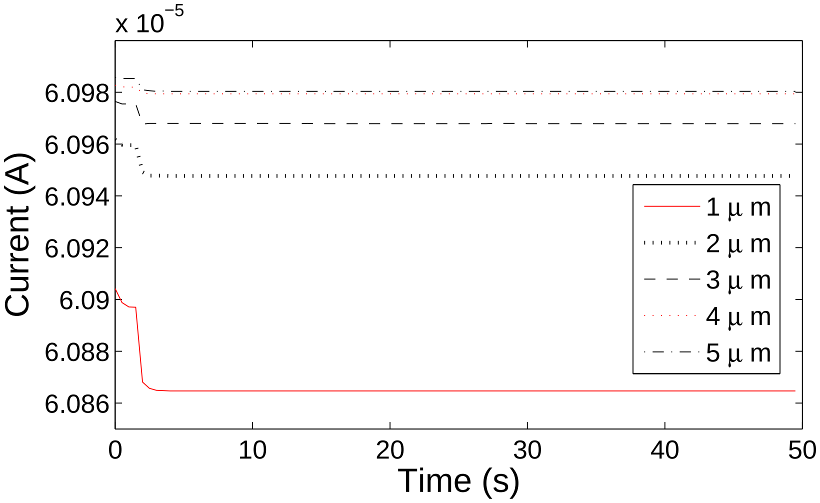

Figure 5.32: Simulated field emission current histories for varying spacing between neighboring CNTs under a DC voltage of 650V.

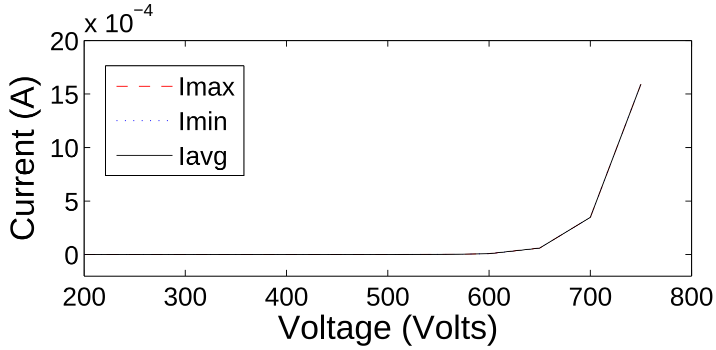

Figure 5.33: Simulated current-voltage characteristics.

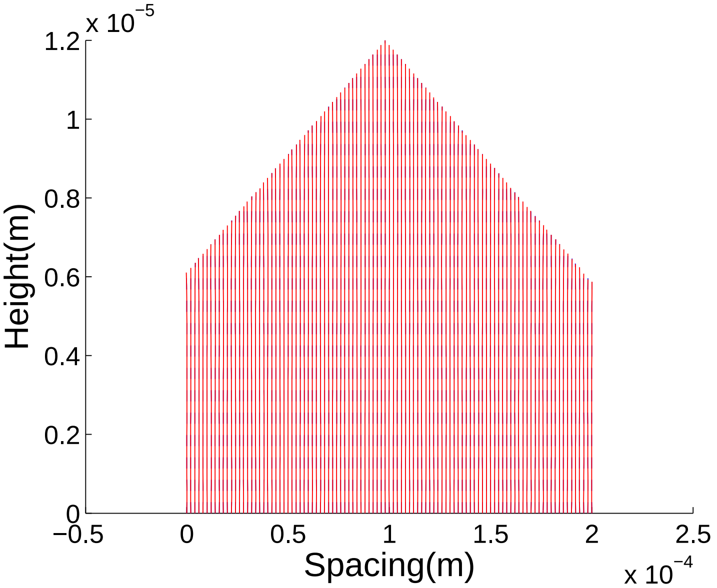

Figure 5.34: Initial and deflected shape of an array of 100 CNTs at t=50s of field emission.

neighboring CNTs is varied. Following five values of spacing between neighboring CNTs have been considered: 1 μm, 2 μm, 3 μm, 4 μm and 5 μm. The current histories for all these cases are shown in Fig. 5.32. The trends in five curves in Fig. 5.32 tell us the following: (i) the current in all cases decreases initially and then becomes constant afterwards. This may be due to realignment of CNTs in the array when voltage is applied; (ii) as the spacing between neighboring CNTs increases, the output current increases, which is physically consistent because the screening effect becomes less pronounced. These results are in agreement with a previously reported study [19].

Next, we simulate the current-voltage (I-V) characteristics for this arrangement. The minimum, average, and maximum values of current were computed. The simulated results are shown in Fig. 5.33. These results give some interesting insights. For example, as evident from Fig. 5.33, the linear height distribution has stabilized the I-V response drastically as compared to uniform height reported in the previous studies. The variation in I-V characteristics for the three cases in this new design is negligible. This is further confirmed by analyzing the simulated results of CNT tip deflections in Fig. 5.34, in which there is no significant deflection of CNT tips after 50 seconds.

5.10 Field Emission Current History for Applied AC Voltage

In the theoretical model of the electron-phonon interaction, we have eight partial differential equations, as discussed in Chapter 4. The variables here are T, $\tilde{n}_1$, $u_{z'}^{(2)}$, $u_r^{(2)}$, $u_{\theta 0}^{(2)}$, $E_{z'}$, E_r, and $E_{\theta 0}$. By applying Fourier transform from time domain to fre-

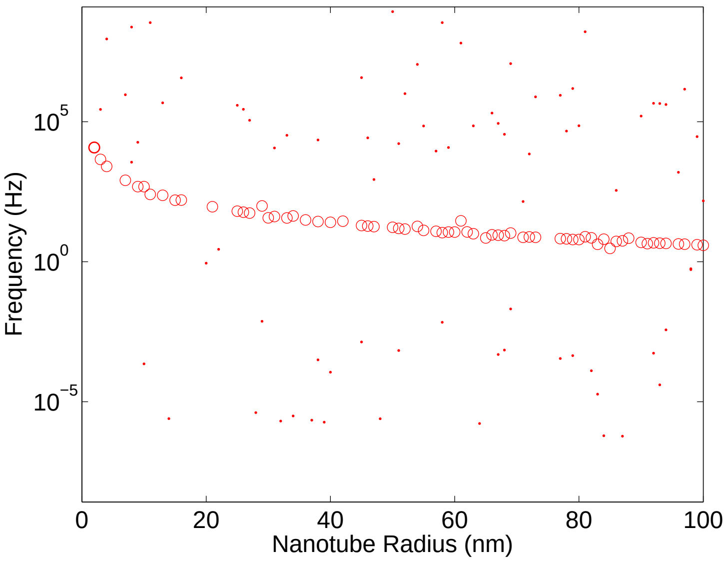

Figure 5.35: Frequencies for zero longitudinal wavenumber and zero radial wavenumber and for various values of the CNT radius.

quency domain and assuming periodic field distribution in terms of the wavevectors, and by substituing them into the eight governing equations, we get the dispersion relation. Fig. 5.35 shows the frequencies for various values of the CNT radius. The circles show the frequencies (ω_k) at which there will be uniform flow of conduction electrons (i.e., for the zero waveneumebrs: $q_k = 0$, $m_k = 0$). In Fig. 5.35, the dots indicate the various values of the frequencies at the which the acoustic phonons and the thermal phonons cease to exist; that is, at these frequencies the coupled phonon modes are degenerate and the resulting effect is the same as in an ideal cylindrical CNT with no fluctuation in the CNT sheet.

In this study, we report the first set of experimental results, wherein the field emission current has been measured for various AC frequencies at 600V of bias DC voltage across the CNT substrate and the anode. Figure 5.36 shows the field

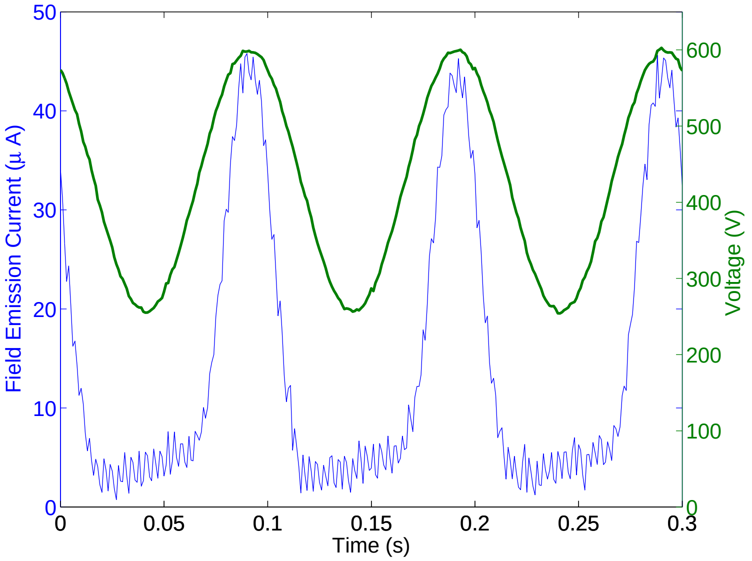

Figure 5.36: Field emission current history for applied AC voltage at 600V and 10 Hz. Voltage history is shown by thick solid line.

emission current history (thin lines) and the applied AC voltage history (solid line) at frequency of 10Hz. The field emission current is obtained for a steady-state oscillation of voltage with amplitude of 600V. A drop in the resistivity can be seen at the peak voltage, whereas at the minimum voltage, the field current is fluctuation dominated. Figure 5.37 shows the variation in the maximum field emission current obtained for 600V DC voltage as we vary the frequencies. From Fig. 5.37, it is seen that the field emission current drops by approximately 10 μA as the applied voltage is changed from 600V DC to 600V AC at 2Hz. However, an amplification of field emission current at about 40Hz (voltage is kept at 600V) can be seen. Although a very low frequency as compared to the ballistic transport regime is applied (see the frequency range in Fig. 5.35), the frequency variation seen in Fig. 5.37 is essentially an indication that phonon-assisted control of field emission current in CNT film

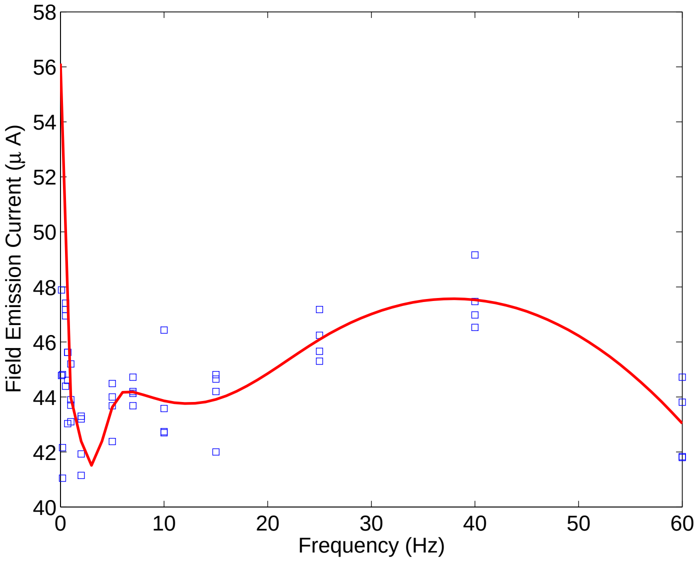

Figure 5.37: Variation in the field emission current amplitude for various frequencies of applied AC voltage. Applied AC voltage amplitude is 600V for all frequencies.

device is possible [121].

Hysteresis in CNTs is not new but it has been observed while investigating the mechanical properties [72]. While performing the experiments, hysteresis in field emission was observed as the frequency was increased. The experimental results are shown in Fig. 5.38. Since the data has been acquired at fast speed, therefore, transient responses are building up as damping is low in the system. After some time, there is transience built in the system to throw the response off the steady-state. As we approach resonance frequency from below, the response becomes larger and multi-valued, which proves the presence of nonlinearity and indicates hardening nonlinearity. Some preliminary studies on this aspect has been conducted [142]. However, this remarkable property should be characterized in detail in order to exploit these results for device applications. This includes: (i) determination of

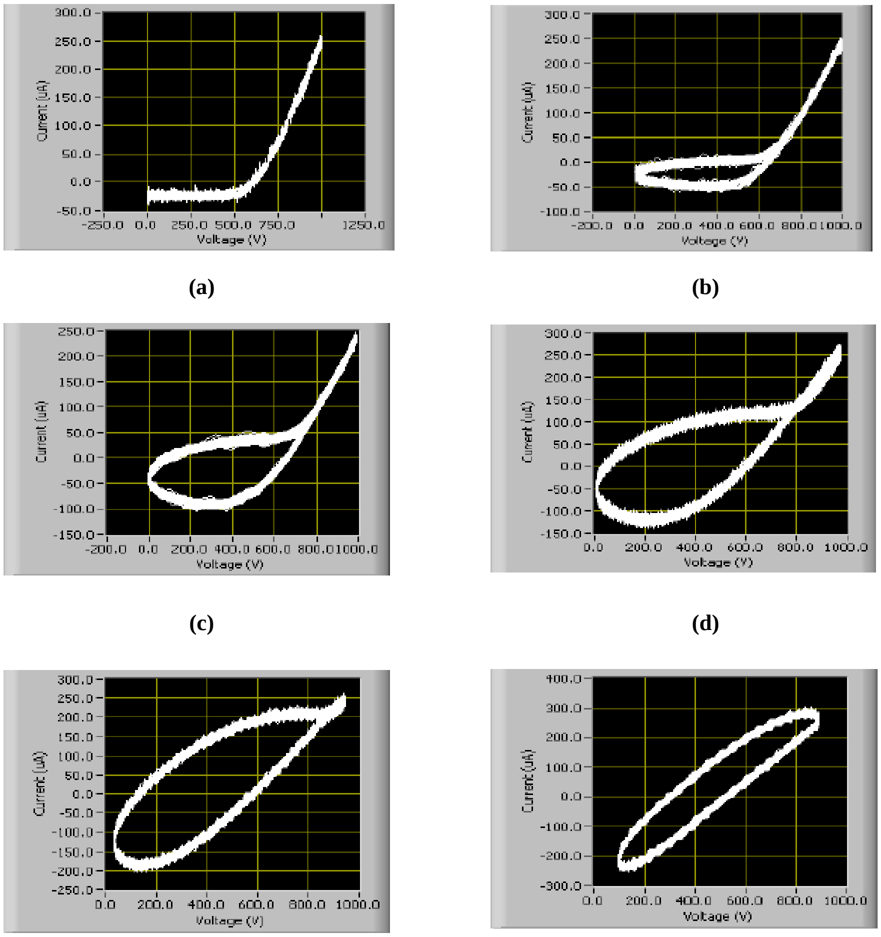

(a) (b) (c) (d) (e) (f)

Figure 5.38: Trends in hysteresis at (a) 1 Hz, (b) 100 Hz, (c) 250 Hz, (d) 500 Hz, (e) 1000 Hz, and (f) 2000 Hz.

the nature of nonlinearity, (ii) estimation of the effective nonlinearity constant, (iii) finding the location of the multi-valued region in current-voltage curve, and (iv) using these findings to either remove hysteresis or calibrate the ramp rate to diminish the effect of hysteresis. This will be one of the future research directions.

5.11 Experimental Investigation of the Crosstalk Phenomenon

In many device applications, multiple pixels of CNTs are used. In such cases, an additional complexity is the leaking of the current from one pixel to the other due to crosstalk phenomenon. In this work, a preliminary study on the crosstalk phenomenon that arises from the combination of using only one CNT source and multiple anodes as opposed to the traditional multiple CNT sources with multiple gates/anodes was performed [143]. The schematic diagram of the diode configuration used for this experiment is shown in Fig. 5.39.

For crosstalk experiments, following four distances between anodes were set: 1.37 mm, 2.07 mm, 3.23 mm, and 4.21 mm. The experiments were performed at a frequency of 1Hz. We started with the experiment where the power was supplied to one anode, while the rest three anodes were grounded. The distance between neighboring anodes was set to 1.37 mm. The corresponding current history is shown in Fig. 5.40. From the figure, it is clearly seen that as the current at the powered anode increases, the current collected at the grounded anode also increases. It is inferred from this figure that the current is leaking from one pixel to the neighboring pixel at a distance of 1.37 mm and there is crosstalk. In the next experiment, the distance between neighboring anodes was increased. It was observed that as the

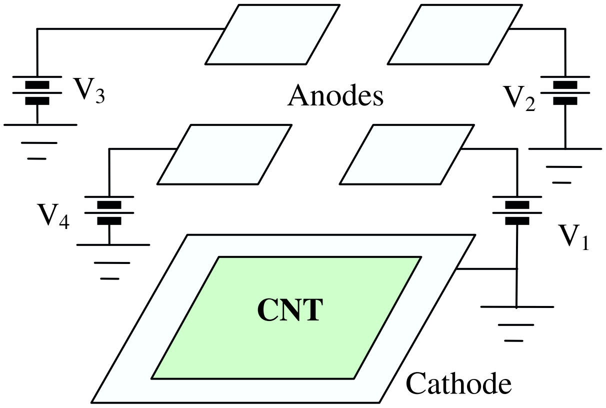

Figure 5.39: The diode configuration inside the vacuum chamber for experiments.

distance between anodes was incresed to 3.23 mm, the current collected at the grounded anode did not increase when the current at the powered anode increased. Instead, it oscillated between a maximum and a minimum, which was mainly noise. It can be concluded that the current at the grounded anode was independent of the current at the powered anode. Therefore, no crosstalk is observed when the neighboring anodes were 3.23 mm apart.

Next, two neighboring anodes were turned on and the distance between the anodes was set to 3.23 mm. The corresponding current history is shown in Fig. 5.41. A close analysis of the figure reveals that the current at the grounded anode increases in steps when the currents at the powered anodes increase. This clearly indicates that crosstalk phenomenon is prevalent in this case. Therefore, a detailed study is required to understand the relationship between separation between anodes and the number of powered and grounded anodes at that point of time.

During the experiments, we observed that the maximum current drawn at different anodes is different when all the anodes are drawing current simultaneously (as also is the case with Fig. 5.41) although the emitting area was approximately

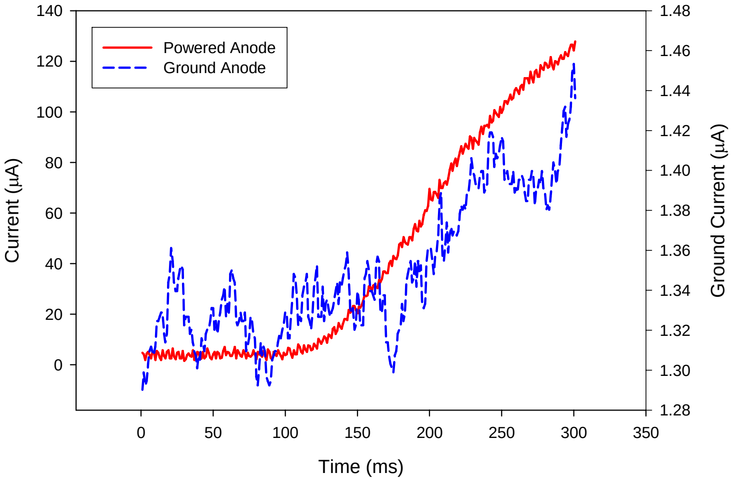

Figure 5.40: Current history of two neighboring pixels with three grounded and one turned on at a distance of 1.37 mm.

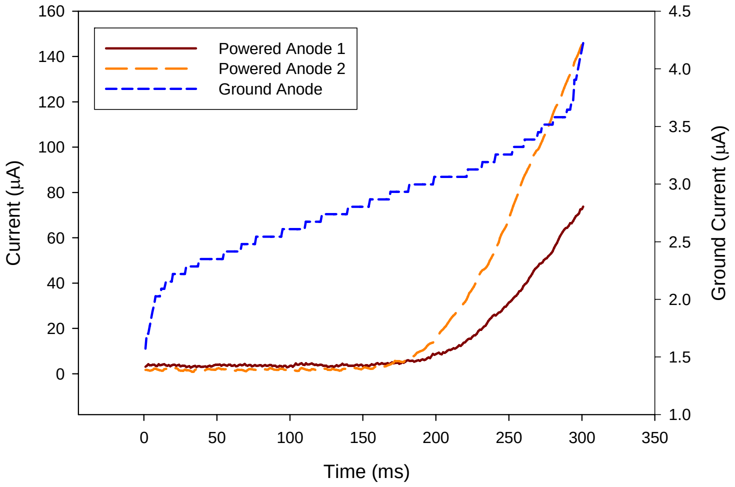

Figure 5.41: Current history of three neighboring pixels with two grounded and the other two turned on at a distance of 3.23 mm.

Table 5.6: Maximum current drawn at each anode.

	Anode 1	Anode 2	Anode 3	Anode 4
Current (μA)	381.2	791.99	547.18	852.56
Voltage (V)	1623.01	1219.19	1460.12	1158.63

Table 5.7: Constant current requirements for the four anodes.

	Anode 1	Anode 2	Anode 3	Anode 4
Current (μA)	381.2	381.2	381.2	381.2
Voltage (V)	1623.01	1070.54	1365.71	991.52

same. The maximum emission currents and corresponding voltages are shown in Table 5.6. The difference in emitted current can be attributed to the morphology of the film, emitting site density, electromechanical interaction of CNTs leading to reorientation, and degradation of CNTs. In order to maintain a constant current at all the anodes for stable performance of the multi-pixel array, we selected the minimum of the maximum currents from the four anodes, and listed the corresponding voltages that were required at all the four anodes (see Table 5.7).

5.12 Conclusion

In this chapter, results related to the proposed multiphysics model were presented. Our analysis shows how the electromechanical interaction among the CNTs influences the orientation of individual CNTs in an ensemble, and consequently, how the distribution of CNTs and geometrical factors affect the device current. Using the developed computational scheme, we were able to capture the transience in the field emission current, which has been observed in actual experiments. In addition, we evaluated the influence of defects and impurities in CNTs on the field emission properties of CNT arrays. Design optimization studies for stable performance of the CNT-based device were also presented in this research. For the first time, it was demonstrated by us that phonon-assisted control of field emission current in a CNT-based thin film is possible. Lastly, experimental studies were conducted to avoid crosstalk phenomenon during field emission in a multi-pixel CNT array. With new findings reported in this study, there are few important aspects that require further attention. They are discussed in the next chapter.

Chapter 6

Conclusions and Future Work

6.1 Contributions of the Thesis

The scientific contributions of this thesis are listed and summarized below.

1. In this thesis, a multiphysics model of CNT field emission has been developed. This model integrates the nucleation coupled model of degradation of CNTs, the electromechanical forces on randomly oriented CNTs, the mechanics of CNTs, and the thermodynamics of electron-phonon interaction in a systematic manner;
2. The published experimental studies indicate that the current history of the device consists of several spikes. The results of simulation described in this study reveal that these spikes are due to the degradation and electrodynamic pull on the CNTs and related coupled phenomena;
3. In addition to capturing the current spikes, the present simulation has also captured the temperature rise at CNT tips, which is in agreement with the

experimental findings reported in literature;

4. An approach for determination of field emission properties of CNT arrays with defects and impurities is developed;
5. A new design for optimization of field emission performance of CNT arrays has been proposed. This design stabilises the fluctuation in field emission current, which is highly desirable for many biomedical applications;
6. The results of this study demonstrate that phonon-assisted control of field emission current in CNT thin films is possible;
7. In this research, preliminary studies related to the crosstalk phenomenon in a single cathode-multi anode configuration have been conducted. The results presented here are significant for multi-pixel CNT arrays, where crosstalk (and the resultant interference/noise) is highly undesirable;
8. For the first time, hysteresis during CNT field emission has been observed and reported in this study. This property has the potential to be utilized in developing many future device applications.

6.2 Future Work

The following topics are suggested as a continuation of the current research.

1. A detailed investigation on the physical mechanism of cluster formation and CNT fragmentation is required, which is an open area of research;

2. As discussed earlier, the current knowledge about the work function of CNTs is limited. Detailed studies for their comprehensive understanding is still awaited;

3. This study (and most of the field emission related studies on CNTs) have mainly focussed on the interaction between CNTs and emission from tips of CNTs. Another important issue that needs attention is the interaction between CNTs and substrates. In particular, it should be determined how the substrate material affects the electron emission phenomenon and the reasons behind it;

4. The studies on the crosstalk phenomenon needs to be investigated further. For instance, in the present study, the voltage was applied in the discrete mode, i.e., 'on' and 'off'. It is worthwhile to look into the effect of applying the voltage in the continuous mode. Also, detailed study of the application of a range of frequencies is required. Another area of research is to reduce the size of the pixels to characterize the performance of the array. Lastly, the performance of single cathode and multiple anode configuration should be compared with the multiple anode and multiple cathode configuration for optimal performance. The incorporation of these factors presents an appealing scope for future research;

5. Although preliminary experimental observations on hysteresis have been reported in this study, detailed investigations on the charaterization of hysteresis from CNT arrays is required;

6. Precision biomedical applications require design of field emission pixels for spatio-temporally controlled x-ray dosage. In order to achieve this goal, fluctuation in field emission current needs to be minimized. Although one design

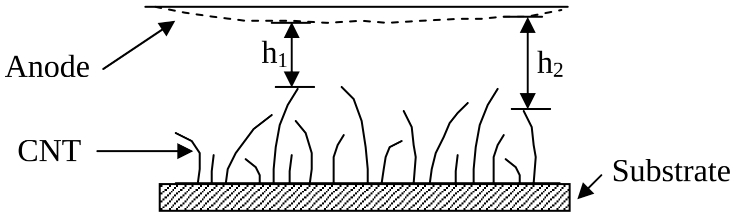

Figure 6.1: Non-uniform distance between the anode surface and the CNT tips leading to current fluctuation.

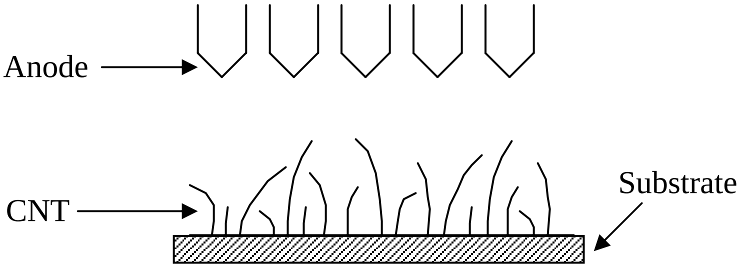

Figure 6.2: Replacement of the flat anode surface with pointed anode may stabilize the current fluctuation.

optimization study has been presented in this thesis, there are some other optimization studies, which should be looked into. These include:

(i) Design of anode for stable performance. Anodes in the state-of-the-art applications are flat surfaces. As it is very difficult to have complete control over the morphology of CNT thin films, situations such as in Fig. 6.1 arise that are very common. Under these circumstances, it is very difficult to maintain uniform distance between CNT tips and the anode surface, which ultimately results in spikes and fluctuations. One possible way is to design pointed anodes as shown in Fig. 6.2.

(ii) It will also be interesting to see if coating the thin film with different materials can result in the stabilization of the field emission current. However, this requires expertise in thin film growth and deposition techniques.

Bibliography

[1] Y. Cheng and O. Zhou, "Electron field emission from carbon nanotubes," *C. R. Physique*, vol. 4, pp. 1021-1033, 2003.

[2] R.H. Fowler and L. Nordheim, "Electron emission in intense electric field," *Proc. Royal Soc. London A*, vol. 119, pp. 173-181, 1928.

[3] C.A. Spindt, I. Brodie, L. Humphrey and E. R. Westerberg, "Physical properties of thin-film field emission cathodes with molybdenum cones," *J. Appl. Phys.*, vol. 47, pp. 5248-5263, 1976.

[4] Y. Gotoh, M. Nagao, D. Nozaki, K. Utsumi, K. Inoue, T. Nakatani, T, Sakashita, K. Betsui, H. Tsuji and J. Ishikawa, "Electron emission properties of Spindt-type platinum field emission cathodes," *J. Appl. Phys.*, vol. 95, pp. 1537-1549, 2004.

[5] W. Zhu (Ed.), Vacuum microelectronics, Wiley, NY (2001).

[6] Lawrence Berkley Nat. Labs [Online]. Available: http://www.lbl.gov

[7] J.G. Wen, Z.P. Huang, D.Z. Wang, J.H. Chen, S.X. Yang, Z.F. Ren, J.H. Wang, L.E. Calvet, J. Chen, J.F. Klemic and M.A. Reed, "Growth and char-

acterization of aligned carbon nanotubes from patterned nickel nanodots and uniform thin films," *J. Mater. Res.*, vol. 16, pp. 3246-3253, 2001.

[8] S. Iijima, "Helical microtubules of graphitic carbon," *Nature*, vol. 354, 56-58, 1991.

[9] A.G. Rinzler, J.H. Hafner, P. Nikolaev, L. Lou, S.G. Kim, D. Tomanek, D. Colbert and R.E. Smalley, "Unraveling nanotubes: field emission from an atomic wire," *Science*, vol. 269, pp. 1550-1553, 1995.

[10] W.A. de Heer, A. Chatelain and D. Ugrate, "A carbon nanotube field-emission electron source," *Science*, vol. 270, pp. 1179-1180, 1995.

[11] L.A. Chernozatonskii, Y.V. Gulyaev, Z.Y. Kosakovskaya, N.I. Sinitsyn, G.V. Torgashov, Y.F. Zakharchenko, E.A. Fedorov and V.P. Valchuk, "Electron field emission from nanofilament carbon films," *Chem. Phys. Lett.*, vol. 233, pp. 63-68, 1995.

[12] J.M. Bonard, J.P. Salvetat, T. Stockli, L. Forro and A. Chatelain, "Field emission from carbon nanotubes: perspectives for applications and clues to the emission mechanism," *Appl. Phys. A*, vol. 69, pp. 245-254, 1999.

[13] Y. Saito and S. Uemura, "Field emission from carbon nanotubes and its application to electron sources," *Carbon*, vol. 38, pp. 169-182, 2000.

[14] H. Sugie, M. Tanemure, V. Filip, K. Iwata, K. Takahashi and F. Okuyama, "Carbon nanotubes as electron source in an x-ray tube," *Appl. Phys. Lett.*, vol. 78, pp. 2578-2580, 2001.

[15] O. Groening, O.M. Kuettel, C. Emmenegger, P. Groening and L. Schlapbach, "Field emission properties of carbon nanotubes of variable heights," *J. Vac. Sci. Technol. B*, vol. 18, pp. 665-678, 2000.

[16] P.G. Collins and A. Zettl, "A simple and robust eleectron beam source from carbon nanotubes," *Appl. Phys. Lett.*, vol. 69, pp. 1969-1971, 1996.

[17] D. Nicolaescu, L.D. Filip, S. Kanemaru and J. Itoh, "Modeling of optimized field emission nanotriodes with aligned carbon nanotubes of variable heights," *Jpn. J. Appl. Phys.*, vol. 43, pp. 485-491, 2004.

[18] D. Nicolaescu, V. Filip, S. Kanemaru and J. Itoh, "Modeling of field emission nanotriodes with carbon nanotube emitters," *J. Vac. Sci. Technol.*, vol. 21, pp. 366-374, 2003.

[19] L. Nilsson, O. Groening, C. Emmeneger, O. Kuettel, E. Schaller, L. Schlapbach, H. Kind, J.-M. Bonard and K. Kern, "Scanning field emission from patterned carbon nanotube films," *Appl. Phys. Lett.*, vol. 76, pp. 2071-2073, 2000.

[20] J.-C. Charlier, "Defects in carbon nanotubes," *Acc. Chem. Res.*, vol. 35, pp. 1063-1069, 2002.

[21] T.W. Odom, J.L. Huang, P. Kim and C.M. Lieber, "Atomic structure and electronic properties of single-walled carbon nanotubes," *Nature*, vol. 391, pp. 62-64, 1998.

[22] T.W. Ebbesen, "Production and purification of carbon nanotubes," in *Carbon Nanotubes: Preparation and Properties*, Ed. T. W. Ebbesen, Boca Raton: CRC Press, 1997, pp. 139-162.

[23] S. Iijima and T. Ichihashi, "Single-shell carbon nanotubes of 1-nm diameter," *Nature*, vol. 363, pp. 603, 1993.

[24] D.S. Bethune, C.H. Kiang, M.S. de Vries, G. Gorman, R. Savoy, J. Vazquez and R. Beyers, "Cobalt-catalysed growth of carbon nanotubes with single-atomic-layer walls," *Nature*, vol. 363, pp. 305, 1993.

[25] H. Li, L. Guan, Z. Shi and Z. Gu, "Direct synthesis of high purity single-walled carbon nanotube fibers by arc discharge," *J. Phys. Chem. B*, vol. 108, pp. 4573-4575, 2004.

[26] M.C. Paladugu, K. Maneesh, P.K. Nair and P. Haridoss, "Synthesis of carbon nanotubes by arc discharge in open air," *J. Nanosci. Nanotechnol.*, vol. 5, pp. 747-752, 2005.

[27] A. Thess, R. Lee, P. Nikolaev, H.J. Dai, P. Petit, J. Robert, C.H. Xu, Y.H. Lee, S.G. Kim, A.G. Rinzler, D.T. Colbert, G.E. Scuseria, D. Tomanek, J.E. Fischer and R.E. Smalley, "Crystalline ropes of metallic carbon nanotubes," *Science*, vol. 273, pp. 483-487, 1996.

[28] S. Arepalli, P. Nikolaev, W. Holmes and B.S. Files, "Production and measurements of individual single-wall nanotubes and small ropes of carbon," *Appl. Phys. Lett.*, vol. 78, pp. 1610, 2001.

[29] C.D. Scott, S. Arepalli, P. Nikolaev and R.E. Smalley, "Growth mechanisms for single-wall carbon nanotubes in a laser-ablation process," *Appl. Phys. A: Materials Science and Processing*, vol. 72, pp. 573-580, 2001.

[30] S. Takahashi, T. Ikuno, T. Oyama, S.I. Honda, M. Katayama, T. Hirao and K. Oura, "Synthesis and characterization of carbon nanotubes grown on carbon

particles by using high vacuum laser ablation," *J. Vac. Soc. Jpn.*, vol. 45, pp. 609-612, 2002.

[31] H. Dai, "Nanotube growth and characterization," *Topics Appl. Phys.*, vol. 80, pp. 29-54, 2001.

[32] M.J. Yacaman, M.M. Yoshida, L. Rendon and J.G. Santiesteban, "Catalytic growth of carbon microtubules with fullerene structure," *Appl. Phys. Lett.*, vol. 62, pp. 202-204, 1993.

[33] V.K. Varadan and J. Xie, "Large-scale synthesis of multi-walled carbon nanotubes by microwave CVD," *Smart Mat. Struc.*, vol. 11, pp. 610-616, 2002.

[34] D. Park, Y.H. Kim and J.K. Lee, "Synthesis of carbon nanotubes on metallic substrates by a sequential combination of PECVD and thermal CVD," *Carbon*, vol. 41, pp. 1025-1029, 2003.

[35] B.Q. Wei, R. Vajtai, Y. Jung, J. Ward, R. Zhang, G. Ramanath and P.M. Ajayan, "Organized assembly of carbon nanotubes ," *Nature*, vol. 416, pp. 495, 2002.

[36] T.W. Ebbesen, P.M. Ajayan, H. Hiura and K. Tanigaki, "Purification of nanotubes," *Nature*, vol. 367, pp. 519, 1994.

[37] H. Hiura, T.W. Ebbesen and K. Tanigaki, "Opening and purification of carbon nanotubes in high yields," *Adv. Mat.*, vol. 7, pp. 275-276, 1995.

[38] C. Xu, E. Flahaut, S.R. Bailey, G. Brown, J. Sloan, K.S. Coleman, V.C. Williams and M.L.H. Green, "Purification of single-walled carbon nanotubes grown by a chemical vapor deposition (CVD) method," *Chem. Res. Chinese Univ.*, vol. 18, pp. 130, 2002.

[39] L.P. Biro, N.Q. Khanh, Z. Vertesy, Z.E. Horvath, Z. Osvath, A. Koos, J. Gyulai, A. Kocsonya, Z. Konya, X.B. Zhang, G.V. Tendeloo, A. Fonseca and J.B. Nagy, "Catalyst traces and other impurities in chemically purified carbon nanotubes grown by CVD," *Mat. Sci. Eng. C*, vol. C19, pp. 9, 2002.

[40] E W. Wong, P.E. Sheehan and C.M. Lieber, "Nanobeam mechanics : Elasticity, strength, and toughness of nanorods and nanotubes," *Science*, vol. 277, pp. 1971-1975, 1997.

[41] R. Saito, M. Fujita, G. Desselhaus and M.S. Dresselhaus, "Electronic structure of chiral graphene tubules," *Appl. Phys. Lett.*, vol. 60, pp. 2204-2206, 1992.

[42] R.H. Baughman, A.A. Zakhidov and W.A. de Heer, "Carbon nanotubes-the route toward applications," *Science*, vol. 297, pp. 787-792, 2002.

[43] M. Terrones, "Science and technology of the twenty-first century: synthesis, properties, and applications of carbon nanotubes," *Ann. Rev. Mat. Res.*, vol. 33, pp. 419-501, 2003.

[44] M.S. Dresselhaus, P.C. Eklund and R. Saito, "Carbon nanotubes," *Phys. World*, vol. 33, 1998.

[45] M.S. Dresselhaus, G. Dresselhaus and P.C. Eklund, *Science of Fullerenes and Carbon Nanotubes* (Academic Press, NY, 1996).

[46] S.G. Louie, "Electronic properties, junctions, and defects of carbon nanotubes," *Topics Appl. Phys.*, vol. 80, pp. 113-146, 2001.

[47] R.S. Ruoff, D. Qian and W.K. Liu, "Mechanical properties of carbon nanotubes: theoretical predictions and experimental measurements," *C.R. Physique*, vol. 4, pp. 993-1008, 2003.

[48] S. Amelinckx, D. Bernaerts, X.B. Zhang, G. van Tendeloo and J. van Landuyt, "A structure model and growth mechanism for multishell carbon nanotubes," *Science*, vol. 267, pp. 1334-1338, 1995.

[49] W. Liang, M. Bockrath, D. Bozovic, J.H. Hafner, M. Tinkham and H. Park, "Fabry-perot interference in a nanotube electron waveguide," *Nature*, vol. 411, pp. 665-669, 2001.

[50] B.Q. Wei, R. Vajtai and P.M. Ajayan, "Reliability and current carrying capacity of carbon nanotubes," *Appl. Phys. Lett.*, vol. 79, pp. 1172, 2001.

[51] G.U. Sumanasekera, C.K.W. Adu, S. Fang and P.C. Eklund, "Effects of gas adsorption and collisions on electrical transport in single-walled carbon nanotubes ," *Phys. Rev. Lett.*, vol. 85, pp. 1096-1099, 2000.

[52] L. Chico, V.H. Crespi, L.X. Benedict, S.G. Louie and M.L. Cohen, "Pure carbon nanoscale devices: nanotube heterojunctions," *Phys. Rev. Lett.*, vol. 76, pp. 971-974, 1996.

[53] A. Rochefort, D.R. Salahub and P. Avouris, "The effect of structural distortions on the electronic structure of carbon nanotubes," *Chem. Phys. Lett.*, vol. 297, pp. 45-50, 1998.

[54] D. Danailov, P. Keblinski, S. Nayak and P.M. Ajayan, "Bending properties of carbon nanotubes encapsulating solid nanowires," *J. Nanosci. Nanotechnol.*, vol. 2, pp. 503-507, 2002.

[55] A. Rochefort, P. Avouris, F. Lesage and D.R. Salahub, "Electrical and mechanical properties of distorted carbon nanotubes," *Phys. Rev. B*, vol. 60, pp. 13824-13830, 1999.

[56] M. Kociak, A.Y. Kasimov, S. Gueron, B. Reulet, I.I. Khodos, Y.B. Gorbatov, V.T. Volkov, L. Vaccarini and H. Bouchiat, "Superconductivity in ropes of single-walled carbon nanotubes," *Phys. Rev. Lett.*, vol. 86, pp. 2416-2419, 2001.

[57] J. Zhaoa and R. Xie, "Electronic and photonic properties of doped carbon nanotubes," *J. Nanosci. Nanotechnol.*, vol. 3, pp. 459-478, 2003.

[58] M.M.J. Treacy, T.W. Ebbesen and J.M. Gibson, "Exceptionally high young's modulus observed for individual carbon nanotubes," *Nature*, vol. 381, pp. 678-680, 1996.

[59] M.R. Falvo, G.J. Clary, R.M. Taylor, V. Chi, F.P. Brooks, S. Washburn and R. Superfine, "Bending and buckling of carbon nanotubes under large strain," *Nature*, vol. 389, pp. 582-584, 1997.

[60] J. Gaillard, M. Skove and A.M. Rao, "Mechanical properties of chemical vapor deposition-grown multiwalled carbon nanotubes," *Appl. Phys. Lett.*, vol. 86, pp. 233109, 2005.

[61] O. Lourie and H.D. Wagner, "Evaluation of young's modulus of carbon nanotubes by micro-raman spectroscopy," *J. Mat. Res.*, vol. 13, pp. 2418-2422, 1998.

[62] M.F. Yu, B.S. Files, S. Arepalli and R.S. Ruoff, "Tensile loading of ropes of single wall carbon nanotubes and their mechanical properties," *Phys. Rev. Lett.*, vol. 84, pp. 5552-5555, 2000.

[63] M.F. Yu, O. Lourie, M.J. Dyer, K. Moloni, T.F. Kelly and R.S. Ruoff, "Strength and breaking mechanism of multiwalled carbon nanotubes under tensile load," *Science*, vol. 287, pp. 637-640, 2000.

[64] P. Jaroenapibal, D.E. Luzzi, S. Evoy and S. Arepalli, "Transmission-electron-microscopic studies of mechanical properties of single-walled carbon nanotube bundles," *Appl. Phys. Lett.*, vol. 85, pp. 4328, 2004.

[65] O. Lourie, D.M. Cox and H.D. Wagner, "Buckling and collapse of embedded carbon nanotubes," *Phys. Rev. Lett.*, vol. 81, pp. 1638-1641, 1998.

[66] P.H. Zhang, P.E. Lammert and V.H. Crespi, "Plastic deformations of carbon nanotubes," *Phys. Rev. Lett.*, vol. 81, pp. 5346-5349, 1998.

[67] T. Belytschko, S.P. Xia, G.C. Schatz and R.S. Rouff, "Atomistic simulations of nanotube fracture," *Phys. Rev. B*, vol. 65, pp. 235430(1-8), 2002.

[68] J.P. Salvetat, J.M. Bonard, N.H. Thomson, A.J. Kulik, L. Forro, W. Benoit and L. Zuppiroli, "Mechanical properties of carbon nanotubes," *Appl. Phys. A: Materials Science and Engineering*, vol. 69, pp. 255-260, 1999.

[69] M.B. Nardelli, B.I. Yakobson and J. Bernholc, "Mechanism of strain release in carbon nanotubes," *Phys. Rev. B*, vol. 57, pp. R4277, 1998.

[70] M.C. Weisenberger, E.A. Grulke, D. Jacques, A.T. Rantell and R. Andrews, "Enhanced mechanical properties of polyacrylonitrile/multiwall carbon nanotube composite fibers ," *J. Nanosci. Nanotechnol.*, vol. 3, pp. 535-539, 2003.

[71] H. Miyagawa, M. Misra and A.K. Mohanty, "Mechanical properties of carbon nanotubes and their polymer nanocomposites," *J. Nanosci. Nanotechnol.*, vol. 5, pp. 1593-1615, 2005.

[72] J. Suhr, N. Koratkar, P. Keblinski and P.M. Ajayan, "Viscoelasticity in carbon nanotube composites," *Nature Mater.*, vol. 4, pp. 134-137, 2005.

[73] J. Hone, M.C. Llaguno, N.M. Nemes, A.T. Johnson, J.E. Fischer, D.A. Walters, M J. Casavant, J. Schmidt and R.E. Smalley, “Electrical and thermal transport properties of magnetically aligned single wall carbon nanotube films,” *Appl. Phys. Lett.*, vol. 77, pp. 666-668, 2000.

[74] W. Yi, L. Lu, D.L. Zhang, Z.W. Pan and S.S. Xie, “Linear specific heat of carbon nanotubes,” *Phys. Rev. B*, vol. 59, pp. R9015, 1999.

[75] A. Mizel, L.X. Benedict, M.L. Cohen, S.G. Louie, A. Zettl, N.K. Budraa and W.P. Beyermann, “Analysis of the low-temperature specific heat of multiwalled carbon nanotubes and carbon nanotube ropes,” *Phys. Rev. B*, vol. 60, pp. 3264, 1999.

[76] J.C. Lasjaunias, K. Biljakoviae, Z. Benes, J.E. Fischer and P. Monceau, “Low-temperature specific heat of single-wall carbon nanotubes,” *Phys. Rev. B*, vol. 65, pp. 113409, 2002.

[77] J. Hone, M. Whitney, C. Piskoti and A. Zettl, “Thermal conductivity of single-walled carbon nanotubes,” *Phys. Rev. B*, vol. 59, pp. R2514, 1999.

[78] P. Kim, L. Shi, A. Majumdar and P.L. McEuen, “Thermal transport measurements of individual multiwalled nanotubes,” *Phys. Rev. Lett.*, vol. 87, pp. 215502 (1-4), 2001.

[79] W. Zhang, Z. Zhu, F. Wang, T. Wang, L. Sun and Z. Wang, “Chirality dependence of the thermal conductivity of carbon nanotubes,” *Nanotechnology*, vol. 15, pp. 936-939, 2004.

[80] D. Lovall, M. Buss, E. Graugnard, R.P. Andres and R. Reifenberger, “Electron emission and structural characterization of a rope of single-walled carbon nanotubes,” *Phys. Rev. B*, vol. 61, pp. 5683-5691, 2000.

[81] S.T. Purcell, P. Vincent, C. Journet and V.T. Binh, "Hot nanotubes: stable heating of individual multiwall carbon nanotube to 2000 K induced by the field-emission current," *Phys. Rev. Lett.*, vol. 88, pp. 105502, 2002.

[82] S.T. Purcell, P. Vincent, C. Journet and V.T. Binh, "Tuning of nanotube mechanical resonances by electric field pulling ," *Phys. Rev. Lett.*, vol. 89, pp. 276103, 2002.

[83] J.M. Bonard, M. Croci, F. Conus, T. Stockli and A. Chatelain, "Watching carbon nanotubes grow," *Appl. Phys. Lett.*, vol. 81, pp. 2836-2838, 2002.

[84] J.M. Bonard, M. Croci, C. Klinke, F. Conus, I. Arfaoui, T. Stockli and A. Chatelain, "Growth of carbon nanotubes characterized by field emission measurements during chemical vapor deposition," *Phys. Rev. B*, vol. 67, pp. 085412, 2003.

[85] J.M. Bonard, F. Maier, T. Stockli, A. Chatelain, W.A. de Heer, J.P. Salvetat and L. Forro, "Field emission properties of multiwalled carbon nanotubes," *Ultramicroscopy*, vol. 73, pp. 7-15, 1998.

[86] K.A. Dean, T.P. Burgin and B.R. Chalamala, "Evaporation of carbon nanotubes during electron field emission," *Appl. Phys. Lett.*, vol. 79, pp. 1873-1875, 2001.

[87] Y. Wei, C. Xie, K.A. Dean and B.F. Coll, "Stability of carbon nanotubes under electric field studied by scanning electron microscopy," *Appl. Phys. Lett.*, vol. 79, pp. 4527-4529, 2001.

[88] Z.L. Wang, R.P. Gao, W.A. de Heer and P. Poncharal, "*In situ* imaging of field emission from individual carbon nanotubes and their structural damage," *Appl. Phys. Lett.*, vol. 80, pp. 856-858, 2002.

[89] J. Chung, K.H. Lee, J. Lee, D. Troya and G.C. Schatz, “Multi-walled carbon nanotubes experiencing electrical breakdown as gas sensors,” *Nanotechnology* vol. 15, pp. 1596-1602, 2004.

[90] P. Avouris, R. Martel, H. Ikeda, M. Hersam, H.R. Shea and A. Rochefort, “Electrical properties of carbon nanotubes: spectroscopy, localization and electrical breakdown,” *Fundamental Mater. Res. Series: Sci. Appl. Nanotubes*, D. Tomanek and R.J. Enbody (Ed.), Kluwer Academic/Plenum Publishers, pp.223-237, 2000.

[91] L. Nilsson, O. Groening, P. Groening and L. Schlapbach, “Collective emission degradation behavior of carbon nanotube thin-film electron emitters,” *Appl. Phys. Lett.*, vol. 79, pp. 1036-1038, 2001.

[92] L. Nilsson, O. Groening, P. Groening and L. Schlapbach, “Characterization of thin film electron emitters by scanning anode field emission microscopy,” *J. Appl. Phys.*, vol. 90, pp. 768-780, 2001.

[93] J.M. Bonard, C. Klinke, K.A. Dean and B.F. Coll, “Degradation and failure of carbon nanotube field emitters,” *Phys. Rev. B*, vol. 67, pp. 115406 (1-10), 2003.

[94] J.M. Bonard, N. Weiss, H. Kind, T. Stockli, L. Forro, K. Kern and A. Chatelain, “Tuning the field emission properties of patterned carbon nanotube films,” *Adv. Mater.*, vol. 13, pp. 184-188, 2001.

[95] J.M. Bonard, J.P. Salvetat, T. Stockli, W.A. de Heer, L. Forro and A. Chatelain, “Field emission from single-wall carbon nanotube films,” *Appl. Phys. Lett.*, vol. 73, pp. 918-920, 1998.

[96] S.C. Lim, H.J. Jeong, Y.S. Park, D.S. Bae, Y.C. Choi, Y.M. Shin, W.S. Kim, K.H. An and Y.H. Lee, "Field emission properties of vertically aligned carbon-nanotube array dependent on gas exposures and growth conditions," *J. Vac. Sci. Technol. A*, vol. 19, pp. 1786-1789, 2001.

[97] N.Y. Huang, J.C. She, J. Chen, S.Z. Deng, N.S. Xu, H. Bishop, S.E. Huq, L. Wang, D.Y. Zhong, E.G. Wang and D.M. Chen, "Mechanism responsible for initiating carbon nanotube vacuum breakdown," *Phys. Rev. Lett.*, vol. 93, pp. 075501 (1-4), 2004.

[98] X.Y. Zhu, S.M. Lee, Y.H. Lee and T. Frauenheim, "Adsorption and desorption of an O_2 molecule on carbon nanotubes," *Phys. Rev. Lett.*, vol. 85, pp. 2757-2760, 2000.

[99] N. Sinha, D. Roy Mahapatra, J.T.W. Yeow, R.V.N. Melnik and D.A. Jaffray, "Carbon nanotube thin film field emitting diode: Understanding the system response based on multiphysics modelling," *J. Comp. Theor. Nanosci.*, vol. 4, pp. 535-549, 2007.

[100] G.Y. Slepyan, S.A. Maksimenko, A. Lakhtakia, O. Yevtushenko and A. V. Gusakov, "Electrodynamics of carbon nanotubes: Dynamic conductivity, impedance boundary conditions, and surface wave propagation," *Phys. Rev. B*, vol. 60, no. 24, pp. 17136-17149, 1999.

[101] N. Sinha, D. Roy Mahapatra, J.T.W. Yeow, R.V.N. Melnik and D.A. Jaffray, "Characterization of self-assembly and evolution in carbon nanotube thin film field emitter," *Proc. 6th IEEE Conf. Nanotech.*, Cincinnati, USA, July 16-20, 2006.

[102] S.K. Friedlander, "Dynamics of aerosol formation by chemical reactions," *Ann. N.Y. Acad. Sci.*, vol. 404, pp. 354-364, 1983.

[103] S.L. Grishick, C.P. Chiu and P.H. McMurry, "Time-dependent aerosol models and homogeneous nucleation rates," *Aerosol Sci. Technol.*, vol. 13, pp. 465-477, 1990.

[104] N. Sinha, D. Roy Mahapatra, Y. Sun, J.T.W. Yeow, R.V.N. Melnik and D.A. Jaffray, "Electromechanical interactions in a carbon nanotube thin film field emitting diode," *Nanotechnology*, vol. 19, pp. 25701 (1-12), 2008.

[105] T. Watanabe, T. Notoya, T. Ishigaki, H. Kuwano, H. Tanaka and Y. Moriyoshi, "Growth mechanism for carbon nanotubes in a plasma evaporation process," *Thin Solid Films*, vol. 506-507, pp. 263-267, 2006.

[106] T. Watanabe and K. Fujiwara, "Nucleation and growth of oxide nanoparticles prepared by induction thermal plasmas," *Chem. Engg. Comm.*, vol. 191, pp. 1343-1361, 2004.

[107] T. Watanabe and H. Okumiya, "Formation mechanism of silicide nanoparticles by induction thermal plasmas," *Sci. Technol. Adv. Mater.*, vol. 5, pp. 639-646, 2004.

[108] J.E. Farrell and O.T. Valls, "Growth kinetics and domain morphology after off-critical quenches in a two-dimensional fluid model," *Phys. Rev. B*, vol. 43, pp. 630-640, 1991.

[109] H. Jiang, P. Zhang, B. Liu, Y. Huang, P.H. Geubelle, H. Gao and K.C. Hwang, "The effect of nanotube radius on the constitutive model for carbon nanotubes," *Comp. Mat. Sci.*, vol. 28, pp. 429-442, 2003.

[110] N. Sinha, D. Roy Mahapatra, J.T.W. Yeow and R.V.N. Melnik, "Modeling the field emission current fluctuation in carbon nanotube thin films," *Proc. 10th Annual NSTI Nanotech. Conf.*, Santa Clara, USA, May 20-24, 2007.

[111] A. Svizhenko and M.P. Anantram, "Effect of scattering and contacts on current and electrostatics in carbon nanotubes," *Phys. Rev. B*, vol. 72, pp. 085430 (1-10), 2005.

[112] O.E. Glukhova, A.I. Zhbanov, I.G. Torgashov, N.I. Sinistyn and G.V. Torgashov, "Ponderomotive forces effect on the field emission of carbon nanotube films," *Appl. Surf. Sci.*, vol. 215, pp. 149-159, 2003.

[113] A.L. Musatov, N.A. Kiselev, D.N. Zakharov, E.F. Kukovitskii, A.I. Zhbanov, K.R. Izrael'yants and E.G. Chirkova, "Field electron emission from nanotube carbon layers grown by CVD process," *Appl. Surf. Sci.*, vol. 183, pp. 111-119, 2001.

[114] R.S. Ruoff, J. Tersoff, D.C. Lorents, S. Subramoney and B. Chan, "Radial deformation of carbon nanotubes by van der Waals forces," *Nature*, vol. 364, pp. 514-516, 1993.

[115] T. Hertel, R.E. Walkup and P. Avouris, "Deformation of carbon nanotubes by surface van der Waals forces," *Phys. Rev. B*, vol. 58, pp. 13870-13873, 1998.

[116] J.N. Reddy, 2002 *Energy principles and variational methods in applied mechanics*, New Jersey: John Wiley.

[117] W.W. Dolan, W.P. Dyke and J.K. Trolan, "The field emission initiated vacuum arc II. the resistively heated emitter," *Phys. Rev.*, vol. 91, pp. 1054-1057, 1953.

[118] W.B. Nottingham, “Remarks on energy losses attending thermionic emission of electrons from metals,” *Phys. Rev.*, vol. 59, pp. 906-907, 1941.

[119] H.-Y. Chiu, V.V. Deshpande, H.W.Ch. Postma, C.N. Lau, C. Mikó, L. Forró and M. Bockrath, “Ballistic phonon thermal transport in multiwalled carbon nanotubes,” *Phys. Rev. Lett.*, vol. 95, pp. 226101 (1-4), 2005.

[120] T. Yamamoto, S. Watanabe and K. Watanabe, “Universal features of quantized thermal conductance of carbon nanotubes,” *Phys. Rev. Lett.*, vol. 92, pp. 075502 (1-4), 2004.

[121] N. Sinha, D. Roy Mahapatra, J.T.W. Yeow and R.V.N. Melnik, “Multi-mode phonon-controlled field emission from carbon nanotubes: modeling and experiments,” *Proc. 7th IEEE Int. Conf. Nanotechol.*, Hong Kong, pp. 961-964, 2007.

[122] L. Wei and Y.-N. Wang, “Electromagnetic wave propagation in single-wall carbon nanotubes,” *Phys. Lett. A*, vol. 333, pp. 303-309, 2004.

[123] J.R. Xiao, B.A. Gama and J.W. Gillespie, “An analytical molecular structural mechanics model for the mechanical properties of carbon nanotubes,” *Int. J. Solids Struc.*, vol. 42, pp. 3075-3092, 2005.

[124] Z.P. Huang, J.W. Xu, Z.F. Ren, J.H. Wang, M.P. Siegal and P.N. Provencio, “Growth of highly oriented carbon nanotubes via plasma-enhanced hot filament chemical vapor deposition,” *Appl. Phys. Lett.*, vol. 73, pp. 3845, 1998.

[125] N. Sinha, Y. sun and J.T.W. Yeow, “Field emission properties of carbon nanotube thin films grown on different substrate materials,” *8th IEEE International Conference on Nanotechnology*, Arlington, USA, (Accepted).

[126] E. Rabbani, "Preliminary investigation of field emission from carbon nanotubes," *Co-op Project Report*, University of Waterloo, 2004.

[127] J.W. Gadzuk and E.W. Plummer, "Field emission energy distribution," *Rev. Mod. Phys.*, vol. 45, pp. 487-548, 1973.

[128] K.A. Dean, O. Groening, O.M. Kuttel and L. Schlapbach, "Nanotube electronic states observed with thermal field emission electron spectroscopy," *Appl. Phys. Lett.*, vol. 75, pp. 2773-2775, 1999.

[129] A. Takakura, K. Hata, Y. Saito, K. Matsuda, T. Kona and C. Oshima, "Energy distributions of field emitted electrons from a multi-wall carbon nanotube," *Ultramicroscopy*, vol. 95, pp. 139-143, 2003.

[130] S. Suzuki, C. Bower, Y. Watanabe and O. Zhou, "Work functions and valence band states of pristine and Cs-intercalated single-walled carbon nanotube bundles," *Appl. Phys. Lett.*, vol. 76, pp. 4007-4009, 2000.

[131] H. Ago, T. Kugler, F. Cacialli, W.R. Salaneck, M.S.P. Shaffer, A.H. Windle and R.H. Friend, "Work functions and surface functional groups of multiwall carbon nanotubes," *J. Phys. Chem. B*, vol. 103, pp. 8116-8121, 1999.

[132] M.J. Fransen, T.L. van Rooy and P. Kruit, "Field emission energy distributions from individual multiwalled carbon nanotubes," *Appl. Surf. Sci.*, vol. 146, pp. 312-327, 1999.

[133] M. Shiraishi and M. Ata, "Work function of carbon nanotubes," *Carbon*, vol. 39, pp. 1913-1917, 2001.

[134] N.I. Sinitsyn, Y.V. Gulyaev, G.V. Torgashov, L.A. Chernozatonskii, Z.Y. Kosakovskaya, Y.F. Zakharchenko, N.A. Kiselev, A.L. Musatov, A.I. Zhbanov,

S.T. Mevlyut and O.E. Glukhova, "Thin films consisting of carbon nanotubes as a new material for emission electronics," *Appl. Surf. Sci.*, vol. 111, pp. 145-150, 1997.

[135] A.N. Obraztsov, A.P. Volkov and I. Pavlovsky, "Field emission from nanostructured carbon materials," *Diam. Rel. Mater.*, vol. 9, pp. 1190-1195, 2000.

[136] Z.P. Huang, Y. Tu, D.L. Carnahan and Z.F. Ren, "Field emission of carbon nanotubes," *Encyl. Nanosci. Nanotechnol.* (Ed. H. S. Nalwa), vol. 3, pp. 401-416, 2004.

[137] N. Sinha, D. Roy Mahapatra, R.V.N. Melnik and J.T.W. Yeow, "Computational implementation of a new multiphysics model for field emission from CNT thin films," *International Conference on Computational Science*, Krakow, Poland, (To appear in Lecture Notes in Computer Science).

[138] A.I. Zhbanov and O.E. Glukhova, "Lengthening of nanotubes in strong electrical fields," *Proc. 14th Int. Microelect. Conf.*, pp. 63-64, 2001.

[139] L. Yang, M.P. Anantram, J. Han and J.P. Lu, "Band-gap change of carbon nanotubes: Effect of uniaxial and torsional strain," *Phys. Rev. B*, vol. 60, pp. 13874-13878, 1999.

[140] D. Roy Mahapatra, N. Sinha, R.V.N. Melnik and J.T.W. Yeow, "Field emission properties of carbon nanotube arrays with defects and impurities," *Proc. 11th Ann. NSTI Nanotech. Conf.*, Boston, USA (Accepted).

[141] D. Roy Mahapatra, N. Sinha, R.V.N. Melnik and J.T.W. Yeow, "Design optimization of field emission from a stacked carbon nanotube array," *Proc. 11th Ann. NSTI Nanotech. Conf.*, Boston, USA (Accepted).

[142] D. Roy Mahapatra, N. Sinha, R.V.N. Melnik and J.T.W. Yeow, "Characterizing hysteresis in field emission from carbon nanotube arrays," *Proc. 6th EUROMECH Nonlinear Dynamics Conf.*, Saint Petersburg, Russia (Accepted).

[143] N. Sinha, J.T.W. Yeow and D.A. Jaffray, "Experimental investigation of the crosstalk phenomenon and current stability in a carbon nanotube array," *Proc. 7th IEEE Int. Conf. Nanotech.*, Hong Kong, pp. 194-197, 2007.

Appendices

Appendix A

Discretization of the nucleation coupled model for degradation

With the help of Eqs. (3.17)-(3.19) and by eliminating the kinetic nucleation rate N_{kin}, we first rewrite the simplified form of Eqs. (3.13)-(3.16), which are given by, respectively,

$$S\frac{dn_1}{dt} - n_1\frac{dS}{dt} = \frac{\beta_{11}n_s^2S^3}{12}\sqrt{\frac{\Theta}{2\pi}}\exp\left[\Theta - \frac{4\Theta^3}{27(\ln S)^2}\right] , \tag{A.1}$$

$$\frac{dS}{dt} = -\frac{2\beta_{11}n_s\Theta S}{81\sqrt{2\pi}(\ln S)^3}\exp\left[\Theta - \frac{4\Theta^3}{27(\ln s)^2}\right] - \sqrt{\frac{kT}{2\pi m_1}}(S-1)A_n , \tag{A.2}$$

$$\frac{dM_1}{dt} = \frac{\beta_{11}n_s^2d_p^*S}{12}\sqrt{\frac{\Theta}{2\pi}}\exp\left[\Theta - \frac{4\Theta^3}{27(\ln S)^2}\right] + 2n_s^2v_1\exp(\Theta)\sqrt{\frac{kT}{2\pi m_1}}(S-1) , \tag{A.3}$$

$$\frac{dA_n}{dt} = \frac{\beta_{11}n_s^2s_1\Theta^{5/2}S}{27\sqrt{2\pi}(\ln S)^2}\exp\left[\Theta - \frac{4\Theta^3}{27(\ln S)^2}\right] + 4\pi n_s v_1\sqrt{\frac{kT}{2\pi m_1}}M_1(S-1) . \tag{A.4}$$

By eliminating dS/dt from Eq. (A.1) with the help of Eq. (A.2) and by applying a finite difference formula in time, we get

$$\frac{n_{1_i} - n_{1_{i-1}}}{t_i - t_{i-1}} \approx \frac{\beta_{11}n_{1_i}^2}{12}\sqrt{\frac{\Theta}{2\pi}}\exp\left(-\frac{4\Theta^3}{27(\ln S_{i-1})^2}\right) - \frac{2\beta_{11}}{81}\frac{\Theta^{7/2}}{\sqrt{2\pi}}\frac{n_{1_i}^2}{S_i}$$

$$\frac{\exp\left(\Theta - \frac{4\Theta^3}{27(\ln S_{i-1})^2}\right)}{(\ln S_{i-1})^3} + \frac{n_{1_i}^2 (S_i - 1) A_n(i)}{S_i^2}\sqrt{\frac{kT}{2\pi m_1}} \; . \tag{A.5}$$

Similarly, Eqs. (A.2)-(A.4) are discretized as, respectively,

$$\frac{S_i - S_{i-1}}{t_i - t_{i-1}} \approx -\frac{2\beta_{11}}{81}\frac{\Theta^{7/2}}{\sqrt{2\pi}} n_{1_i} \frac{\exp\left(\Theta - \frac{4\Theta^3}{27(\ln S_{i-1})^2}\right)}{(\ln S_{i-1})^3} - \frac{n_{1_i}(S_i - 1)A_{n_i}}{S_i}\sqrt{\frac{kT}{2\pi m_1}} \; , \tag{A.6}$$

$$\begin{aligned} \frac{M_{1_i} - M_{1_{i-1}}}{t_i - t_{i-1}} &\approx \frac{\beta_{11} n_{1_i}^2}{12 S_i} d_p^* \sqrt{\frac{\Theta}{2\pi}} \exp\left(\Theta - \frac{4\Theta^3}{27(\ln S_{i-1})^2}\right) \\ &\quad + 2v_1 \frac{n_{1_i}^2 (S_i - 1)}{S_i^2} \exp(\Theta) \sqrt{\frac{kT}{2\pi m_1}} \; , \end{aligned} \tag{A.7}$$

$$\frac{A_{n_i} - A_{n_{i-1}}}{t_i - t_{i-1}} \approx \frac{\beta_{11} s_1 \Theta^{5/2} n_{1_i}}{27\sqrt{2\pi}} \frac{\exp\left(\Theta - \frac{4\Theta^3}{27(\ln S_{i-1})^2}\right)}{(\ln S_{i-1})^2} + 4\pi v_1 \sqrt{\frac{kT}{2\pi m_1}} (S_i - 1) M_{1_i} \; . \tag{A.8}$$

By simplifying Eq. (A.5) with the help of Eqs. (A.6)-(A.8), we get a quadratic polynomial of the form

$$(b_1 - b_2 - b_3){n_{1_i}}^2 - n_{1_i} + n_{1_{i-1}} = 0 \; , \tag{A.9}$$

where

$$b_1 = \Delta t \frac{\beta_{11}}{12} \sqrt{\frac{\Theta}{2\pi}} \exp\left(-\frac{4\Theta^3}{27(\ln S_{i-1})^2}\right) \; , \tag{A.10}$$

$$b_2 = \Delta t \frac{2\beta_{11}}{81} \frac{\Theta^{7/2}}{\sqrt{2\pi}} \frac{\exp\left(\Theta - \frac{4\Theta^3}{27(\ln S_{i-1})^2}\right)}{S_i (\ln S_{i-1})^3} \; , \tag{A.11}$$

$$b_3 = \Delta t \frac{S_i - 1}{S_i^2} A_{n_i} \sqrt{\frac{kT}{2\pi m_1}} \; . \tag{A.12}$$

Solution of Eq. (A.9) yields two roots (denoted by superscripts $(1,2)$):

$$n_{1_i}^{(1,2)} = \frac{1}{2(b_1 - b_2 - b_3)} \pm \frac{\sqrt{1 - 4 n_{1_{i-1}} (b_1 - b_2 - b_3)}}{2(b_1 - b_2 - b_3)} \; . \tag{A.13}$$

For the first time step, the values of b_1, b_2 and b_3 are obtained by applying the initial conditions: $S(0) = S_0$, $n_{1_0} = n_0$, and $A_{n_0} = A_{n0}$. Since the n_{1_i} must be real and finite, the following two conditions are imposed: $1 - 4n_{1_{i-1}}(b_1 - b_2 - b_3) \geq 0$ and $(b_1 - b_2 - b_3) \neq 0$. Also, it has been assumed that the degradation of CNTs is an irreversible process, that is, the reformation of CNTs from the carbon cluster does not take place. Therefore, an additional condition of positivity, that is, $n_{1_i} > n_{1_{i-1}}$ is introduced while performing the time stepping. Along with the above constraints, the n_1 history in a cell is calculated as follows:

- If $n_{1_i}^{(1)} > n_{1_{i-1}}$ and $n_{1_i}^{(1)} < n_{1_i}^{(2)}$, then $n_{1_i} = n_{1_i}^{(1)}$;
- Else if $n_{1_i}^{(2)} > n_{1_{i-1}}$, then $n_{1_i} = n_{1_i}^{(2)}$;
- Otherwise the value of n_1 remains the same as in the previous time step, that is, $n_{1_i} = n_{1_{i-1}}$.

Simplification of Eq. (A.6) results in the following equation:

$$S_i{}^2 + (c_1 + c_2 - S_{i-1})S_i - c_1 = 0 \; , \tag{A.14}$$

where

$$c_1 = \Delta t n_{1_i} A_{n_i} \sqrt{\frac{kT}{2\pi m_1}} \; , \tag{A.15}$$

$$c_2 = \Delta t \frac{2\beta_{11}}{81} \frac{\Theta^{7/2}}{\sqrt{2\pi}} n_{1_i} \frac{\exp\left(\Theta - \frac{4\Theta^3}{27(\ln S_{i-1})^2}\right)}{(\ln S_{i-1})^3} \; . \tag{A.16}$$

Solution of Eq. (A.14) yields the following two roots:

$$S_i = -\frac{1}{2}(c_1 + c_2 - S_{i-1}) \pm \frac{1}{2}\sqrt{c_1 + c_2 - S_{i-1}^2 + 4c_1} \; . \tag{A.17}$$

For the first time step, c_1 and c_2 are calculated with the following conditions: n_{1_1} from the above calculation, $S(0) = S_0$, and $A_{n_0} = A_{n0}$. Realistically, the saturation ratio S cannot be negative or equal to one. Therefore, $S_i > 0$ yields $c_1 > 0$.

While solving for A_n, the Eq. (A.8) is solved with the values of n_1 and S from the above calculations and the initial conditions $A_{n_0} = A_{n0}$, $M_{1_0} = M_0$. The value of M_{1_0} was calculated by assuming $n(d_p, t)$ as a standard normal distribution function.

Appendix B

Calculation of the parameters c_{11} to c_{33}

$$
\begin{bmatrix}
0 & \frac{2\beta_3^2 D_e}{t_h b \sin(\alpha/2)(1+\cos(\alpha/2))} & 0 \\
0 & \frac{2\beta_3^2 D_e \sin\beta}{t_h b \sin^2(\alpha/2)(1+\cos(\alpha/2))} & 0 \\
\frac{2\beta_3^2 D_e}{t_h a \sin(\alpha/2)(1+\cos(\alpha/2))} & 0 & 0
\end{bmatrix}
=
\begin{bmatrix}
c_{11} & c_{12} & c_{13} \\
c_{21} & c_{22} & c_{23} \\
c_{31} & c_{32} & c_{33}
\end{bmatrix}
\begin{bmatrix}
0 & \frac{1}{b} & \frac{\cot(\alpha/2)}{2} \\
0 & \frac{\cos(\alpha/2)}{a+b\cos(\alpha/2)} & -\frac{b\sin(\alpha/2)}{2(a+b\cos(\alpha/2))} \\
\frac{\cot(\alpha/2)}{2b} & \frac{\cot(\alpha/2)}{2b} + \frac{\sin(\alpha/2)}{a(1+\cos(\alpha/2))} & -\frac{c\sin(\alpha/2)\cos(\pi/2n_1)}{2a(1+\cos(\alpha/2))\sin\beta}
\end{bmatrix},
\tag{B.1}
$$

RHS=

$$\begin{bmatrix} \frac{c_{13}\cot(\alpha/2)}{2b} & \begin{array}{l} \frac{c_{11}}{b}+\frac{c_{12}\cos(\alpha/2)}{(a+b\cos(\alpha/2))} \\ +\frac{c_{13}\cot(\alpha/2)}{2b}+\frac{c_{13}\sin(\alpha/2)}{a(1+\cos(\alpha/2))} \end{array} & \begin{array}{l} \frac{c_{11}\cot(\alpha/2)}{2}-\frac{c_{12}b\sin(\alpha/2)}{2(a+b\cos(\alpha/2))} \\ -\frac{c_{13}c\sin(\alpha/2)\cos(\pi/2n_1)}{2a\sin\beta(1+\cos(\alpha/2))} \end{array} \\ \\ \frac{c_{23}\cot(\alpha/2)}{2b} & \begin{array}{l} \frac{c_{21}}{b}+\frac{c_{22}\cos(\alpha/2)}{(a+b\cos(\alpha/2))} \\ +\frac{c_{23}\cot(\alpha/2)}{2b}+\frac{c_{23}\sin(\alpha/2)}{a(1+\cos(\alpha/2))} \end{array} & \begin{array}{l} \frac{c_{21}\cot(\alpha/2)}{2}-\frac{c_{22}b\sin(\alpha/2)}{2(a+b\cos(\alpha/2))} \\ -\frac{c_{23}c\sin(\alpha/2)\cos(\pi/2n_1)}{2a\sin\beta(1+\cos(\alpha/2))} \end{array} \\ \\ \frac{c_{33}\cot(\alpha/2)}{2b} & \begin{array}{l} \frac{c_{31}}{b}+\frac{c_{32}\cos(\alpha/2)}{(a+b\cos(\alpha/2))} \\ +\frac{c_{33}\cot(\alpha/2)}{2b}+\frac{c_{33}\sin(\alpha/2)}{a(1+\cos(\alpha/2))} \end{array} & \begin{array}{l} \frac{c_{31}\cot(\alpha/2)}{2}-\frac{c_{32}b\sin(\alpha/2)}{2(a+b\cos(\alpha/2))} \\ -\frac{c_{33}c\sin(\alpha/2)\cos(\pi/2n_1)}{2a\sin\beta(1+\cos(\alpha/2))} \end{array} \end{bmatrix} \tag{B.2}$$

Now, comparing term by term of LHS and RHS, we get

$$\frac{c_{13}\cot(\alpha/2)}{2b}=0$$

Therefore,

$$c_{13}=0 \tag{B.3}$$

$$\frac{c_{11}}{b}+\frac{c_{12}\cos(\alpha/2)}{(a+b\cos(\alpha/2))}+\frac{c_{13}\cot(\alpha/2)}{2b}+\frac{c_{13}\sin(\alpha/2)}{a(1+\cos(\alpha/2))}=\frac{2\beta_3^2D_e}{t_hb\sin(\alpha/2)(1+\cos(\alpha/2))}$$

As $c_{13}=0$, therefore,

$$\frac{c_{11}}{b}+\frac{c_{12}\cos(\alpha/2)}{(a+b\cos(\alpha/2))}=\frac{2\beta_3^2D_e}{t_hb\sin(\alpha/2)(1+\cos(\alpha/2))} \tag{B.4}$$

Next,

$$\frac{c_{11}\cot(\alpha/2)}{2}-\frac{c_{12}b\sin(\alpha/2)}{2(a+b\cos(\alpha/2))}-\frac{c_{13}c\sin(\alpha/2)\cos(\pi/2n_1)}{2a\sin\beta(1+\cos(\alpha/2))}=0$$

Therefore,

$$\frac{c_{11}\cot(\alpha/2)}{2}=\frac{c_{12}b\sin(\alpha/2)}{2(a+b\cos(\alpha/2))}$$

Rearranging both sides, we get

$$c_{11}=\frac{c_{12}b\sin^2(\alpha/2)}{\cos(\alpha/2)(a+b\cos(\alpha/2))} \tag{B.5}$$

Substituting this value in Eq.(76), we get

$$c_{12}\left[\frac{\sin^2(\alpha/2)}{\cos(\alpha/2)(a+b\cos(\alpha/2))}+\frac{\cos(\alpha/2)}{(a+b\cos(\alpha/2))}\right]=\frac{2\beta_3^2 D_e}{t_h b\sin(\alpha/2)(1+\cos(\alpha/2))}$$

By further solving this equation, one can write

$$c_{12}\left[\frac{\sin^2(\alpha/2)+\cos^2(\alpha/2)}{\cos(\alpha/2)(a+b\cos(\alpha/2))}\right]=\frac{2\beta_3^2 D_e}{t_h b\sin(\alpha/2)(1+\cos(\alpha/2))}$$

Rearranging both sides, one gets

$$c_{12}=\frac{2\beta_3^2 D_e\cos(\alpha/2)(a+b\cos(\alpha/2))}{t_h b\sin(\alpha/2)(1+\cos(\alpha/2))} \tag{B.6}$$

Now,

$$c_{11}=\frac{2\beta_3^2 D_e\cos(\alpha/2)(a+b\cos(\alpha/2))}{t_h b\sin(\alpha/2)(1+\cos(\alpha/2))}\frac{b\sin^2(\alpha/2)}{\cos(\alpha/2)(a+b\cos(\alpha/2))}$$

Therefore,

$$c_{11}=\frac{2\beta_3^2 D_e\sin(\alpha/2)}{t_h(1+\cos(\alpha/2))} \tag{B.7}$$

Now, equating element by element of the 2nd row, we get

$$\frac{c_{23}\cot(\alpha/2)}{2b}=0$$

Therefore,

$$c_{23}=0 \tag{B.8}$$

Next,

$$\frac{c_{21}}{b}+\frac{c_{22}\cos(\alpha/2)}{(a+b\cos(\alpha/2))}+\frac{c_{23}\cot(\alpha/2)}{2b}+\frac{c_{23}\sin(\alpha/2)}{a(1+\cos(\alpha/2))}=\frac{2\beta_3^2 D_e\sin\beta}{t_h b\sin^2(\alpha/2)(1+\cos(\alpha/2))}$$

As $c_{23}=0$, therefore,

$$\frac{c_{21}}{b}+\frac{c_{22}\cos(\alpha/2)}{(a+b\cos(\alpha/2))}=\frac{2\beta_3^2 D_e\sin\beta}{t_h b\sin^2(\alpha/2)(1+\cos(\alpha/2))} \tag{B.9}$$

Next,

$$\frac{c_{21}\cot(\alpha/2)}{2}-\frac{c_{22}b\sin(\alpha/2)}{2(a+b\cos(\alpha/2))}-\frac{c_{23}c\sin(\alpha/2)\cos(\pi/2n_1)}{2a\sin\beta(1+\cos(\alpha/2))}=0$$

By substituting the value of c_{23}, one can write

$$c_{21} = \frac{c_{22} b \sin^2(\alpha/2)}{\cos(\alpha/2)(a + b\cos(\alpha/2))} \tag{B.10}$$

Combining both the equations, we get

$$c_{22}\left[\frac{\sin^2(\alpha/2)}{\cos(\alpha/2)(a + b\cos(\alpha/2))} + \frac{\cos(\alpha/2)}{(a + b\cos(\alpha/2))}\right] = \frac{2\beta_3^2 D_e \sin\beta}{t_h b \sin^2(\alpha/2)(1 + \cos(\alpha/2))}$$

Further solving this equation, one can write

$$c_{22}\left[\frac{\sin^2(\alpha/2) + \cos^2(\alpha/2)}{\cos(\alpha/2)(a + b\cos(\alpha/2))}\right] = \frac{2\beta_3^2 D_e \sin\beta}{t_h b \sin^2(\alpha/2)(1 + \cos(\alpha/2))}$$

Therefore,

$$c_{22} = \frac{2\beta_3^2 D_e \sin\beta \cos(\alpha/2)(a + b\cos(\alpha/2))}{t_h b \sin^2(\alpha/2)(1 + \cos(\alpha/2))} \tag{B.11}$$

Substituting the value of c_{22}, we get

$$c_{21} = \frac{2\beta_3^2 D_e \sin\beta}{t_h(1 + \cos(\alpha/2))} \tag{B.12}$$

Now, comparing element by element of the third row, we get

$$\frac{c_{33}\cot(\alpha/2)}{2b} = \frac{2\beta_3^2 D_e}{t_h a \sin(\alpha/2)(1 + \cos(\alpha/2))}$$

Therefore,

$$c_{33} = \frac{4\beta_3^2 b D_e}{t_h a \cos(\alpha/2)(1 + \cos(\alpha/2))} \tag{B.13}$$

Next,

$$\frac{c_{31}}{b} + \frac{c_{32}\cos(\alpha/2)}{(a + b\cos(\alpha/2))} + \frac{c_{33}\cot(\alpha/2)}{2b} + \frac{c_{33}\sin(\alpha/2)}{a(1 + \cos(\alpha/2))} = 0$$

Substituting the value of c_{33}, we get

$$\frac{c_{31}}{b} + \frac{c_{32}\cos(\alpha/2)}{(a + b\cos(\alpha/2))} + \frac{2\beta_3^2 D_e}{t_h a \sin(\alpha/2)(1 + \cos(\alpha/2))} + \frac{4\beta_3^2 b D_e \sin(\alpha/2)}{t_h a^2 \cos(\alpha/2)(1 + \cos(\alpha/2))^2} = 0 \tag{B.14}$$

Now, after comparing the last term of both the sides, one can write

$$\frac{c_{31}\cot(\alpha/2)}{2}-\frac{c_{32}b\sin(\alpha/2)}{2(a+b\cos(\alpha/2))}-\frac{c_{33}c\sin(\alpha/2)\cos(\pi/2n_1)}{2a\sin\beta(1+\cos(\alpha/2))}=0$$

Substituting the value of c_{33}, we get

$$\frac{c_{31}\cot(\alpha/2)}{2}-\frac{c_{32}b\sin(\alpha/2)}{2(a+b\cos(\alpha/2))}-\frac{4\beta_3^2bD_e}{t_ha\cos(\alpha/2)(1+\cos(\alpha/2))}\frac{c\sin(\alpha/2)\cos(\pi/2n_1)}{2a\sin\beta(1+\cos(\alpha/2))}=0$$

Further solving, we get

$$c_{31}-c_{32}\frac{2}{\cot(\alpha/2)}\frac{b\sin(\alpha/2)}{2(a+b\cos(\alpha/2))}-\frac{2}{\cot(\alpha/2)}\frac{4\beta_3^2bD_e}{t_ha\cos(\alpha/2)(1+\cos(\alpha/2))}$$

$$\frac{c\sin(\alpha/2)\cos(\pi/2n_1)}{2a\sin\beta(1+\cos(\alpha/2))}=0$$

$$c_{31}=\frac{c_{32}b\sin(\alpha/2)}{\cot(\alpha/2)(a+b\cos(\alpha/2))}+\frac{4\beta_3^2bcD_e\sin(\alpha/2)\cos(\pi/2n_1)}{t_ha^2\cot(\alpha/2)\cos(\alpha/2)\sin\beta(1+\cos(\alpha/2))^2} \tag{B.15}$$

Substituting this value in Eq. (B.14), one can write

$$\frac{c_{32}\sin(\alpha/2)}{\cot(\alpha/2)(a+b\cos(\alpha/2))}+\frac{4\beta_3^2cD_e\sin(\alpha/2)\cos(\pi/2n_1)}{t_ha^2\cot(\alpha/2)\cos(\alpha/2)\sin\beta(1+\cos(\alpha/2))^2}+\frac{c_{32}\cos(\alpha/2)}{(a+b\cos(\alpha/2))}$$

$$+\frac{2\beta_3^2D_e}{t_ha\sin(\alpha/2)(1+\cos(\alpha/2))}+\frac{4\beta_3^2bD_e\sin(\alpha/2)}{t_ha^2\cos(\alpha/2)(1+\cos(\alpha/2))^2}=0$$

Solving it further,

$$c_{32}\left(\frac{\sin^2(\alpha/2)}{\cos(\alpha/2)(a+b\cos(\alpha/2))}+\frac{\cos(\alpha/2)}{(a+b\cos(\alpha/2))}\right)+\frac{4\beta_3^2cD_e\sin^2(\alpha/2)\cos(\pi/2n_1)}{t_ha^2\cos^2(\alpha/2)\sin\beta(1+\cos(\alpha/2))^2}$$

$$+\frac{2\beta_3^2D_e}{t_ha\sin(\alpha/2)(1+\cos(\alpha/2))}+\frac{4\beta_3^2bD_e\sin(\alpha/2)}{t_ha^2\cos(\alpha/2)(1+\cos(\alpha/2))^2}=0$$

Further simplification leads to

$$c_{32}\left(\frac{\sin^2(\alpha/2)+\cos^2(\alpha/2)}{\cos(\alpha/2)(a+b\cos(\alpha/2))}\right)=-\frac{2\beta_3^2D_e}{t_ha(1+\cos(\alpha/2))}\left(\frac{2c\sin^2(\alpha/2)\cos(\pi/2n_1)}{a\cos^2(\alpha/2)\sin\beta(1+\cos(\alpha/2))}\right.$$

$$+\frac{1}{\sin(\alpha/2)}+\frac{2b\sin(\alpha/2)}{a\cos(\alpha/2)(1+\cos(\alpha/2))}\Bigg)$$

Finally, c_{32} can be written as

$$c_{32}=-\frac{2\beta_3^2 D_e\cos(\alpha/2)(a+b\cos(\alpha/2))}{t_h a(1+\cos(\alpha/2))}\Bigg(\frac{2c\sin^2(\alpha/2)\cos(\pi/2n_1)}{a\cos^2(\alpha/2)\sin\beta(1+\cos(\alpha/2))}+\frac{1}{\sin(\alpha/2)}$$

$$+\frac{2b\sin(\alpha/2)}{a\cos(\alpha/2)(1+\cos(\alpha/2))}\Bigg) \tag{B.16}$$

By substituting this value of c_{32}, c_{31} can be expressed as

$$c_{31}=-\frac{2\beta_3^2 D_e\cos(\alpha/2)(a+b\cos(\alpha/2))}{t_h a(1+\cos(\alpha/2))}\frac{b\sin(\alpha/2)}{\cot(\alpha/2)(a+b\cos(\alpha/2))}$$

$$\Bigg(\frac{2c\sin^2(\alpha/2)\cos(\pi/2n_1)}{a\cos^2(\alpha/2)\sin\beta(1+\cos(\alpha/2))}+\frac{1}{\sin(\alpha/2)}+\frac{2b\sin(\alpha/2)}{a\cos(\alpha/2)(1+\cos(\alpha/2))}\Bigg)$$

$$+\frac{4\beta_3^2 bcD_e\sin(\alpha/2)\cos(\pi/2n_1)}{t_h a^2\cot(\alpha/2)\cos(\alpha/2)\sin\beta(1+\cos(\alpha/2))^2} \tag{B.17}$$

Appendix C

Derivation of out-of-plane stress ($\sigma_{\mathbf{rr}}$)

Consider $a = b$. Then,

$$\sin 30^o = \frac{d}{a} \ , \quad \cos 30^o = \frac{g}{a} \ ,$$

This gives

$$d = \frac{a}{2} \ , \quad 2g = \sqrt{3}a \ ,$$

Therefore, area of projection of the resulting pyramidal shape due to the out-of-plane deformation of the center atom is expressed as

$$A_r = \frac{1}{2}(3d)(2g) = \frac{3\sqrt{3}}{4}a^2 \ ,$$

The energy due to transverse stretching is expressed as

$$\mathcal{U} = \frac{1}{2}k_3(\Delta\psi)^2$$

where k_3 is effective elastic constant and

$$\Delta\psi = \frac{du_r^{(2)}}{ds}\cos(\bar{\alpha}/2) + \frac{du_r^{(2)}}{dz}\sin(\bar{\alpha}/2) \ ,$$

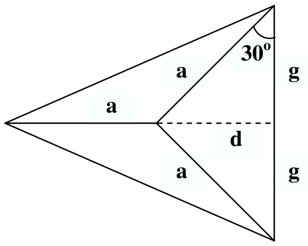

Figure C.1: Analytical model of a CNT.

In this case, $\bar{\alpha}$ is the angle, which the bond makes with respect to $\theta\theta$ direaction in the θz plane. Taking average of $\Delta\psi$ from all the neighboring bonds,

$$\Delta\psi = \frac{du_r^{(2)}}{ds}\Big(1 + 2\cos(\bar{\alpha}/2)\Big) + \frac{du_r^{(2)}}{dz}\Big(\sin(\bar{\alpha}/2) - \sin(\bar{\alpha}/2)\Big)$$

$$= \frac{du_r^{(2)}}{ds}\Big(1 + 2\cos(\bar{\alpha}/2)\Big) ,$$

Therefore,

$$\mathcal{U} = \frac{1}{2}k_3\Big[\frac{du_r^{(2)}}{ds}\Big(1 + 2\cos(\bar{\alpha}/2)\Big)\Big]^2 ,$$

The out-of-plane stress σ_{rr} can be expressed as

$$A_r\sigma_{rr} = -\frac{\partial\mathcal{U}}{\partial u_r^{(2)}}$$

Therefore,

$$\sigma_{rr} = -\frac{2k_3}{3\sqrt{3}a^2}\frac{\partial^2 u_r^{(2)}}{\partial s^2}(1 + 2\cos(\bar{\alpha}/2))^2 , \qquad \text{(C.1)}$$

Appendix D

Converting the electromagnetics equation into Bessel form

The original equation is

$$\frac{\partial^2 E_{z'}(r)}{\partial r^2}+\frac{1}{r}\frac{\partial E_{z'}(r)}{\partial r}+\frac{1}{r^2}\frac{\partial^2 E_{z'}(r)}{\partial \theta_0^2}+\frac{\partial^2 E_{z'}(r)}{\partial z'^2}-\mu\sigma\frac{\partial E_{z'}(r)}{\partial t}-\mu\epsilon\frac{\partial^2 E_{z'}(r)}{\partial t^2}=0 \quad \text{(D.1)}$$

By substituing the Fourier transforms, one can write

$$\frac{\partial^2 \tilde{E}_{z'_k}(r)}{\partial r^2}+\frac{1}{r}\frac{\partial \tilde{E}_{z'_k}(r)}{\partial r}-\frac{1}{r^2}m_k^2\tilde{E}_{z'_k}(r)-q_k^2\tilde{E}_{z'_k}(r)+\mu\sigma j\omega_k\tilde{E}_{z'_k}(r)+\mu\epsilon\omega_k^2\tilde{E}_{z'_k}(r)=0 \quad \text{(D.2)}$$

Multiplying both sides of Eq. (D.2) by r^2, we get

$$r^2\frac{\partial^2 \tilde{E}_{z'_k}(r)}{\partial r^2}+r\frac{\partial \tilde{E}_{z'_k}(r)}{\partial r}+\left[r^2(\mu\sigma j\omega_k+\mu\epsilon\omega_k^2-q_k^2)-m_k^2\right]\tilde{E}_{z'_k}(r)=0 \quad \text{(D.3)}$$

By assuming $(\mu\sigma j\omega_k+\mu\epsilon\omega_k^2-q_k^2)=a^2$, Eq. (D.3) can be rewritten as

$$r^2\frac{\partial^2 \tilde{E}_{z'_k}(r)}{\partial r^2}+r\frac{\partial E_{z'_k}(r)}{\partial r}+(a^2r^2-m_k^2)\tilde{E}_{z'_k}(r)=0 \quad \text{(D.4)}$$

Substituting $y = ar$ in Eq. (D.4), we get

$$\frac{\partial^2 \tilde{E}_{z'_k}(r)}{\partial r^2} = a^2 \frac{\partial^2 \tilde{E}_{z'_k}}{\partial y^2} \ , \quad \frac{\partial \tilde{E}_{z'_k}(r)}{\partial r} = a \frac{\partial \tilde{E}_{z'_k}}{\partial y} \ . \tag{D.5}$$

With the help of Eq. (D.5), Eq. (D.4) can now be converted into the Bessel form

$$y^2 \frac{\partial^2 \tilde{E}_{z'_k}}{\partial y^2} + y \frac{\partial \tilde{E}_{z'_k}}{\partial y} + (y^2 - m_k^2) \tilde{E}_{z'_k} = 0 \ . \tag{D.6}$$

The Bessel function yields a solution, which is given by

$$\tilde{E}_{z'_k} = \tilde{\tilde{E}}_{z'_k} J_{m_k}(r) \tag{D.7}$$

where J_{m_k} is expressed as

$$J_{m_k} = \sum_{p=0}^{\infty} \frac{(-1)^p (y/2)^{(m_k+2p)}}{p! \Gamma(m_k + p + 1)} \tag{D.8}$$

The Bessel solution of second kind is neglected for simplicity in this case.

Appendix E

Details of the design of vacuum chamber

As discussed in chapter 1, field emission experiments require ultra-high vacuum (UHV) conditions. Successful field emission can only occur in a vacuum where the emitted electrons can actually reach the anode and avoid colliding with air particles. Therefore, a vacuum chamber had to be designed to house the CNTs and the anodes in a vacuum environment. There were several constraints placed on the chamber design:

1. Vacuum chamber (must reach pressures less than 10-6 Torr);
2. Use UHV compatible materials only (stainless steel, Teflon, OFHC copper);
3. Interchangeable mount for a 10mm x 10mm CNT film;
4. Mechanism to manipulate the CNT-electrode gap (0-500 μm);
5. Allow for a minimum of 5 electrical leads to be fed through into the vacuum;

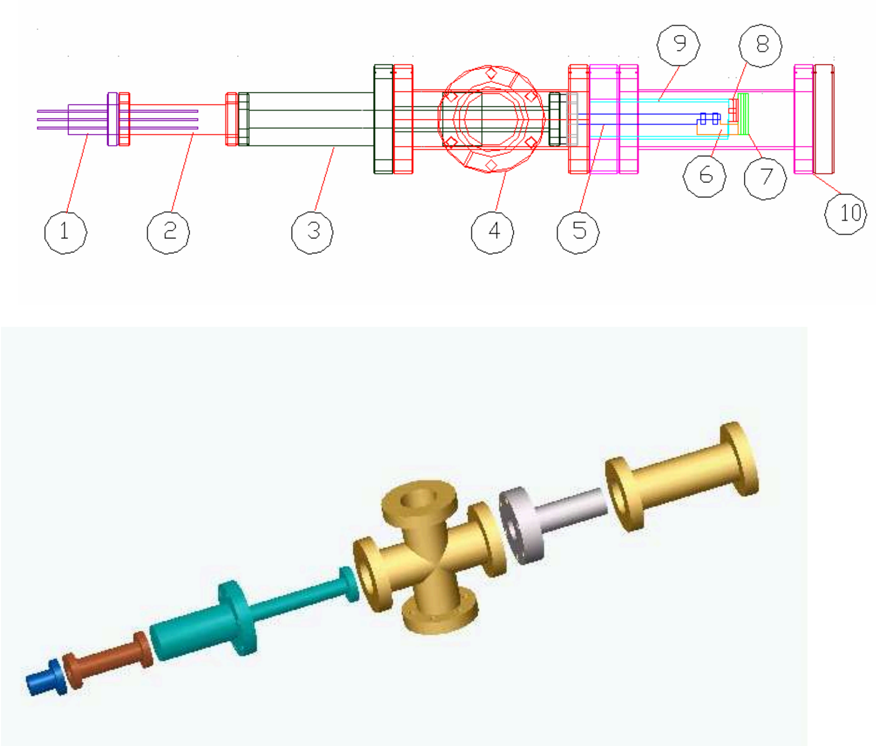

Figure E.1: Schematic design of the vacuum chamber.

6. Allow for electrodes and anode target to be insulated from the chamber; and
7. Two ports available for connections to pumps.

Figure E.1 shows the drawing of the vacuum chamber, which was designed fulfilling the requirements. The following are details regarding each component:

1. Instrumentation feedthrough: An 8 pin feedthrough is used to connect wiring from the atmosphere side to the vacuum side. The CNT will be connected to one wire while the electrodes will be connected to a wire each.
2. 1.33” nipple: This fitting is used to attach the instrumentation feedthrough to the micrometer. The leads of the instrumentation feedthrough are 2” long

and cannot be cut shorter due to the risk of damaging the ceramic seal. Since this will not fit inside the body of the micrometer, a standoff was required and the 1.33" nipple fit the role.

3. Micrometer linear feedthrough: With a resolution of 0.002" (50.8 microns) and a range of 1" (25.4mm) this micrometer has a hollow tube through which flexible wires can be passed through.
4. Four way cross: This is similar to a standard stainless steel 2.75"(69.85mm) four way cross, the only exception being that all the flanges are of the Conflat design.
5. Micrometer extension: A 0.25" (6.35mm) ground rod was used to extend the reach of the micrometer. A gate holder was attached to the end of the rod.
6. Gate holder: This machined component was made as an attachment between the ground rod and the gate.
7. Gate: This component was machined to be the frame onto which the electrodes can be mounted.
8. CNT mount: This is the stainless steel component onto which the CNTs are deposited. This piece is mounted onto the CNT holder via two screws.
9. CNT holder: A 1" (25.4mm) diameter stainless steel tube was welded onto a 2.75" (69.85mm) double sided Conflat flange.
10. 2.75" nipple: This fitting is used to seal the end of the chamber thereby enclosing all the inner components. For the second phase of design, this fitting will be replaced by other components.

Appendix F

List of publications during PhD

1. N. Sinha and J.T.W. Yeow, "Carbon nanotubes for biomedical applications," *IEEE Transactions on Nanobioscience*, vol. 4, no. 2, pp. 180-195, 2005.

2. N. Sinha and J.T.W. Yeow, "Modeling of the behavior of random carbon nanotubes during field emission," *Proc. 2005 International Conference on MEMS, Nano, and Smart Systems*, pp. 371-376, Banff, Canada, 2005.

3. N. Sinha, D. Roy Mahapatra, J.T.W. Yeow, R.V.N. Melnik and D.A. Jaffray, "Characterization of self-assembly and evolution in carbon nanotube thin film field emitter," *Proc. 6th IEEE International Conference on Nanotechnology*, Cincinnati, USA, pp. 673-676, 2006.

4. N. Sinha, D. Roy Mahapatra, J.T.W. Yeow, R.V.N. Melnik and D.A. Jaffray, "A quantum-hydrodynamic coupled model of field emission from carbon nanotube thin films," *Proc. 7th World Congress on Computational Mechanics*, Los Angeles, USA, pp. 0459, 2006.

5. N. Sinha, D. Roy Mahapatra, J.T.W. Yeow, R.V.N. Melnik and D.A. Jaffray,

"Carbon nanotube thin film field emitters: effect of disorderness of the film on field emission properties," *International Workshop on Physics of Disordered and Mesoscopic materials*, IIT, Kanpur, India, 2006.

6. N. Sinha, D. Roy Mahapatra, J.T.W. Yeow, R.V.N. Melnik and D.A. Jaffray, "Carbon nanotube based sensors," *Journal of Nanoscience and Nanotechnology*, vol. 6, no. 3, pp. 573-590, 2006.

7. N. Sinha, D. Roy Mahapatra, J.T.W. Yeow, R.V.N. Melnik and D.A. Jaffray, "Carbon nanotube thin film field emitting diode: understanding system response based on multiphysics modeling and analysis," *Journal of Computational and Theoretical Nanoscience*, vol. 4, no. 3, pp. 535-549, 2007.

8. N. Sinha, D. Roy Mahapatra, J.T.W. Yeow and R.V.N. Melnik, "Modeling the field emission current fluctuation in carbon nanotube thin films," *Proc. 10th Annual NSTI Nanotechnology Conference*, Santa Clara, USA, vol. 1, pp. 76-79, 2007.

9. N. Sinha, D. Roy Mahapatra, J.T.W. Yeow and R.V.N. Melnik, "Multi-mode phonon-controlled field emission from carbon nanotubes: modeling and experiments," *Proc. 7th IEEE International Conference on Nanotechnology*, Hong Kong, pp. 961-964, 2007.

10. N. Sinha, J.T.W. Yeow and D.A. Jaffray, "Experimental investigation of the crosstalk phenomenon and current stability in a carbon nanotube array," *Proc. 7th IEEE International Conference on Nanotechnology*, Hong Kong, pp. 194-197, 2007.

11. R.V.N. Melnik, D. Roy Mahapatra, N. Sinha, J.T.W. Yeow, D.A. Jaffray, M. Willatzen, B. Lassen and L. Lew Yan Voon, "Coupled nonlinear effects in

nanostructures and their applications," *Proc. 6th International Congress on Industrial and Applied Mathematics*, Zurich, Switzerland, pp. 303-304, 2007.

12. N. Sinha and J.T.W. Yeow, "Carbon nanotube based field emission devices for x-ray generation," *Proc. International Conference on Nanomedicine and its Applications*, Tanjavur, India, pp. 136-146, 2007.

13. N. Sinha, D. Roy Mahapatra, Y. Sun, J.T.W. Yeow, R.V.N. Melnik and D.A. Jaffray, "Electromechanical interactions in a carbon nanotube based thin film field emitting diode," *Nanotechnology*, vol. 19, no. 2, pp. 25710 (1-12), 2008.

14. R.V.N. Melnik, D. Roy Mahapatra, N. Sinha and J.T.W. Yeow, "Coupled nonlinear effects on field emission from CNTs," *Proc. in Applied Mathematics and Mechanics*, vol. 7, no. 1, pp. 1030801-1030802, 2008.

15. N. Sinha and J.T.W. Yeow, "Nanotechnology for oncology," *Encyclopedia of Nanoscience and Nanotechnology*, Ed. H.S. Nalwa, American Scientific Publishers, (in press).

16. J.T.W. Yeow and N. Sinha, "Carbon nanotube and fullerene sensors," *Sensors Based on Nanostructured Materials*, Ed. Francisco Arregui, Springer, (in press).

17. N. Sinha, D. Roy Mahapatra, R.V.N. Melnik and J.T.W. Yeow, "Computational implementation of a new multiphysics model for field emission from CNT thin films," *International Conference on Computational Science*, Krakow, Poland, (To appear in Lecture Notes in Computer Science).

18. D. Roy Mahapatra, N. Sinha, R.V.N. Melnik and J.T.W. Yeow, "Characterizing hysteresis in field emission from carbon nanotube arrays," *Proc. 6th*

EUROMECH Nonlinear Dynamics Conference, Saint Petersburg, Russia (Accepted).

19. D. Roy Mahapatra, N. Sinha, R.V.N. Melnik and J.T.W. Yeow, “Field emission properties of carbon nanotube arrays with defects and impurities,” *Proc. 11th Annual NSTI Nanotechnology Conference*, Boston, USA, (Accepted).
20. D. Roy Mahapatra, N. Sinha, R.V.N. Melnik and J.T.W. Yeow, “Design optimization of field emission from a stacked carbon nanotube array,” *Proc. 11th Annual NSTI Nanotechnology Conference*, Boston, USA, (Accepted).
21. N. Sinha, Y. sun and J.T.W. Yeow, “Field emission properties of carbon nanotube thin films grown on different substrate materials,” *8th IEEE International Conference on Nanotechnology*, Arlington, USA, (Accepted).